

Fermilab

FERMILAB-THESIS-2000-29

UMAHEP 459
September 2000

DIFFRACTIVELY PRODUCED CHARM
FINAL STATES IN 800 GeV/c
PROTON-PROTON COLLISIONS

Michael H.L.S. Wang

Submitted to the Graduate School of the
University of Massachusetts Amherst in partial fulfillment
of the requirements for the degree of

DOCTOR OF PHILOSOPHY

September 2000

Department of Physics and Astronomy

Supported in part by U.S. National Science Foundation Grant
PHY90-14879.

Performed in part under the auspices of the U.S. Department of Energy
by the Lawrence Livermore National Laboratory under contract
W-7405-ENG-48.

©Copyright by Michael H.L.S. Wang 2000

All Rights Reserved

DIFFRACTIVELY PRODUCED CHARM FINAL STATES IN 800 GeV/c
PROTON-PROTON COLLISIONS

A Dissertation Presented

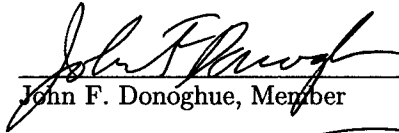
by

MICHAEL H.L.S. WANG

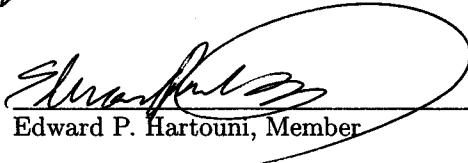
Approved as to style and content by:



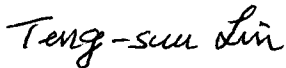
Michael N. Kreisler, Chairperson



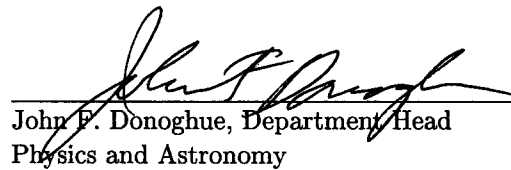
John F. Donoghue, Member



Edward P. Hartouni, Member



Teng-Sun Liu, Member



John F. Donoghue, Department Head
Physics and Astronomy

ACKNOWLEDGEMENTS

I wish to thank my two mentors, Ed Hartouni and Mike Kreisler, for providing me with the opportunity and the resources to work with the E690 collaboration.

Ed has guided me closely throughout my research in the fascinating field of particle physics. The systematic approach he takes to tackle seemingly insurmountable problems has influenced me immensely. Digging out the tiny D^* signals buried beneath tons of background in the E690 data would have been close to impossible if I had not pursued his advice of developing a simple diffractive charm event generator for exploring possible decay modes and analysis cuts to use. Looking back at all these years of working with Ed, I find most valuable his outstanding ability, not simply to have all the answers to a graduate student's queries, but to set you up on a well thought-out path to discover and figure things out on your own. This, I believe, is the hallmark of an ideal research advisor. I also thank him for providing me with the computing hardware necessary to realize much of the work described in this dissertation.

To Mike, I am most grateful for consistently securing the necessary research funding to support me during my years at both UMass and LLNL. But more importantly, Mike has influenced me in a much deeper way through his exceptional ability to think and reason like a true physicist—in the simplest possible terms uncluttered by the jargon and often convoluted reasoning fashionable these days that reveal nothing of the underlying physics. Working with Mike on the Σ^0 mass paper has also instilled in me a great appreciation for the importance of making careful experimental measurements, and in writing concisely but coherently in scientific publications, providing enough details for the analysis to be understood clearly.

None of the work presented in this dissertation would have been possible if it were not for the heroic efforts of a small band of extremely talented and independent minded physicists belonging

to the E690 collaboration (Appendix A). To Dave Christian must be given much of the credit for keeping this collaboration active and alive through all these years and for almost single-handedly completing the Pass 2 offline reconstruction. I am most grateful to him for taking a sincere interest and active role in the diffractive charm analysis and for his valuable contributions to this analysis. I thank Erik Gottschalk for his encouragement and for his generosity in offering his superb talents and skills to assist in any aspect of E690 analysis. To Gastón Gutiérrez goes the credit for realizing, early on, the physics potential of E690 in terms of providing an ideal laboratory for exotic light-meson spectroscopy. I thank Alan Wehmann for his consistent and active participation in the E690 collaboration. No acknowledgement of the contributions from fellow E690 collaborators would be complete without mentioning the outstanding vision of the group’s spokesperson, Bruce Knapp. Though I have never had the opportunity of working directly with Bruce, countless hours spent struggling with code written by him has inspired in me a deep sense of respect for his extraordinary physical intuition.

I thank my fellow UMass graduate students Jorge Uribe, Shuyu Lee, and Kyriacos Markianos for blazing the trail before me, making my ride through E690 analysis a much smoother and more pleasant one. Jorge and Shuyu were senior graduate students who helped me get acquainted with BNL E766 and FNAL E690 analysis when I first joined the group. Kyriacos was also a senior graduate student who accompanied me on that long cross-country trip from the East Coast to Livermore, CA in a huge Penske truck carrying four processor racks and *umahp4*—an 8-CPU SGI—among other things. I have learned much from his expansive knowledge, particularly of things related to the hardware processor. I also wish to thank our collaborators from Mexico—Julián Félix, Marco Reyes, and Modesto Sosa—for their continued interest in E690 analysis and in continuing to produce top-caliber physics results from the E690 data.

I wish to acknowledge the administrative and technical support I received from Al McConkey, Dianne Quilty, and Jane Knapp of UMass and Pat Smith, Rudy Bauer, and Jo Ann Harris of LLNL’s N-division. I thank James Walker for his assistance as graduate program director at UMass.

Among my professors at UMass graduate school, Art Swift deserves special mention as an exceptional instructor whose mastery of the subject matter and difficult but extremely useful problem sets have left an indelible mark on countless UMass graduates including myself.

I thank John Donoghue, chairman of the Department of Physics and Astronomy, and Teng-Sun Liu of the Department of Mathematics and Statistics for the rare privilege of having them serve on my dissertation committee. I thank John Donoghue for his insightful advice as a graduate program advisor. I am deeply grateful to Teng-Sun Liu and his wife Yi-Keng for their hospitality during my years at Amherst. I also thank my Aunt Josephine and Uncle George for providing a refuge from graduate school while I was on the East Coast.

I acknowledge the assistance of Andrei Solodsky and Shinhong Kim of the CDF collaboration in clarifying some issues on CDF's diffractive b -quark analysis.

Lastly, I am eternally indebted to my entire family, to my mother Elizabeth and my brother Edward, in particular, for their continued support and encouragement throughout this long and arduous but rewarding journey.

ABSTRACT

DIFFRACTIVELY PRODUCED CHARM FINAL STATES IN 800 GeV/c
PROTON-PROTON COLLISIONS

SEPTEMBER 2000

MICHAEL H.L.S. WANG, B.S., UNIVERSITY OF THE PHILIPPINES DILIMAN

M.S., UNIVERSITY OF MASSACHUSETTS AMHERST

Ph.D., UNIVERSITY OF MASSACHUSETTS AMHERST

Directed by: Professors Michael N. Kreisler and Edward P. Hartouni

We report the observation of charm final states produced in the single diffractive dissociative reactions (1) $pp \rightarrow pX(D^{*+} \rightarrow (D^0 \rightarrow K^- \pi^+) \pi^+)$ and (2) $pp \rightarrow pX(D^{*-} \rightarrow (\bar{D}^0 \rightarrow K^+ \pi^-) \pi^-)$. These results are based on the over 5 billion event data sample acquired by Fermilab experiment E690 during the fixed target run of 1991. In this run, an 800 GeV/c incident proton beam was used with a liquid hydrogen target. We measure cross sections of $[0.209 \pm 0.050(\text{stat})_{-0.040}^{+0.083}(\text{syst})] \mu\text{b}$ and $[0.196 \pm 0.043(\text{stat})_{-0.046}^{+0.014}(\text{syst})] \mu\text{b}$ for reactions (1) and (2), respectively. These results are compared with model predictions and results from other experiments. Our results are significantly lower than predictions based on the diffractive model of Ingelman and Schlein using a flat or a hard pomeron structure function.

Contents

ACKNOWLEDGEMENTS	iv
ABSTRACT	vii
LIST OF FIGURES	xiii
LIST OF TABLES	xvii
CHAPTER	
1 INTRODUCTION	1
1.1 Hadronic Diffraction	2
1.2 Regge Phenomenology and the Pomeron	4
1.3 The Pomeron in QCD	11
1.3.1 Ingelman and Schlein Model	11
1.3.2 Experimental Investigation of the Pomeron Structure	14
1.3.3 Breakdown of Factorization in the Ingelman-Schlein Model	16
1.3.4 Renormalization of the Pomeron Flux	17
1.4 Gap Survival Probability	20
1.5 Diffractive Charm Production	21

CONTENTS

2	EXPERIMENTAL APPARATUS	25
2.1	Beam Spectrometer	26
2.1.1	Beamline	26
2.1.2	Incoming Beam Spectrometer	26
2.1.3	Forward Spectrometer	27
2.2	Multi-particle Spectrometer	27
2.2.1	Target Counter (TC) and Halo Counter (TVT)	29
2.2.2	Target System	29
2.2.3	Veto Counters	29
2.2.4	Middle and Rear Hodoscopes	31
2.2.5	Čerenkov Counter	33
2.2.6	Drift Chambers	33
2.2.7	Forward Hodoscope	35
2.3	Data Acquisition System	35
2.3.1	Overview	35
2.3.2	Fast Trigger Logic	39
2.3.3	Multiplicity Logic	43
2.3.4	Prescale Events	44
3	EVENT RECONSTRUCTION AND SELECTION	47
3.1	First Stage Track Reconstruction (Pass 1)	47
3.2	Track and Vertex Reconstruction (Pass 2)	50
3.2.1	Beam Track Reconstruction	50
3.2.2	Reconstruction of Multi-Particle Spectrometer Tracks	51
3.2.3	Primary Vertex Reconstruction	52
3.2.4	Secondary Vertex Reconstruction	53

CONTENTS

3.2.5	Pass 2 Output	57
3.3	Strip Job	58
3.4	D^* Candidates Selection	58
4	CROSS SECTION MEASUREMENT	63
4.1	Determination of N_{beam}	64
4.2	Determination of $N_{diff}(c\bar{c})$	70
4.2.1	Determining $N_{diff}^{obs}(D^*)$	71
4.2.2	D^* Acceptance Calculation	78
4.2.3	Results for $N_{diff}(c\bar{c})$	83
4.3	Total cross section	86
5	CONCLUSION	89
5.1	Comparison with Theoretical Predictions	90
5.2	Comparison with Other Experiments	92
5.2.1	Comparison with CDF and ZEUS	92
5.2.2	Comparison with Other Charm Experiments	97
5.3	Conclusions	100
APPENDICES		
A	THE E690 COLLABORATION	101
B	POMPYT PARAMETER SETTINGS	103
C	PYTHIA PARAMETER SETTINGS	111
	BIBLIOGRAPHY	117

CONTENTS

List of Figures

1.1	Contours for the scattering amplitude $A(s, t)$ in the complex l plane.	5
1.2	Chew-Frautschi plot for octet baryons.	7
1.3	Reggeon exchange diagram.	9
1.4	Triple Regge diagram.	10
1.5	CDF plot of discrepancy factor as a function of pomeron gluon content.	18
1.6	Total single diffractive $p\bar{p}$ cross sections calculated with standard and renormalized flux factors.	19
2.1	Block diagram of the E690 detector.	25
2.2	Detector elements of the E690 multi-particle spectrometer.	28
2.3	E690 target system.	30
2.4	Middle and rear hodoscope arrays.	32
2.5	Side view of the Čerenkov counter.	34
2.6	Forward hodoscope array.	36
2.7	Block diagram of the E690 data acquisition system.	38
2.8	Block diagram of the E690 Fast Trigger Logic.	40
3.1	3-plane line finder in Pass 1 beam chamber track reconstruction.	49
3.2	Multi-particle spectrometer track types reconstructed by Pass 1.	50

LIST OF FIGURES

3.3	Event reconstructed by Pass 2 with two secondary vertices from a possible decay of the type $\Xi^+ \rightarrow (\bar{\Lambda}^0 \rightarrow \bar{p}\pi^+)\pi^+$	56
3.4	Invariant mass plots of the D^{*+} and D^0	61
3.5	Invariant mass plots for the D^{*-} and \bar{D}^0	61
4.1	p_z sum of all reconstructed tracks assigned to the primary vertex versus Δp_z of the beam proton.	65
4.2	Cut used to select events with single incident beam protons.	67
4.3	Invariant mass of the reconstructed Ξ^- events in each geometry group used in the cross section measurement.	69
4.4	Invariant $K\pi\pi$ mass of D^* candidates used in cross section measurement.	72
4.5	Invariant $K\pi$ mass of D^0 's decaying from D^* candidates used in cross section measurement.	72
4.6	Invariant $K\pi\pi$ mass of D^* candidates used in cross section measurement satisfying coherence condition of $x_F > 0.90$	73
4.7	Invariant $K\pi$ mass of D^0 's decaying from D^* candidates used in cross section measurement satisfying coherence condition of $x_F > 0.90$	73
4.8	Q distributions of D^* candidate events.	74
4.9	x_F distributions of the D^* , X system, and scattered beam proton, p_{fast}	76
4.10	Rapidity, y , distributions of the D^* , X system, and scattered beam proton, p_{fast}	77
4.11	p_T^2 distributions of the scattered beam proton for the selected D^{*+} and D^{*-} candidate events.	78
4.12	Invariant $K^-\pi^+\pi^+$ mass versus x_F of the scattered beam proton for the D^{*+} candidate events.	79
4.13	Invariant $K^+\pi^-\pi^-$ mass versus x_F of the scattered beam proton for the D^{*-} candidate events.	80

LIST OF FIGURES

4.14	Comparison of the <i>flat</i> , <i>soft</i> , and <i>hard</i> pomeron parton distribution functions.	82
5.1	Total pp single diffractive D^* cross sections at $\sqrt{s} = 40$ GeV predicted by POMPYT plotted as a function of the gluon fraction in the pomeron.	91
5.2	x_F distribution of leading protons from charm events generated by PYTHIA.	94
5.3	Discrepancy factor, D , as a function of the pomeron's gluon content (Definition 1).	95
5.4	Discrepancy factor, D , as a function of the pomeron's gluon content (Definition 2).	98

LIST OF FIGURES

List of Tables

2.1	Multiplicity Logic trigger conditions used for most of the run.	44
2.2	Multiplicity Logic trigger conditions used at the beginning of the run.	45
2.3	Summary of E690 run conditions.	45
3.1	Mass limits used for identifying secondary vertex types in Pass 2.	54
3.2	Event types selected in Pass 2's select output.	57
3.3	Output streams produced by the Strip Job.	58
3.4	Selection criteria for charm meson strip.	59
3.5	Selection criteria for D^* candidates.	59
3.6	D^* Candidates selection summaries	60
4.1	Cuts used to select Ξ^- events for normalizing the number incident beam protons. . .	66
4.2	Number of reconstructed Ξ^- 's in each geometry group used in the cross section measurement.	70
4.3	D^* acceptance calculated using events generated with POMPYT.	84
4.4	Fraction of diffractive charm events containing a D^* as determined from POMPYT. . .	85
4.5	Total single diffractive charm cross sections with a coherence condition of $x_F > 0.85$. . .	87
4.6	Total single diffractive charm cross sections with a coherence condition of $x_F > 0.90$. . .	88

LIST OF TABLES

Chapter 1

Introduction

The study of diffraction in high energy hadron physics traces its history back to the days when it was understood in terms of optical concepts. In the 1960's, the application of Regge theory to the description of hadronic cross sections provided a new picture of diffraction in terms of the exchange of a virtual particle called the *pomeron*. This picture was largely forgotten until two decades ago when Ingelman and Schlein [1] proposed a simple model for investigating the structure of the pomeron within the context of QCD. Over the past two decades, experiments at CERN, DESY and Fermilab have provided ample evidence for the partonic structure of the pomeron in support of this model. However, these same experiments have also uncovered serious shortcomings in the model. The pomeron does not seem to possess the simple and universal nature expected. Clearly, a more sophisticated picture of diffraction is required. New measurements which extend existing ones are also needed to provide additional physical insight.

This thesis presents the first cross section measurement for diffractively produced charm in hadron-hadron interactions. It is based on roughly half of the 5.5 billion pp events acquired by experiment E690 during the Fermilab fixed target run of 1991. By comparing this measurement with theoretical predictions and diffractive data from other experiments, it hopes to contribute to our understanding of the nature of diffraction. In the following sections, this measurement is put in

CHAPTER 1. INTRODUCTION

the broader perspective of the study of high energy hadronic diffraction. Beginning with a generic description of hadronic diffraction, the concept of the pomeron is traced back to its origin in Regge theory. This is followed by a discussion of the model proposed by Ingelman and Schlein and the results from experiments undertaken to study the pomeron within the context of this model. The outstanding problems in our understanding of diffraction implied by these experimental results are briefly discussed. Finally, the chapter concludes with a section on diffractive charm production and the relevance of the E690 measurement.

1.1 Hadronic Diffraction

In the high energy domain, the scattering of hadrons on hadrons exhibits a number of striking features. The total cross section tends toward constant values as the energy increases. The differential elastic scattering cross section, $d\sigma_{\text{el}}/dt$, as a function of t , the invariant momentum transfer squared, is sharply peaked in the forward region of low t . This peak is well described by an exponential of the form $e^{-b|t|}$ where b is called the slope parameter. The slope parameter increases slowly as a function of energy causing a narrowing or shrinkage of the forward peak.

The forward peak observed in elastic scattering is a consequence of the quantum mechanical nature of hadrons. It is analogous to the case in classical optics where a beam of light incident on a circular absorbing disc forms a diffraction pattern behind the disc [3, 4]. Such optical diffraction patterns are characterized by a large central peak followed by a sequence of diminishing fringes. As in this optical analogy, the forward peaks observed in elastic hadron collisions are said to arise from the diffractive scattering of hadrons.

Diffraction can also occur in the inelastic scattering of hadrons such as in the single dissociative reaction $a + b \rightarrow a + X$. In this reaction, hadron b dissociates or breaks up into the system X while hadron a remains intact. From quantum mechanics, diffraction will occur when the effect of the collision on hadron a is small enough for it to retain coherence over the duration of the collision.

1.1. HADRONIC DIFFRACTION

This is satisfied when the wavelength associated with the minimum invariant momentum transfer ($\sqrt{|t_{min}|}$) of the collision is large compared to the dimensions of the scattering target [2]. For a reaction $1 + 2 \rightarrow 3 + 4$, t_{min} is given by:

$$\begin{aligned} t_{min} &= m_1^2 + m_3^2 - 2E_1^* E_3^* + 2|p_1^*| |p_3^*| \\ &= m_1^2 + m_3^2 - \frac{(s + m_1^2 - m_2^2)(s - m_3^2 - m_4^2)}{2s} \\ &\quad + 2 \left(\frac{\sqrt{s - (m_1 + m_2)^2} \sqrt{s - (m_1 - m_2)^2}}{2\sqrt{s}} \right) \left(\frac{\sqrt{s - (m_3 + m_4)^2} \sqrt{s - (m_3 - m_4)^2}}{2\sqrt{s}} \right) \end{aligned}$$

where s is the total energy squared in the center of mass frame of particles 1 and 2. E^* and p^* are the energies and momenta of the individual particles in this frame. In the case of $p + p \rightarrow p + X$, this becomes:

$$t_{min} = \frac{3m_p^2 - s + M_X^2}{2} + \frac{s}{2} \sqrt{1 - \frac{4m_p^2}{s}} \sqrt{1 - \frac{(m_p + M_X)^2}{s}} \sqrt{1 - \frac{(m_p - M_X)^2}{s}}.$$

In the limit where $s \gg M_X^2$ and m_p^2 , this reduces to¹:

$$t_{min} \cong -\frac{m_p^2 (M_X^2 - m_p^2)^2}{s^2}.$$

Assuming the size of the scattering target is given by $R = 1/m_\pi$ ($R = \hbar c/m_\pi \cong 1.4$ fermi's), then:

$$\begin{aligned} \sqrt{|t_{min}|} &< \frac{1}{R} = m_\pi \\ \frac{M_x^2 - m_p^2}{s} &< \frac{m_\pi}{m_p} \cong 0.15. \end{aligned}$$

This relation, which is known as the coherence condition, defines the condition for diffraction to occur. It can also be written in terms of the fractional momentum of the diffracted proton in the

¹ Expanding the square root terms with $\sqrt{1+x} = 1 + \frac{x}{2} - \frac{x^2}{8} + \frac{x^3}{16} - \dots$ and keeping terms up to order 3 in x .

CHAPTER 1. INTRODUCTION

center of mass frame defined by $x_F = p_{\parallel}^*/p_{\parallel, max}^*$ (where p_{\parallel}^* and $p_{\parallel, max}^*$ are the longitudinal component of the diffracted proton's momentum and its maximum value respectively in this frame). When s is much larger than the masses involved, we have:

$$\begin{aligned}
 M_X^2 &= s - s \frac{E^*}{\sqrt{s}/2} + m_p^2 \\
 &\cong s - s \frac{P_{\parallel}^*}{p_{\parallel, max}^*} + m_p^2 \\
 1 - x_F &\cong \frac{M_X^2 - m_p^2}{s} < 0.15.
 \end{aligned} \tag{1.1}$$

where E^* is the diffracted proton's energy in the center of mass frame.

Reactions of the form $a + b \rightarrow a + X$ are termed *single diffractive*. At high energies, the single diffractive hadronic cross section is found to have the form $d^2\sigma_{diff}^{ab}/dtdM_X^2 \propto e^{-b|t|} \bullet 1/M_X^2$. In the next section, we shall see that this behavior together with the others described above for hadronic interactions is well predicted by Regge phenomenology.

1.2 Regge Phenomenology and the Pomeron

In the days before QCD, the energy dependence of cross sections for hadronic interactions was understood within the context of Regge theory in terms of the exchange of particles associated along a Regge trajectory. The leading or dominant trajectory at high energy, known as the *Pomeronchuk trajectory*, was believed to be responsible for the diffractive nature of high energy elastic scattering. Experimentally observed properties of the high energy diffractive scattering of hadrons were well described in terms of the exchange of this dominant trajectory. This was interpreted by some to represent the exchange of a virtual particle called the *pomeron*. As we shall discuss in Section 1.3, much work in the past two decades has focused on testing the concept and properties of the pomeron within the modern framework of QCD.

1.2. REGGE PHENOMENOLOGY AND THE POMERON

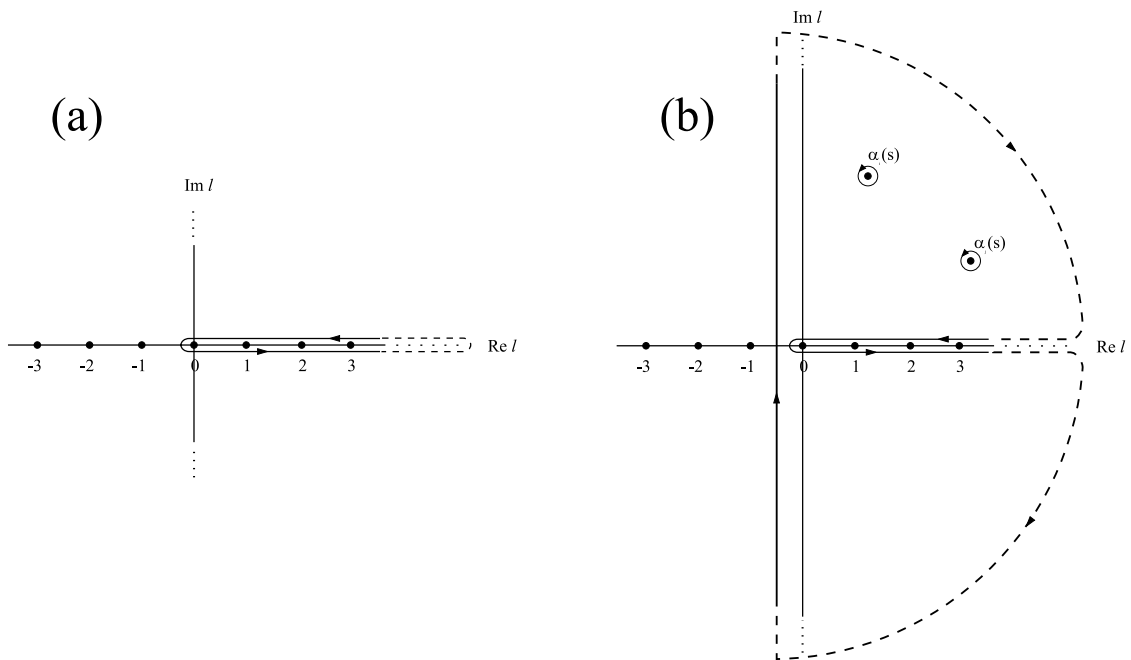


Figure 1.1: Contours used for the scattering amplitude $A(s, t)$ in the complex l plane, (a) before and (b) after applying the Sommerfeld-Watson transformation.

In order to understand the origin of the pomeron, let us first review some relevant aspects of Regge theory [5–9]. We begin with the partial wave expansion of the scattering amplitude² $A(s, t)$ for the reaction $a + b \rightarrow c + d$:

$$A(s, t) = \sum_{l=0}^{\infty} (2l + 1) a_l(s) P_l(z) \quad (1.2)$$

where s is the total energy in the center of mass frame, t is the invariant momentum transfer squared, $a_l(s)$ represents the amplitude for the l 'th partial wave, and $P_l(z)$ are Legendre polynomials with $z = \cos \theta$. The first step taken in Regge theory is to transform the integer valued variable l into one that is continuous and complex. With this modification, the partial wave sum can be replaced with an integral in the complex l -plane over contour (a) shown in Figure 1.1 :

²This also known as the T matrix element.

CHAPTER 1. INTRODUCTION

$$\begin{aligned}
 A(s, t) &= \frac{1}{2i} \oint (2l+1)a_l(s) \frac{P_l(-z)}{\sin \pi l} dl \\
 &= 2\pi i \sum \text{residues} = 2\pi i \sum_{n=0}^{\infty} \frac{1}{2i} \frac{(2l+1)a_l(s)P_l(-z)}{\pi \cos \pi l} \Big|_{l=n} \\
 &= \sum_{n=0}^{\infty} (2n+1)a_n(s)(-1)^n P_n(-z) = \sum_{n=0}^{\infty} (2n+1)a_n(s)P_n(z)
 \end{aligned} \tag{1.3}$$

Using the Sommerfeld-Watson transformation, contour (a) in Figure 1.1 can be deformed into the equivalent one of contour (b) in the same figure [10,11]. Instead of poles from $(\sin \pi l)^{-1}$, the deformed contour now encloses poles from $a_l(s)$ which give rise to residues. Thus, we have:

$$\begin{aligned}
 A(s, t) &= \frac{1}{2i} \int_{-\frac{1}{2}-i\infty}^{-\frac{1}{2}+i\infty} (2l+1)a_l(s) \frac{P_l(-z)}{\sin \pi l} dl \\
 &\quad + \sum_{i=1}^N (2\alpha_i(s)+1) \frac{\beta_i(s)}{\sin \pi \alpha_i(s)} P_{\alpha_i(s)}(-z)
 \end{aligned} \tag{1.4}$$

where the $\beta_i(s)$'s contain the residues of the N poles of $a_l(s)$ at the positions $\alpha_i(s)$. Since $z = \cos \theta = 1 + \frac{t}{2p^{*2}}$ (where p^* is the momentum in the center of mass frame) the asymptotic region where $z \rightarrow \infty$ represents the case when $\sqrt{|t|} \gg p^*$. In this region the Legendre polynomial reduces to $P_l(z) \cong z^{\alpha_i(s)}$ and the integral term in Equation 1.4 vanishes, allowing us to write:

$$A_i(s, t) \cong \frac{\beta_i(s)}{\sin \pi \alpha_i(s)} t^{\alpha_i(s)} \tag{1.5}$$

where various terms not depending on t have been absorbed into $\beta_i(s)$.

The poles represented by $\alpha_i(s)$ are called Regge poles and the paths they trace out in the complex l -plane as a function of s are called Regge trajectories. When the real part of $\alpha_i(s)$ is plotted versus s , it is found that they lie along straight lines. Each line represents a sequence of resonances with increasing mass and intrinsic spin but all having the total charge, baryon number, and strangeness of the initial and final states of the reaction $a + b \rightarrow c + d$. As shown in Figure 1.2, it is found that the experimentally observed hadrons can be organized into families described by Regge trajectories

1.2. REGGE PHENOMENOLOGY AND THE POMERON

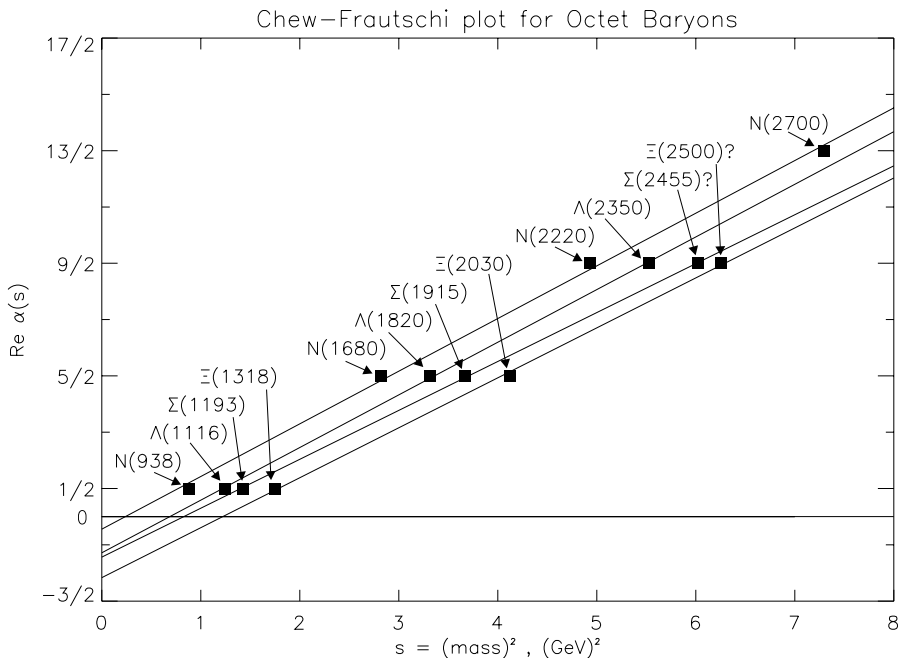


Figure 1.2: Plot of $\text{Re } \alpha_i(s)$ versus s for baryons. Each line is a Regge trajectory connecting baryons of the same family sharing the same quantum numbers I , B , and S but with increasing mass and spin increasing by units of 2.

with members of each family sharing the same quantum numbers I , B , and S . It is also found that the hadrons on each trajectory recur at values of $\alpha_i(s)$ differing by units of 2. Because of this fact, the term $\beta_i(s)$ in Equation 1.5 must include what is called a *signature factor* which causes the cancellation of every other resonance.

The discussion above relates the asymptotic t behavior of the amplitude $A(s, t)$ to Regge poles in the s -channel. In the case of diffractive scattering, we wish to go to the opposite extreme to see if Regge poles in the t -channel can provide information on the behavior of the amplitude $A(s, t)$ when $s \gg t$. To do this, we assume that the partial wave expansion in Equation 1.2 describes the reaction $a + \bar{c} \rightarrow \bar{b} + d$ in the t channel. Invoking crossing symmetry, we then interchange s and t in Equations 1.2-1.5 above to cross over to the s channel reaction $a + b \rightarrow c + d$. Thus, in the high energy, low t region, we may write:

$$A(s, t) \cong \frac{\beta_{\mathcal{P}}(t)}{\sin \pi \alpha_{\mathcal{P}}(t)} s^{\alpha_{\mathcal{P}}(t)} \quad (1.6)$$

CHAPTER 1. INTRODUCTION

where $\alpha_P(t)$ is the leading trajectory furthest to the right in the complex l plane dominating all others when $s \gg t$. In this high energy region, the optical theorem may be written as:

$$\sigma_{\text{tot}} = \frac{1}{s} \text{Im}A(s, 0) \quad (1.7)$$

Combining Equation 1.6 with the optical theorem, we see that:

$$\sigma_{\text{tot}} \propto s^{\alpha_P(0)-1}.$$

Since total cross sections for hadron-hadron collisions tend to constant values at high energy, we find that $\alpha_P(0) = 1$. This dominant Regge trajectory in the high energy limit with $\alpha_P(0) = 1$ is known as the *Pomeranchuk trajectory*. It is assumed to carry the quantum numbers of the vacuum, $I = S = B = 0$, and represents the exchange in the t channel of a virtual particle called the *pomeron*.

The amplitude $A(s, t)$ is a superposition of the amplitudes for the exchanges of all possible Regge trajectories. The exchange of each trajectory can be viewed as an exchange in the t -channel of a virtual particle called a Reggeon of which the pomeron is one particular type. The elastic scattering $a + b \rightarrow a + b$, for instance, can be represented by the exchange diagram shown in Figure 1.3. The index i indicates that we are considering all possible Reggeons that can be exchanged. The amplitude for the exchange illustrated by the diagram is assumed to factorize into a coupling g_{ai} between the exchanged Reggeon i and hadron a , and a coupling g_{bi} between the same Reggeon and hadron b . This is known as Regge factorization.

Using this concept of Regge factorization together with the high-energy behavior of $A(s, t)$ obtained from Regge theory above, we can write down the formulae for the total, elastic, and single diffractive cross sections between two hadrons a and b in the high-energy regime [2, 3]. From the optical theorem in Equation 1.7 above, the total cross section for the reaction $a + b \rightarrow X$ is given

1.2. REGGE PHENOMENOLOGY AND THE POMERON

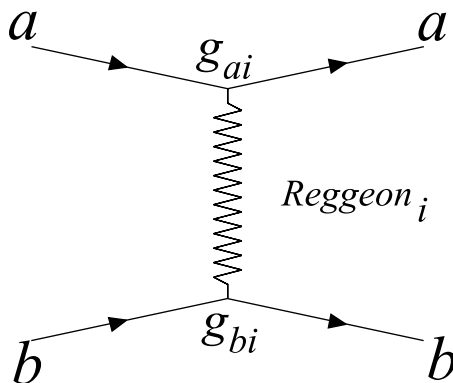


Figure 1.3: Exchange of a Reggeon between hadrons a and b where g_{ai} and g_{bi} are the couplings between the Reggeon and each hadron.

by:

$$\sigma_{\text{tot}}^{ab} = \sum_i \beta_{ai}(0)\beta_{bi}(0)s^{\alpha_i(0)-1}. \quad (1.8)$$

The differential elastic cross section for the reaction $a + b \rightarrow a + b$ can be written as:

$$\begin{aligned} \frac{d\sigma_{\text{el}}^{ab}}{dt} &= \frac{|A(s, t)|^2}{16\pi s^2} \\ &= \sum_i \frac{\beta_{ai}^2(t)\beta_{bi}^2(t)}{16\pi} s^{2[\alpha_i(t)-1]}. \end{aligned} \quad (1.9)$$

The single diffractive cross section for the reaction $a + b \rightarrow a + X$ can be obtained from Mueller's generalization of the optical theorem which relates the inclusive cross section for a reaction $ab \rightarrow cX$ to the forward amplitude for the three body reaction $abc \rightarrow abc$ [12, 13]. The steps involved in applying this generalization to the calculation of the single diffractive cross section are illustrated by the diagrams shown in Figure 1.4. The cross section is represented by diagram (a) which is the square of the amplitude for $a + b \rightarrow a + X$. In the limit of large s and small t , this amplitude "Reggeizes" to the one shown in diagram (b). Mueller's generalization is applied in going from diagram (b) to (c). In the transition from diagram (c) to (e), the amplitude for the process $i + b \rightarrow i + b$ is assumed to Reggeize in the limit of large M_X^2 as indicated by diagram (d). This is based on the same argument as that used in equating diagram (a) with (b). In the present case, the X system

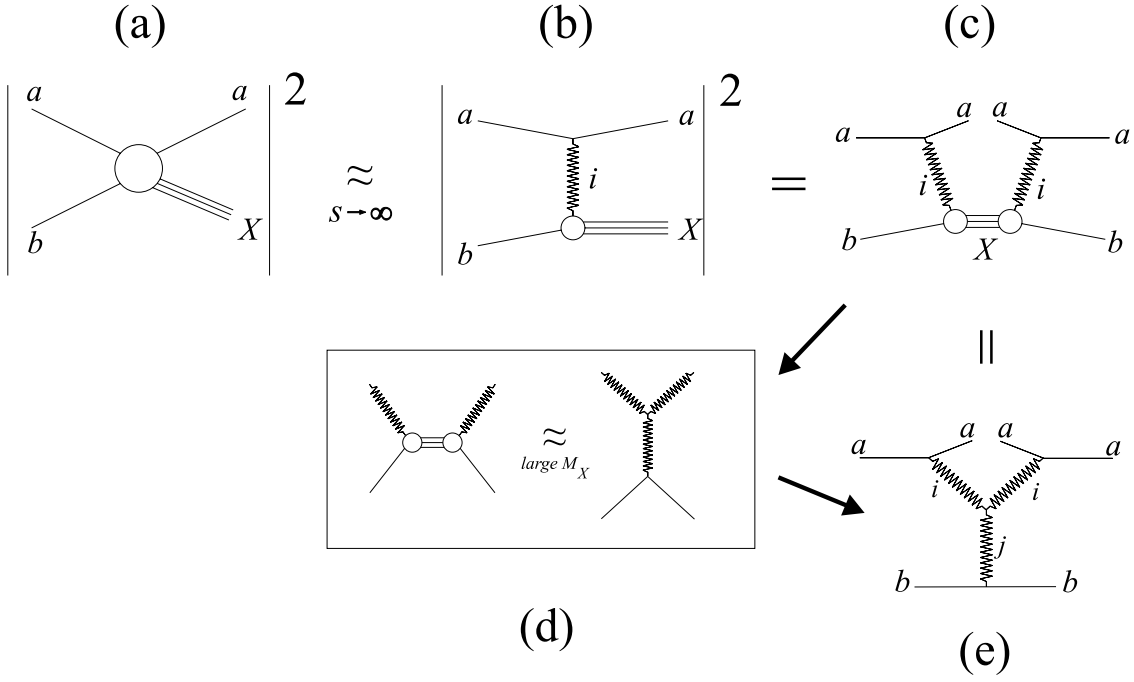


Figure 1.4: Steps leading to the triple Regge diagram in the calculation of the single diffractive cross section for the reaction $a + b \rightarrow a + X$.

mass M_X represents \sqrt{s} in the $i - b$ system. The resulting graph shown in diagram (e) is known as a triple Regge diagram. The single diffractive cross section is determined from this diagram as:

$$\frac{d^2\sigma_{\text{diff}}^{ab}}{dt dM_X^2} = \sum_{i,j} \frac{\beta_{ai}^2(t)\beta_{bj}(0)g_{iij}(t)}{16\pi} \frac{1}{M_X^2} \left(\frac{s}{M_X^2}\right)^{2[\alpha_i(t)-1]} (M_X^2)^{\alpha_j(0)-1} \quad (1.10)$$

where $g_{iij}(t)$ is the triple Regge coupling constant.

We now assume that the dominant trajectory for the three cross sections calculated above is the pomeron trajectory given by:

$$\alpha_{\mathcal{P}}(t) = \alpha_{\mathcal{P}}(0) + \alpha'_{\mathcal{P}}(t)t$$

with $\alpha_{\mathcal{P}}(0) = 1$. With this assumption, the cross sections given by Equations 1.8-1.10 reduce to [2]:

$$\sigma_{\text{tot}}^{ab}(s) = \beta_{a\mathcal{P}}(0)\beta_{b\mathcal{P}}(0) = \text{constant} \quad (1.11)$$

1.3. THE POMERON IN QCD

$$\begin{aligned}
\frac{d\sigma_{\text{el}}^{ab}}{dt} &= \frac{\beta_{a\mathbb{P}}^2(t)\beta_{b\mathbb{P}}^2(t)}{16\pi} s^{2\alpha'(t)t} \\
&= \frac{\sigma_T^2}{16\pi} e^{[b_0(t)+2\alpha'(t)\ln s]t}
\end{aligned}
\tag{1.12}$$

$$\begin{aligned}
\frac{d^2\sigma_{\text{diff}}^{ab}}{dt dM_X^2} &= \frac{\beta_{a\mathbb{P}}^2(t)\beta_{b\mathbb{P}}(0)g_{\mathbb{P}\mathbb{P}\mathbb{P}}(t)}{16\pi} \left(\frac{1}{M_X^2}\right) \left(\frac{s}{M_X^2}\right)^{2\alpha'(t)t} \\
&= \frac{C}{M_X^2} e^{[b_{D,0}(t)+2\alpha'(t)\ln \frac{s}{M_X^2}]t}
\end{aligned}
\tag{1.13}$$

where the results in Equations 1.12 and 1.13 are for small t . These results show that all the major features of hadron-hadron cross sections at high-energy are well described by Regge phenomenology. The total cross section tends toward a constant, the elastic and diffractive cross sections exhibit peaks at low t which shrink logarithmically with s , and the diffractive cross section goes like $1/M_X^2$.

1.3 The Pomeron in QCD

1.3.1 Ingelman and Schlein Model

The previous section discussed the origin of the pomeron within the context of Regge phenomenology. It is the Reggeon representing the intercept of the dominant Regge trajectory possessing the quantum numbers of the vacuum. Beyond that, Regge theory provides no clue to our understanding of the pomeron in terms of its internal structure.

With the arrival of QCD, Low and others [14,15] proposed in the 1970's that the pomeron might have partonic constituents like gluons. In 1985, Ingelman and Schlein [1] took this idea a step further to propose how one might investigate the partonic constituents of the pomeron experimentally. From Regge theory, they thought of a hadronic interaction like the single diffractive reaction $a+b \rightarrow a+X$ as being mediated by a pomeron. From QCD, they gave hadron-like qualities to the pomeron interpreting it as a composite object made up of partons and described by structure functions. Thus the single diffractive process occurs in two steps. In the first step, a pomeron is emitted from

CHAPTER 1. INTRODUCTION

hadron a . In the second step, the constituents of the pomeron from hadron a undergo pointlike hard scattering with those of hadron b giving rise to the system X . To test this model, they suggested looking at events of the type:

$$\bar{p}_i + p \rightarrow \bar{p}_f + (jets + X).$$

Such events would be characterized by high p_T (transverse momentum) jets signaling hard scattering between the partons of the pomeron and proton, and low p_T spectator jets from the non-interacting partons. More importantly, there will be a large rapidity³ gap between the high p_T jets and the scattered antiproton \bar{p}_f . This is because the pomeron which is believed to carry the quantum numbers of the vacuum must be a color singlet. Since it carries no color, there will be no color field between the pomeron and its parent hadron that can fragment into additional hadrons. This leaves a rapidity gap devoid of particles between the parent hadron and the products of the hard scattering.

To see what the Ingelman and Schlein model means in quantitative terms, we follow Goulianos [30] in rewriting the triple Regge cross section for the single diffractive reaction $a+b \rightarrow a+X$ in Equation 1.10 as:

$$\begin{aligned} \frac{d^2\sigma_{\text{diff}}^{ab}}{dt dM_X^2} &= \frac{\beta_a^2(t)\beta_b(t)g_{\mathbb{P}\mathbb{P}\mathbb{P}}(t)}{16\pi} \frac{1}{M_X^2} \left(\frac{s}{M_X^2}\right)^{2[\alpha_{\mathbb{P}}(t)-1]} (M_X^2)^{\alpha_{\mathbb{P}}(0)-1} \\ &= \frac{\beta_a^2(t)}{16\pi} \frac{1}{M_X^2} \left(\frac{s}{M_X^2}\right)^{2[\alpha(t)-1]} \left[\beta_b(0)g(t) (M_X^2)^{\alpha(0)-1}\right] \end{aligned}$$

where we assume dominance of the pomeron trajectory and have dropped the \mathbb{P} index in the second line. We recall that it is the property of Regge factorization discussed in the previous section that allows us to write the cross section in the form of Equation 1.10. Changing the integration variable

³Rapidity is defined as $y = \frac{1}{2} \ln \left(\frac{E+P_L}{E-P_L} \right)$ where E is the energy of particle and P_L its longitudinal momentum.

1.3. THE POMERON IN QCD

from M_X^2 to $x_{\mathcal{P}} = M_X^2/s$, we have:

$$\begin{aligned}
\frac{d^2\sigma_{\text{diff}}^{ab}}{dt dx_{\mathcal{P}}} &= \frac{\beta_a^2(t)}{16\pi} \frac{s}{M_X^2} \frac{M_X^2}{s} \left(\frac{s}{M_X^2}\right)^{2\alpha(t)-1} \left[\beta_b(0)g(t) (M_X^2)^{\alpha(0)-1}\right] \\
&= \left[\frac{\beta_a^2(t)}{16\pi} x_{\mathcal{P}}^{1-2\alpha(t)}\right] \times \left[\beta_b(0)g(t) (M_X^2)^{\alpha(0)-1}\right] \\
&= f_{\mathcal{P}/a}(x_{\mathcal{P}}, t) \times \sigma_{\text{tot}}^{\mathcal{P}b}(M_X^2).
\end{aligned} \tag{1.14}$$

The terms enclosed by the second set of brackets in the second line are similar in form to Equation 1.8 and represent the total cross section $\sigma_{\text{tot}}^{\mathcal{P}b}(M_X^2)$ between the pomeron \mathcal{P} and hadron b . The terms enclosed in the first set of brackets is the pomeron flux $f_{\mathcal{P}/a}(x_{\mathcal{P}}, t)$ representing the probability of finding a pomeron in hadron a and depends only on the variables $x_{\mathcal{P}}$ and t . We now consider the diffractive production of jets described by the reaction $a + b \rightarrow a + jets + X$. The cross section term in Equation 1.14 will now represent the total $\mathcal{P} - b$ cross section for the production of jets. Using the parton model for hadron-hadron collisions, this cross section can be written as:

$$\begin{aligned}
\frac{d^2\sigma_{\text{diff}}^{jets}}{dt dx_{\mathcal{P}}} &= f_{\mathcal{P}/a}(x_{\mathcal{P}}, t) \times \sigma_{\text{tot}}^{\mathcal{P}b \rightarrow jets}(M_X^2) \\
&= f_{\mathcal{P}/a}(x_{\mathcal{P}}, t) \\
&\times \sum_{i,j} \int \frac{dx_i}{x_{\mathcal{P}}} \int dx_j f_{i/\mathcal{P}}\left(\frac{x_i}{x_{\mathcal{P}}}, Q^2\right) f_{j/b}(x_j, Q^2) \hat{\sigma}_{ij}^{jets}(\hat{s}, Q^2)
\end{aligned}$$

where we consider only leading order $2 \rightarrow 2$ QCD scattering processes. The sum is over all possible types of partons i present in pomeron \mathcal{P} and partons j in hadron b . x_i and x_j are the momentum fractions. We note that $x_{\mathcal{P}}$ can also be defined in this manner representing the fractional momentum of the pomeron. $f_{i/\mathcal{P}}(x_i/x_{\mathcal{P}}, Q^2)$ is the density of partons of type i carrying a fraction $x_i/x_{\mathcal{P}}$ of the pomeron momentum and $f_{j/b}(x_j, Q^2)$ is the density of partons of type j with momentum fraction x_j . $\hat{\sigma}_{ij}^{jets}(\hat{s}, Q^2)$ is the subprocess cross section for $i + j \rightarrow jets$, \hat{s} is the center of mass energy squared in the $i - j$ system and Q^2 is the characteristic momentum scale. The central idea in the Ingelman-Schlein picture is that the diffractive cross section can be factorized into a pomeron flux

and a total pomeron-hadron cross section. Because of this property, the structure of the pomeron, described in terms of parton density functions, must be universal and independent of the process of emission.

1.3.2 Experimental Investigation of the Pomeron Structure

In 1988, the UA8 collaboration found evidence for the partonic structure of the pomeron at the CERN SPS collider with $\sqrt{s} = 630$ GeV [16, 17]. High transverse energy jets produced by the reaction $p + \bar{p} \rightarrow p + (jets + X)$ were observed in which the quasi-elastically scattered final state proton possessed more than 90% of the initial beam proton momentum ($x_F > 0.9$ for the scattered proton). In comparing their data with Monte Carlo, they assumed the pomeron to be composed only of gluons with *soft* and *hard* density functions described, respectively, by $xG(x) = 6(1-x)^5$ and $xG(x) = 6x(1-x)$ where x is the fraction of the pomeron's momentum taken by the gluon. The hard structure function represented their data better but a "super-hard" component was also required in which a gluon in the pomeron took up nearly all of its momentum.

The structure of the pomeron has also been investigated by deep inelastic electron proton scattering (DIS) experiments at DESY using the HERA ep collider [18]. In conventional DIS, the interaction takes place between the electron and the charged quarks in the proton. Using 26.7 GeV electrons and 820 GeV protons, the ZEUS collaboration found a class of DIS events with a large rapidity gap between the scattered proton and the hadrons produced by the electron proton interaction. Such events are called diffractive DIS events and involve the scattering of an electron with quarks in the pomeron. The cross section for diffractive DIS is written in the same form as conventional DIS:

$$\frac{d^4\sigma_{\text{diff}}}{dx_{\mathcal{P}} dt dx dQ^2} = \frac{2\pi\alpha^2}{xQ^4} [1 + (1-y)^2] F_2^{D(4)}(x, Q^2, x_{\mathcal{P}}, t) \quad (1.15)$$

where $x_{\mathcal{P}}$ and t are as defined previously, α is the electromagnetic coupling constant, $F_2^{D(4)}$ is the diffractive structure function, x is the fractional momentum of the pomeron taken by the quark,

1.3. THE POMERON IN QCD

$Q^2 = -\hat{t}$, and $y = -\hat{t}/\hat{s}$, where \hat{s} and \hat{t} are the square of the total energy and momentum transfer in the electron-quark system. From the Ingelman-Schlein model, the diffractive structure function may be factorized into the pomeron flux and the pomeron structure function:

$$F_2^{D(4)}(x, Q^2, x_{\mathcal{P}}, t) = f_{\mathcal{P}}(x_{\mathcal{P}}, t) \times F_2^{\mathcal{P}}(x, Q^2). \quad (1.16)$$

From QCD, the pomeron structure function may be written as:

$$F_2^{\mathcal{P}}(x, Q^2) = \sum_i e_i^2 x f_{i/\mathcal{P}}(x, Q^2) \quad (1.17)$$

where e_i is the charge of the quark, $f_{i/\mathcal{P}}(x, Q^2)$ is the quark distribution function in the pomeron and the sum is over all quark types in the pomeron. In 1995, the ZEUS collaboration reported their measurements of the diffractive structure function in DIS which provides information on the quark distributions in the pomeron. They also reported measurements of the diffractive dijet cross sections in photoproduction which, unlike diffractive DIS, is sensitive to both the quark and gluon densities in the pomeron. Combining the diffractive DIS and photoproduction measurements, they estimated that the gluon content of the pomeron is between 30% to 80% [19].

Programs to study the nature of the pomeron have also been undertaken by the CDF and D0 collaborations at Fermilab. The CDF collaboration has reported observations of the diffractive production of W -bosons, dijets, and b -quarks in $p\bar{p}$ collisions at $\sqrt{s} = 1800$ GeV at the Tevatron [20–22]. Their results are reported as ratios of diffractive to non-diffractive events. These ratios for W -bosons, dijets, and b -quarks are as follows:

$$\begin{aligned} R_W &= [1.15 \pm 0.51(\text{stat}) \pm 0.2(\text{syst})]\% \\ R_{JJ} &= [0.75 \pm 0.05(\text{stat}) \pm 0.09(\text{syst})]\% \\ R_{\bar{b}b} &= [0.62 \pm 0.19(\text{stat}) \pm 0.16(\text{syst})]\%. \end{aligned} \quad (1.18)$$

The production of W -bosons is sensitive only to the quark distributions in the pomeron while that of the dijets and b -quarks are sensitive to both quark and gluon distributions. By combining all three results, the fraction of gluons in the pomeron was found to be $f_g = 0.54_{-0.14}^{+0.16}$, which is consistent with the result found by ZEUS at HERA mentioned above.

1.3.3 Breakdown of Factorization in the Ingelman-Schlein Model

As mentioned in Section 1.3.1, if the concept of factorization introduced by Ingelman and Schlein is correct, the partonic structure of the pomeron must be universal and independent of the process by which the pomeron is emitted. This means that one should be able to extract parton density functions of the pomeron from DIS and photoproduction data obtained at ep colliders, for instance, and apply them to predict diffractive cross sections at $p\bar{p}$ colliders. This is, in fact, what Alvero *et al.* [24] and others have done [25, 26]. Alvero *et al.* assumed the following forms for the quark and gluon distributions of the pomeron in Equation 1.17:

$$\begin{aligned} x f_{q/\mathbb{P}}(x, Q^2) &= a_q [x(1-x) + \tilde{a}_q (1-x)^2] \\ x f_{g/\mathbb{P}}(x, Q^2) &= a_g x(1-x) \end{aligned} \tag{1.19}$$

for their first four parametrizations and the following forms:

$$\begin{aligned} x f_{q/\mathbb{P}} &= a_q x(1-x) \\ x f_{g/\mathbb{P}} &= a_g x^8 (1-x)^{0.3} \end{aligned} \tag{1.20}$$

for what they termed their *super-hard gluon* parametrization. For the pomeron flux factor in Equation 1.16, they used the Donnachie-Landshoff form [27, 28]. With these assumptions, they obtained fits to the diffractive structure function $F_2^{D(3)}(x, Q^2, x_{\mathbb{P}})$ in DIS and the diffractive dijet cross sec-

1.3. THE POMERON IN QCD

tions in photoproduction from HERA to determine the parameters a_q , \tilde{a}_q , and a_g .⁴ The results from these fits were then used to predict cross sections for the diffractive production of W -bosons and dijets in $p\bar{p}$ collisions at the Fermilab energy of $\sqrt{s} = 1800$ GeV. Comparing the predictions from their *realistic*⁵ fits with the measured cross sections from the CDF collaboration at Fermilab [20–22], they found the predictions for W -bosons to be 3-6 times larger than the measured results and predictions for dijets to be 3-22 times larger. Comparisons with preliminary data for diffractive dijet production from the D0 collaboration at Fermilab also gave similar results [23].

The CDF collaboration at Fermilab also compared their measurements of the diffractive W -boson, dijet, and b -quark cross sections with predictions from POMPYT [29] which is a Monte Carlo generator based on the Ingelman-Schlein model. They plotted a discrepancy factor D , which is the ratio of their measured rates shown in Equation 1.18 to the predicted rates from POMPYT, as a function of the gluon fraction in the pomeron [22]. From the plot shown in Figure 1.5, they determined this ratio to be $D = 0.19 \pm 0.04$ with $R_g = 0.54_{-0.14}^{+0.16}$.

The results of the comparisons between predictions and measurements described above show that the experimental cross sections are significantly lower than the expected results based on the Ingelman-Schlein model. This discrepancy indicates the breakdown of factorization as proposed by this model.

1.3.4 Renormalization of the Pomeron Flux

Regge phenomenology, as described in Section 1.2, has done remarkably well in describing the essential features of hadronic cross sections at high energies. More recent results from data acquired at much higher energies, however, have uncovered a serious problem. Recent measurements made

⁴ $F_2^{D(3)}$ is identical to $F_2^{D(4)}$ in Equation 1.15 but integrated over the variable t . $F_2^{D(3)}$ was used since t was not measured by ZEUS.

⁵These are fits that contain gluons, i.e. where a_g in the parton density functions of Equations 1.19 and 1.20 were not set to zero.

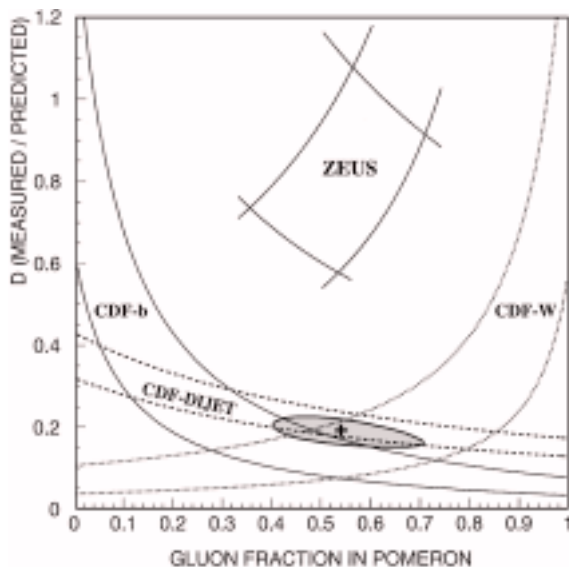


Figure 1.5: The ratio D of measured to predicted diffractive rates as a function of the gluon content of the Pomeron, R_g , from Reference [22].

by collider experiments at Fermilab and CERN show that the total single diffractive $p\bar{p}$ cross section rises much more slowly as a function of energy than the predictions of *standard* Regge theory [30,31]. This behavior is clearly seen in Figure 1.6 which compares the steeply rising prediction of standard Regge theory (dashed line) with recent data from experiments. The standard Regge theory prediction is based on the triple Regge formula of Equation 1.14 with a *standard* pomeron flux factor given by:

$$f_{\mathcal{P}/p}(x_{\mathcal{P}}, t) = \frac{\beta_1^2(t)}{16\pi} x_{\mathcal{P}}^{1-2\alpha(t)} = \frac{\sigma_0^{pp}}{16\pi} x_{\mathcal{P}}^{1-2\alpha(t)} F^2(t) \quad (1.21)$$

where $\sigma_0^{pp}/16\pi = 0.73 \text{ GeV}^{-2}$ and $F^2(t)$ is the proton form factor.

To remedy this situation, Goulianos [30] proposed renormalizing the pomeron flux factor according to the following prescription:

$$f_N(x_{\mathcal{P}}, t) = \frac{f_{\mathcal{P}/p}(x_{\mathcal{P}}, t) dx_{\mathcal{P}} dt}{N(x_{\mathcal{P}}^{min})} \quad (1.22)$$

where :

$$N(x_{\mathcal{P}}^{min}) = 1 \quad \text{if } A(x_{\mathcal{P}}^{min}) \leq 1$$

1.3. THE POMERON IN QCD

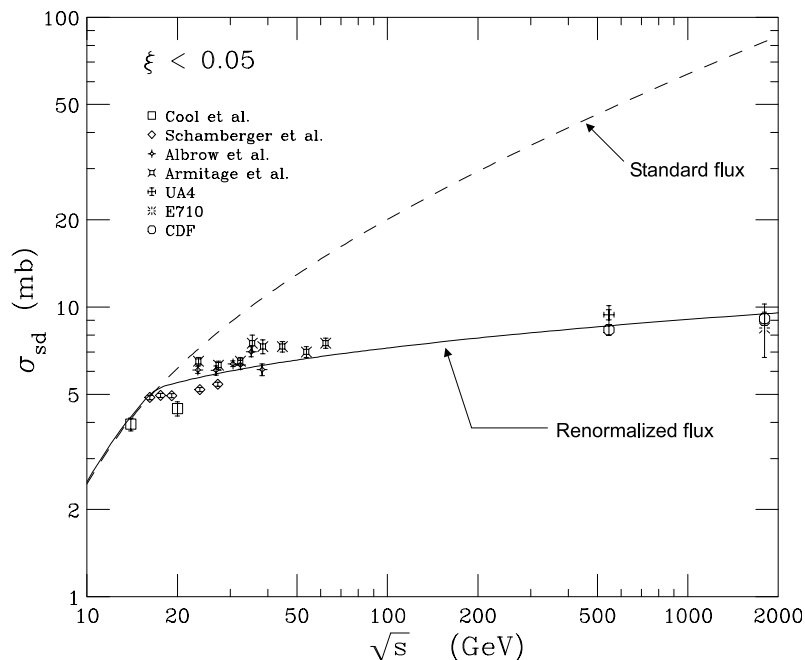


Figure 1.6: Comparison of the total single diffractive $p\bar{p}$ cross section predicted by Regge theory using the standard flux of Equation 1.21 (dashed line) with recent experimental results. The solid line is the Regge theory prediction with the renormalized flux of Equation 1.22. This plot is taken from Reference [31].

$$N(x_{\mathbb{P}}^{min}) = A(x_{\mathbb{P}}^{min}) \quad \text{if } A(x_{\mathbb{P}}^{min}) > 1$$

$$A(x_{\mathbb{P}}^{min}) = \int_{x_{\mathbb{P}}^{min}}^{x_{\mathbb{P}}^{max}} dx_{\mathbb{P}} \int_{t=0}^{\infty} f_{\mathbb{P}/p}(x_{\mathbb{P}}, t) dt.$$

Thus, the standard flux is divided by its integral over all available phase space when this integral exceeds unity. This effectively sets the maximum number of pomerons per proton to unity. With this modified form of the flux, the triple Regge formula correctly describes the energy behavior of the single diffractive cross section up to the TeV scale. This agreement with data is shown by the solid line in Figure 1.6.

From these results, one may ask whether the breakdown of the Ingelman-Schlein model applied to hard diffractive processes might be due to the improper normalization of the pomeron flux factor. Goulianos calculated the ratio of the flux integral $N(x_{\mathbb{P}}^{min})$ for the ep experiments at HERA to that for the $p\bar{p}$ experiments at the Fermilab Tevatron and found it to be $\cong 0.19$ [32]. This value is

consistent with the value of $D = 0.19$ determined by the CDF collaboration from Figure 1.5. This suggests that the breakdown of factorization described in the previous section can be accounted for by the scaling behaviour of the pomeron flux.

1.4 Gap Survival Probability

Although the phenomenological approach of renormalizing the pomeron flux seems to account for the disagreements between the HERA and Fermilab results, the sources of the disagreement still need to be understood. As previously mentioned, diffractive events are thought to proceed via pomeron exchange. Because the pomeron carries no color, a large rapidity gap devoid of hadronic activity is left between the parent hadron of the pomeron and the products from its subsequent interaction. One of the current approaches to understanding the breakdown of factorization in the Ingelman and Schlein model is to think in terms of a *gap survival probability* [34–36]. This approach can be traced back to Bjorken who proposed using large rapidity gaps as a signal for Higgs production via W - W fusion [33]. Let us use F_s to denote the ratio of the cross section of diffractive events mediated by pomeron exchange to that of non-diffractive inelastic events mediated by gluon exchange. According to this approach, if large rapidity gaps are used to identify diffractive events, then the ratio F_s cannot be measured directly and must be modified according to:

$$f_{gap} = \langle |S|^2 \rangle F_s.$$

The measurable quantity f_{gap} is equal to the original ratio F_s multiplied by a factor $\langle |S|^2 \rangle$ representing the survival probability of the gap. This factor takes into account gap destroying mechanisms ignored in the simple picture of Ingelman and Schlein. These can include gluon radiation from the partons involved in the hard scattering process or, in the case of hadron-hadron diffraction, soft color exchanges involving the spectator partons of the interacting hadrons. Such mechanisms populate

1.5. DIFFRACTIVE CHARM PRODUCTION

the rapidity gap with additional hadrons and thereby destroy the gap. Thus $\langle |S|^2 \rangle$ represents the probability that the gap due to pomeron exchange will not be filled by the hadronic products from such mechanisms. The renormalized flux of Goulianos can also be interpreted in these terms, as a probability distribution for gap survival.

In this picture, the gap survival probability is expected to be lower for $p\bar{p}$ collisions than for the DIS or photoproduction experiments at HERA because there are more spectator partons involved in the former. Due to increased parton densities at higher center of mass energies, this probability is also expected to decrease with increasing energy. Thus, the lower rates observed at Fermilab compared to expectations based on HERA results may be due to gap breakdown mechanisms such as those described above. Aside from such statements on the general behavior of $\langle |S|^2 \rangle$, there is currently no detailed understanding of the mechanisms responsible for gap destruction. This is understandable due to the extremely complicated nature of the interactions involved especially in hadron-hadron collisions. Evidently, more data involving different processes and at different energies is needed.

1.5 Diffractive Charm Production

The observation of large Λ_c cross sections ($\simeq 500 \mu\text{b}$) over two decades ago at the CERN ISR [39–44] prompted speculation of a large diffractive component in the hadroproduction of charm. One model proposed by Brodsky *et al.* [45, 46] suggested intrinsic charm states within the proton which could be diffractively excited. It was thought that such explanations could account for the large discrepancies between the ISR results and existing theoretical calculations. However, a number of developments in the late 80's and early 90's made it necessary to re-examine this view. Higher quality data from second generation charm experiments showed that the total charm cross sections ($\simeq 20\text{--}30 \mu\text{b}$) were significantly lower than the ISR measurements [47]. Next to leading order QCD calculations also increased the cross sections by a factor of 3 from previous leading order calculations making them

CHAPTER 1. INTRODUCTION

compatible with the newer measurements [48–50]. This led to serious doubts regarding the ISR results and the solutions proposed to explain them.

Today, the diffractive production of charm is viewed using the model of Ingelman and Schlein. The diffractive production of heavy quarks like c and b involves a hard scattering process between the interacting partons that can be easily described using this model. In this model, the diffractive charm cross section between two protons 1 and 2 in the reaction $1 + 2 \rightarrow 1 + (c\bar{c} + X)$ can be written as:

$$\begin{aligned} \frac{d^2\sigma_{\text{diff}}^{c\bar{c}}}{dt dx_{\mathcal{P}}} &= f_{\mathcal{P}/1}(x_{\mathcal{P}}, t) \int \frac{dx_1}{x_{\mathcal{P}}} \int dx_2 \\ &\times \left[f_{q/\mathcal{P}}\left(\frac{x_1}{x_{\mathcal{P}/1}}, Q^2\right) f_{q/2}(x_2, Q^2) \hat{\sigma}_{qq}^{c\bar{c}}(\hat{s}, Q^2) \right. \\ &\left. + f_{g/\mathcal{P}}\left(\frac{x_1}{x_{\mathcal{P}/1}}, Q^2\right) f_{g/2}(x_2, Q^2) \hat{\sigma}_{gg}^{c\bar{c}}(\hat{s}, Q^2) \right] \end{aligned} \quad (1.23)$$

where the indices q and g indicate quarks and gluons. $f_{q/\mathcal{P}}$ and $f_{g/\mathcal{P}}$ are the parton distribution functions in the pomeron from proton 1 and $f_{q/2}$ and $f_{g/2}$ are the parton distribution functions in proton 2. Only the two major subprocesses for charm production, $qq \rightarrow c\bar{c}$ and $gg \rightarrow c\bar{c}$, are considered here with $\hat{\sigma}_{qq}^{c\bar{c}}$ and $\hat{\sigma}_{gg}^{c\bar{c}}$ representing their cross sections.

Assuming zero quark contribution, Fritzsche and Streng [37] calculated this cross section using a flux factor parametrized by a fit of UA4 data and assuming a pomeron-proton cross section of $\cong 1$ mb. For $x_{\mathcal{P}} = M_X^2/s \leq 0.1$ and a hard gluon distribution of the form $f_{g/\mathcal{P}}(z) = 6(1-z)$ (where $z = x/x_{\mathcal{P}}$), their calculations yielded a cross section of $\cong 0.4 \mu\text{b}$ at $\sqrt{s} = 40$ GeV. This estimate was consistent with the findings of E653 at Fermilab which found no evidence for diffractively produced charm in proton-Si interactions at 800 GeV/c [38]. Their upper limit of $\sigma_{\text{diff}}^{c\bar{c}} < 26 \mu\text{b}/\text{Si nucleus}$ is equivalent to $\sigma_{\text{diff}}^{c\bar{c}} < 2.8 \mu\text{b}$ for the proton-proton case if the cross section is assumed to scale with atomic weight as $A^{2/3}$ and to $\sigma_{\text{diff}}^{c\bar{c}} < 0.93 \mu\text{b}$ if it scales as A .

No measurement of diffractively produced charm in hadronic interactions exists. The first goal of this dissertation is, therefore, to provide a measurement of the diffractive charm cross section in pp

1.5. DIFFRACTIVE CHARM PRODUCTION

interactions at $\sqrt{s} = 40$ GeV. Secondly, there is no experimental data for hard diffractive scattering processes of any kind in this energy range. Thus, the second goal is to compare this measurement with predictions based on the Ingelman-Schlein model and with other diffractive hard scattering data from HERA and Fermilab. Doing so will test the predictions of the Ingelman-Schlein picture of diffraction in this energy range. It will also provide information on the role played by mechanisms proposed to explain the discrepancies discussed in Section 1.3.3 and their possible dependence on energy.

CHAPTER 1. INTRODUCTION

Chapter 2

Experimental Apparatus

Experiment E690 investigated proton-proton collisions using an $800 \text{ GeV}/c$ proton beam incident on a liquid hydrogen target. A member list of the E690 collaboration is shown in Appendix A. E690 acquired data during the fixed target run of 1991 at Fermilab. The E690 detector apparatus was located in Lab G of the east neutrino experimental area (NE). Figure 2.1 shows a schematic diagram of the E690 detector. It consisted of two separate spectrometers, a beam spectrometer and a multi-particle spectrometer. The beam spectrometer measured both the incoming and scattered beam

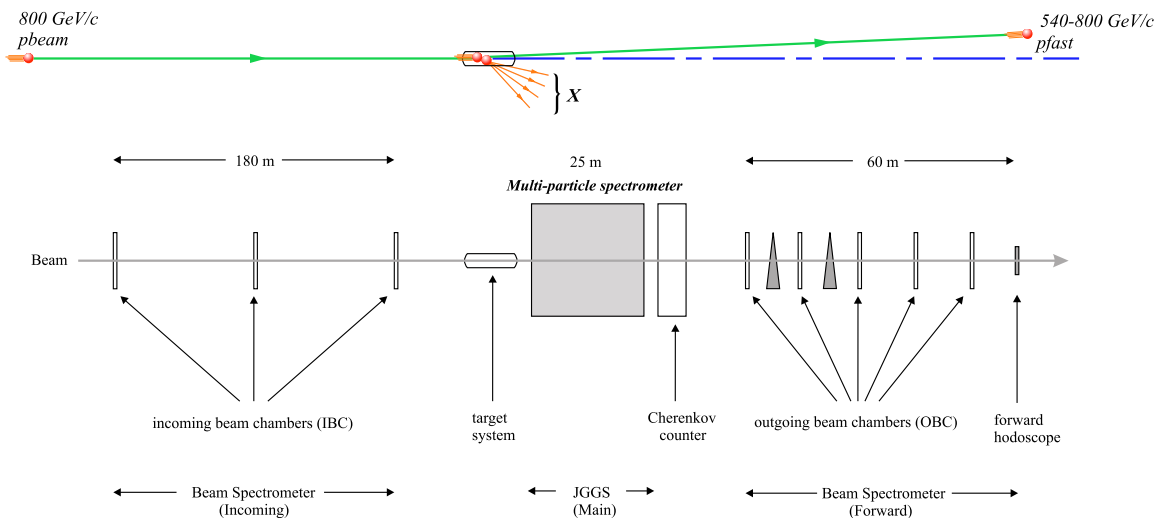


Figure 2.1: Block diagram of the E690 detector (not to scale).

proton allowing a determination of its energy loss after interaction in the liquid hydrogen target. The multi-particle spectrometer measured the charged particle tracks produced by the beam proton's interaction in the liquid hydrogen target. This chapter briefly describes the major components of each spectrometer subsystem followed by a description of the data acquisition system used in recording the events on tape. More detailed descriptions can be found in References [51–53] and references therein.

2.1 Beam Spectrometer

The beam spectrometer was made up of two separate sections, an incoming beam spectrometer upstream of the multi-particle spectrometer and a forward spectrometer downstream of the multi-particle spectrometer. A description of the beamline and the two sections of the beam spectrometer follows.

2.1.1 Beamline

Beam protons extracted from the main ring were delivered to the E690 apparatus via the neutrino east beamline. The proton beam had a momentum of 800 GeV/c with a dispersion of $\Delta p/p < 1.5 \times 10^{-4}$. These protons were delivered every 60 seconds in spills lasting 20 seconds. Beam intensity was controlled by a pinhole located about 935 meters upstream of the liquid hydrogen target providing an average of about 10^8 protons per spill. The beam profile at the target was a ribbon measuring about 20 mm wide by 2 mm high.

2.1.2 Incoming Beam Spectrometer

The incoming spectrometer had an overall length of about 183 meters. It was made up of three drift chamber measuring 6" \times 4". Each drift chamber had four anode planes sandwiched between five cathode planes and two ground planes. The anode plane wires were oriented at angles of -21.6° ,

2.2. MULTI-PARTICLE SPECTROMETER

-7.93°, 7.93°, and 21.6° relative to the vertical axis while the cathode and ground plane wires were vertical. The gas mixture used for the chambers was 82% Argon, 15% Isobutane and 3% Methylal. The design and performance of these chambers are described in greater detail in Ref. [54]. The incoming spectrometer measured the incident beam proton's slope to $\pm 10^{-6}$ rad.

2.1.3 Forward Spectrometer

The outgoing beam spectrometer measured a total length of about 57 meters. It consisted of five drift chambers. The first three chambers were identical to those used in the incoming beam spectrometer. The last two chambers were similar but had a wider aperture measuring 15" \times 8". In between the first three chambers was a string of five magnets that provided an average transverse momentum kick of 12 GeV/c. These magnets allowed momentum lost by the beam proton after interaction in the liquid hydrogen target to be measured with a resolution of $\sigma \leq 0.4$ GeV/c for the longitudinal component and $\sigma \simeq 7$ MeV/c for the transverse component. Acceptance of the forward spectrometer was $\simeq 540$ to 800 GeV/c for the longitudinal component of the momentum and ≤ 0.8 GeV/c for the transverse component.

2.2 Multi-particle Spectrometer

The multi-particle spectrometer was made up of a liquid hydrogen target, several groups of counters, six drift chambers numbered 1-6 and a spectrometer magnet. The liquid hydrogen target provided the target protons. The counters were used for both triggering the data acquisition system and particle identification. The drift chambers and the spectrometer magnet were used for measuring the trajectories and momenta of the charged particles produced by the interaction in the target. Figure 2.2 shows a perspective view of the detector elements in the multi-particle spectrometer.

CHAPTER 2. EXPERIMENTAL APPARATUS

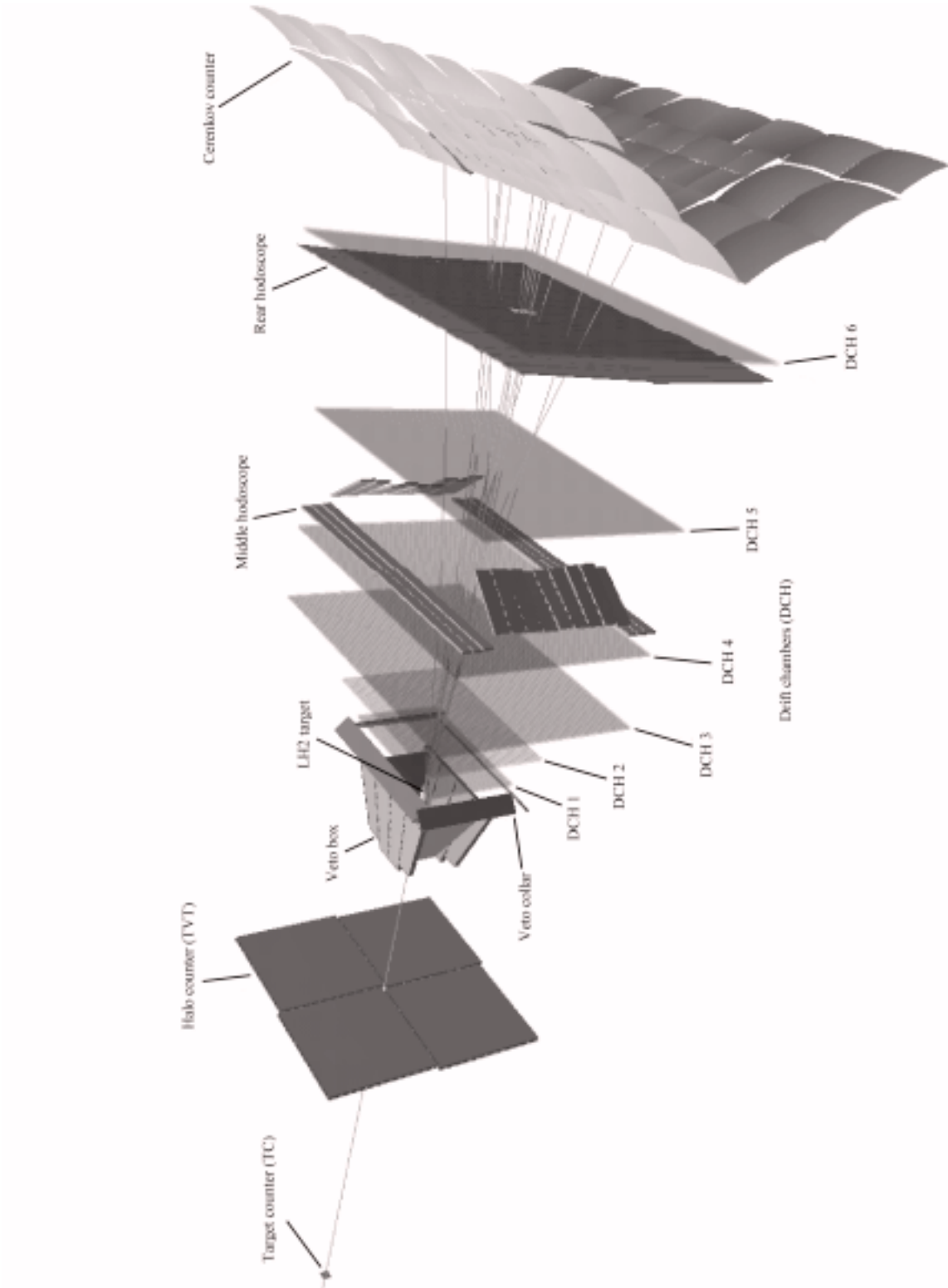


Figure 2.2: Detector elements of the E690 multi-particle spectrometer.

2.2. MULTI-PARTICLE SPECTROMETER

2.2.1 Target Counter (TC) and Halo Counter (TVT)

The target counter was located about 3.5 meters upstream of the liquid hydrogen target. It was made of a .08" thick 2" × 2" square scintillator attached to a phototube. The target counter signalled the arrival of an incident beam proton and provided the initial time, T_0 , relative to which the arrival times of signals from other detector components were measured.

About 2.3 meters downstream of the target counter was the halo counter. It was made of four 24" × 24" slabs of scintillator arranged around the beam axis providing a rectangular aperture in the beam path measuring 1.25" wide by 0.5" high. This counter was used to reject incident protons accompanied by beam halo.

2.2.2 Target System

A diagram of the E690 target system is shown in Figure 2.3. The target consisted of a mylar flask filled with liquid hydrogen. The flask was a 1.5" diameter (I.D.) cylinder with semi-spherical end caps measuring a total length of 5.625". The liquid hydrogen provided a 2% interaction length for the incident beam proton. For thermal insulation, the flask was surrounded by an evacuated foam ball made of 0.2" thick Rohacell 71 with an external radius of 3.2". A fiberglass outer shell provided structural rigidity for the foam ball. The flask and foam ball were enclosed in a box with upstream and downstream windows made of 0.002" thick Kapton. This box was filled with He to minimize ionization losses and multiple scattering of the particles produced by the interaction in the target.

2.2.3 Veto Counters

Surrounding the target box was the veto box, a group of twelve counters forming a truncated pyramid whose axis was aligned along that of the beam. The upstream face of the pyramid formed an aperture measuring 4" wide by 8" high while the downstream face which was the base of the pyramid formed a 12" wide by 22" high aperture. Each counter was made up of four pieces of lead sandwiched in

CHAPTER 2. EXPERIMENTAL APPARATUS

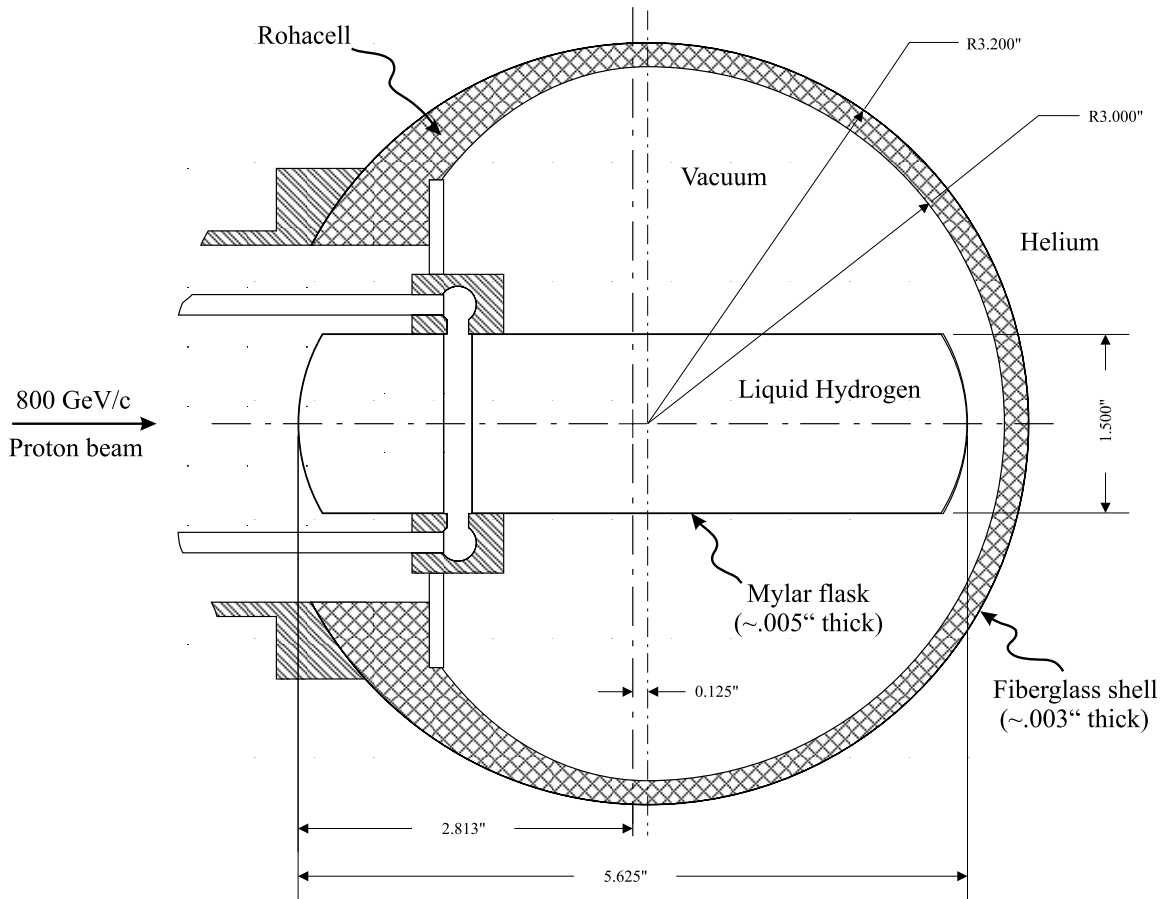


Figure 2.3: E690 target system.

five pieces of scintillator. For certain portions of the run the veto box was used to reject events with charged or neutral particles produced at large angles with respect to the beam direction that would miss the detector aperture.

The veto collar was made of four pieces of 4" wide scintillators forming a rectangular frame right in front of the first drift chamber with an aperture measuring roughly 30" \times 18". The counters that formed the top and bottom of the frame were 33" long while those that formed the sides of the frame were 21" long. The veto collar detected large angle tracks missing the detector aperture that did not hit counters in the veto box.

2.2.4 Middle and Rear Hodoscopes

Located about 1.3 meters downstream of the target in the mid-plane of the E690 detector and right behind drift chamber 4 was the middle hodoscope. The middle hodoscope was made of two types of 0.5" thick rectangular scintillation counters. The long counters measured 30" in length and 2" in width. The short counters were 11.75" long and 3.1" wide. Thirty of these counters were arranged to form a frame measuring roughly 60" \times 40". Each side of the frame was made from nine stacked pieces of short counters with the axes along the shorter edges of their rectangular faces aligned along the vertical and the normals to these faces forming an angle with the beam axis. The top and bottom edges of the frame were each made from six pieces of the long counters. The middle hodoscope detected low momentum particles that left the detector aperture before reaching the rear hodoscope. A perspective view of the middle hodoscope is provided in Figure 2.4.

The rear hodoscope was positioned about 2.4 meters downstream of the target right in front of drift chamber 6. It was made up of 72 pieces of 0.25" thick rectangular scintillation counters measuring 24" long and 2" wide. The counters were arranged to form a rectangular 72" \times 48" array the size of drift chamber 6. Figure 2.4 shows a perspective view of the rear hodoscope. Counters 18, 19, 54, and 55 were 2" shorter than the other counters creating a 4" \times 4" square aperture in the center of the array along the beam path.

The middle and rear hodoscope were used in the triggers of the data acquisition system described in Section 2.3 to signal the presence of charged tracks produced by the interaction in the liquid hydrogen target. They were also used to make time-of-flight measurements for particle identification. The average width of the time distributions ($t_{\text{measured}} - t_{\text{predicted}}(\pi, K, p)$) for all counters in both middle and rear hodoscopes was $\sigma \simeq 400$ ps for pions, kaons, and protons ranging from a low of $\sigma \simeq 300$ ps to a high of $\sigma \simeq 600$ ps.

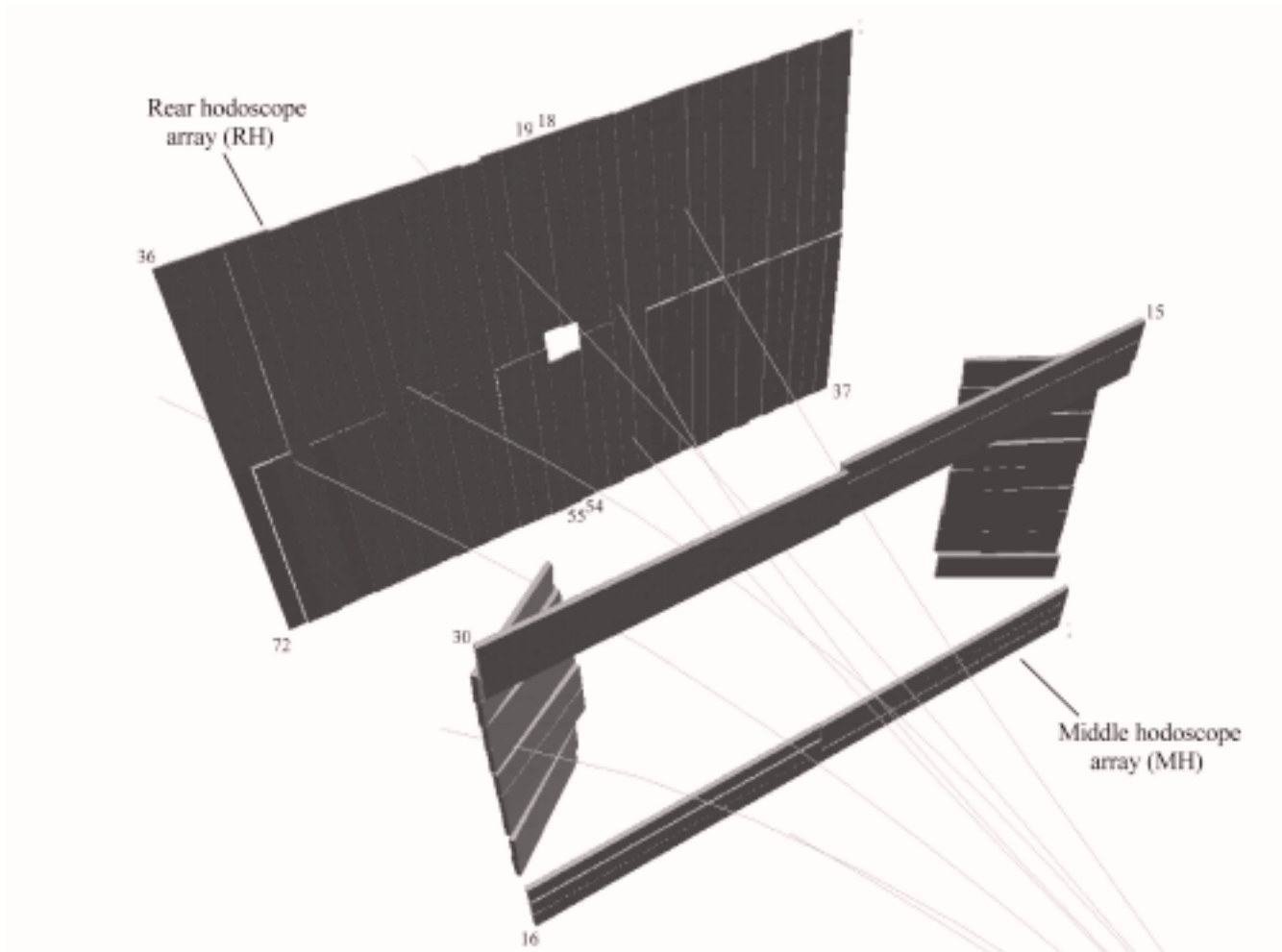


Figure 2.4: Middle and rear hodoscope used for time-of-flight particle identification and for triggering the data acquisition system. The numbers shown indicate the numbering of counters in the array.

2.2.5 Čerenkov Counter

The Čerenkov counter was the most downstream component of the multi-particle spectrometer located about 3 meters from the target. It was made up of 96 toroidal mirrors arranged on two planes forming a 120° wedge facing the target and with each plane making a 30° angle with the vertical. The medium used was Freon 114 ($C_2Cl_2F_4$) with an index of refraction of 1.0015. As shown in Figure 2.5, each mirror reflected Čerenkov radiation emitted by relativistic particles in the medium to a phototube positioned above or below the aperture of the mirror array. Like the middle and rear hodoscopes, the Čerenkov counter was used for particle identification. The π , K , and p momentum thresholds for the Čerenkov counter were 2.5, 9.0, and 17.1 GeV/c respectively.

2.2.6 Drift Chambers

Six drift chambers were used in the multi-particle spectrometer. Chamber 1 was the smallest measuring 30" wide by 18" high and positioned immediately downstream of the target. Chamber 2 measured 36" wide by 24" high. The dimensions of chambers 3, 4, and 5 were 60" wide and 40" high. Chamber 6 was the largest measuring 72" wide and 48" high and positioned right behind the rear hodoscope array. All six chambers were similar in design to the chambers used in the beam spectrometers. Each had four anode planes with wires oriented at angles of -21.6° , -7.93° , 7.93° , and 21.6° with respect to the vertical. The anode planes were sandwiched between five cathode planes and two ground planes with vertical wires. The chambers had windows made of Kapton. A gas mixture of 71% Argon, 25% Isobutane and 4% Methylal was used in all chambers. Each chamber was roughly equivalent to 0.15% radiation length of material. The spaces between the chambers were filled with He to reduce the effects of ionization loss and multiple scattering.

The magnet used in the multi-particle spectrometer was a 240 ton, large aperture dipole known as the Jolly Green Giant. It measured 1.2 m high, 2.5 m wide and 2.2 m deep. This magnet provided

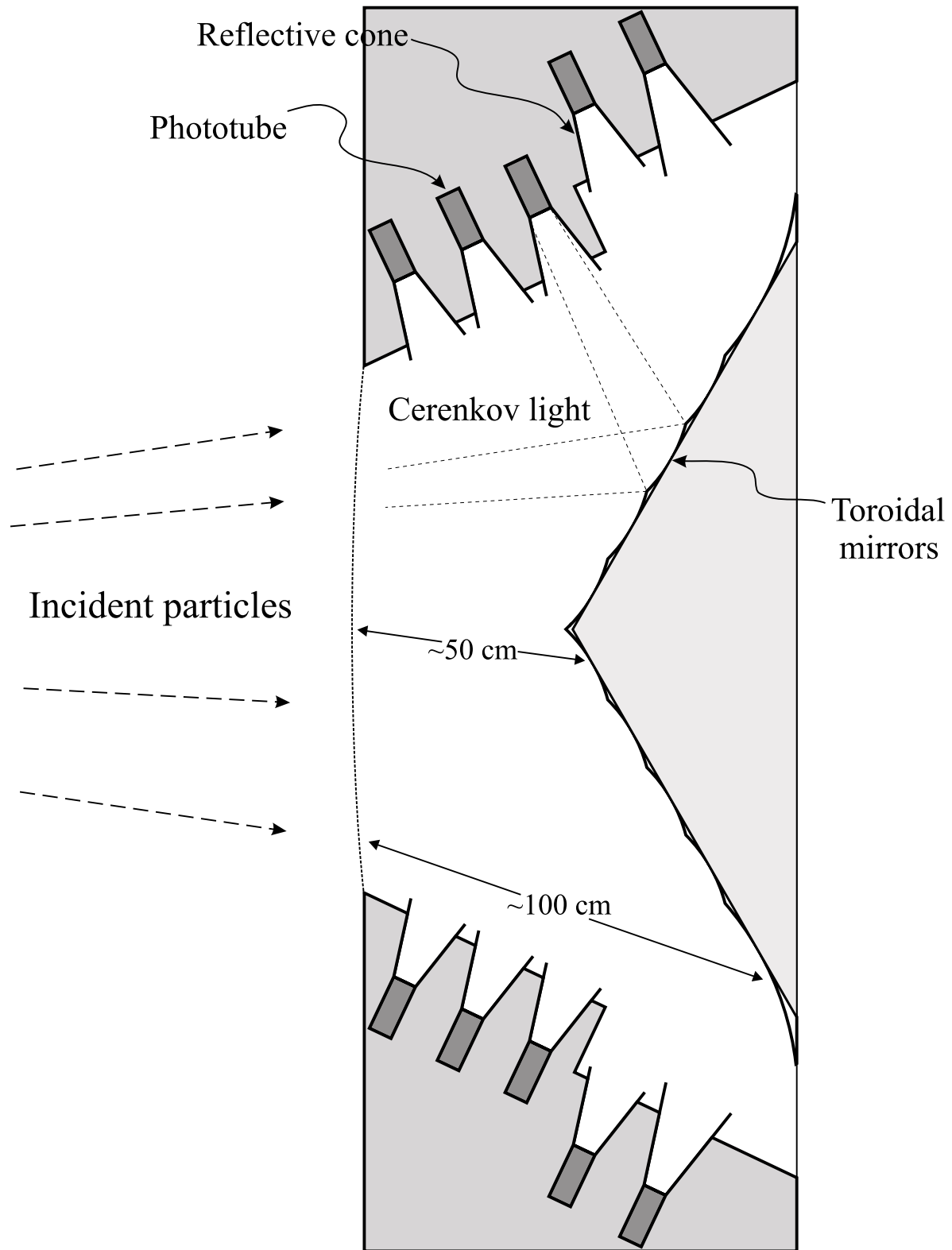


Figure 2.5: Side view of the Čerenkov counter.

2.3. DATA ACQUISITION SYSTEM

an average transverse momentum kick of 350 MeV/c. The magnetic field was mapped using the Fermilab ZIPTRACK [55] system to within ± 1 Gauss.

The drift chamber and magnet combination had a geometric acceptance of ± 580 mrad in the horizontal direction and ± 410 mrad in the vertical direction. It allowed measurement of charged particle trajectories with momenta ranging from 0.15 to 20 GeV/c with a momentum resolution of $\Delta p/p = .002p$ (FWHM). Mass distributions of reconstructed K_S^0 , Λ^0 , and Ξ^- particles fitted to Gaussians have typical widths of $\sigma = 2, 0.7,$ and 1 MeV/c² respectively. Current world averages for the Λ^0 and Σ^0 masses in the particle data book [58] are based on measurements made with this spectrometer [56, 57].

2.2.7 Forward Hodoscope

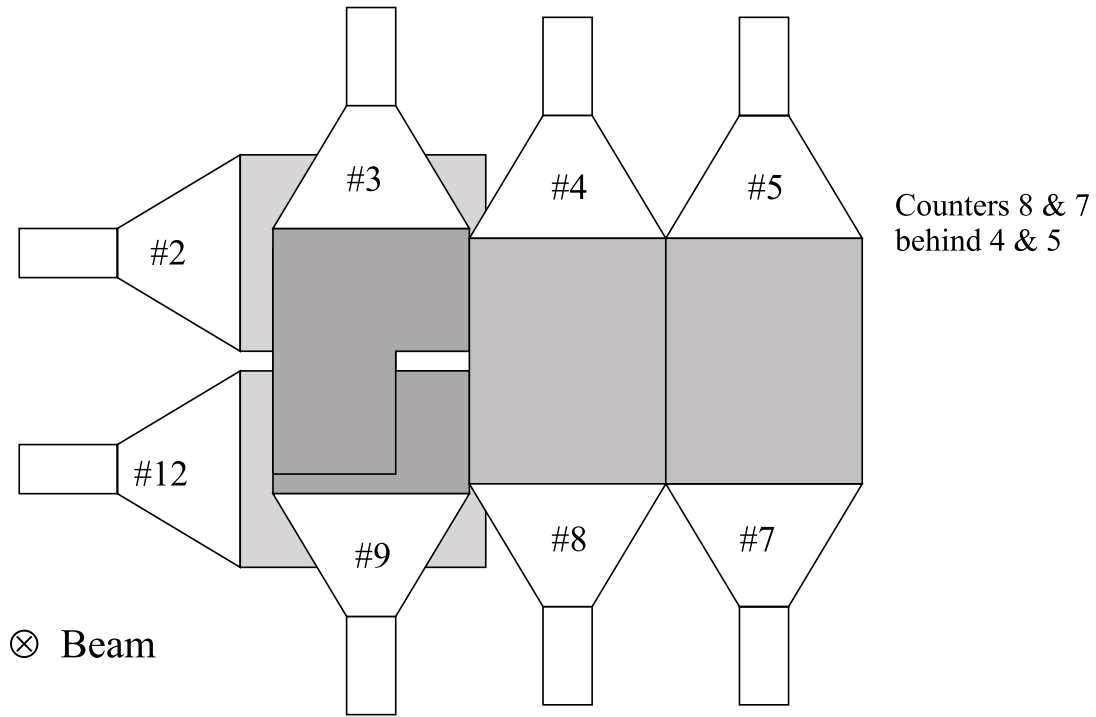
The forward hodoscope was located about 80 meters downstream of the liquid hydrogen target beyond chamber 5 of the forward beam spectrometer. Figure 2.6 shows a diagram of the forward hodoscope which was assembled from eight 4" \times 5" rectangular pieces of scintillation counters. Two of the counters had a 1.5" \times 2.5" rectangular section cut out. The counters were arranged to form a rectangular aperture measuring roughly 1.5" wide and 0.3" high in the path of an uninteracted beam proton. They were configured into two groups of four counters each, with counters 2, 7, 8 and 9 forming *group A* and counters 3, 4, 5, and 12 forming *group B*. A signal from any counter in one group in coincidence with any counter in the other group was taken to signal the presence of an interacted beam proton.

2.3 Data Acquisition System

2.3.1 Overview

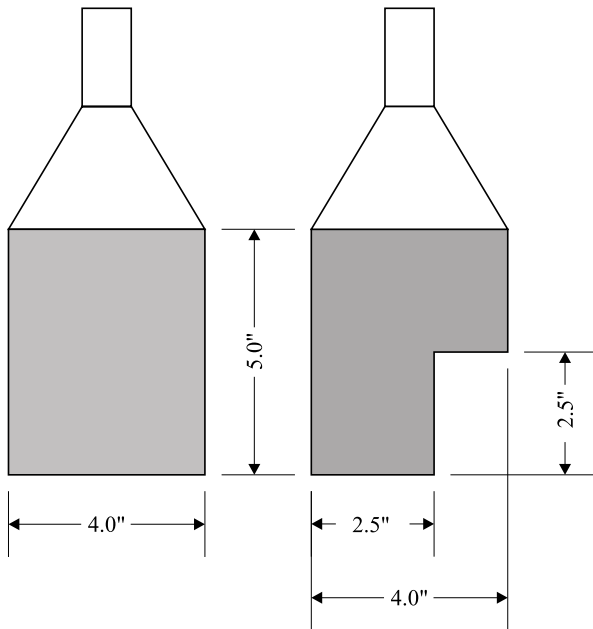
Charged particle tracks produced by the interaction of the beam proton in the liquid hydrogen target induced electrical responses in the active elements of the detector. These electrical signals

CHAPTER 2. EXPERIMENTAL APPARATUS



Counters 2, 4, 5,
7, 8, & 12

Counters 3 & 9



Group A: 2, 7, 8, & 9
Group B: 3, 4, 5, & 12

TG3 requires:
 $(2 + 7 + 8 + 9) \cdot (3 + 4 + 5 + 12)$

Figure 2.6: The forward hodoscope used to detect the presence of a scattered beam proton in the forward spectrometer.

2.3. DATA ACQUISITION SYSTEM

were conditioned by front-end electronics mounted close to the detector before they were sent to the data acquisition system for digitization. Figure 2.7 shows a block diagram of the E690 data acquisition system.

For the drift chambers in the beam and main spectrometers, the front-end electronics consisted of preamplifiers mounted on the chambers and amplifier/discriminators that provided additional signal conditioning. The conditioned signals were sent to TDC's that digitized the drift times from the chambers.

The front-end electronics for the counters consisted of amplifiers and discriminators built into the phototube bases. Each phototube base provided one analog and two digital signals. The analog signals were sent directly to the ADC's in the PHT (Pulse Height and Time) system which digitized the pulse area of the signal. One of the digital signals was sent to PDL (Phototube Discriminator/Latch) boards for additional conditioning before it was sent to the PHT system where TDC's digitized the time of arrival of the pulse. The design of the PHT system is described in detail in Ref. [59].

The data acquisition system made use of a triggering system in order to reduce the interaction rates to a manageable level and to select events that were physically interesting and could be reconstructed. The guiding principles used in the design of the trigger system were to select reconstructable events where:

1. there was a beam proton in the incoming beam spectrometer
2. the beam proton had interacted inelastically in the LH_2 target producing at least one charged track in the multi-particle spectrometer
3. the interacted beam proton was scattered into the outgoing beam spectrometer.

The triggering system can be grouped into two major levels—the Fast Trigger Logic (FTL), and the Multiplicity Logic (MLOG). The purpose of the FTL, itself consisting of three levels, was to make rapid decisions to accept or reject an event using only the information from the counters.

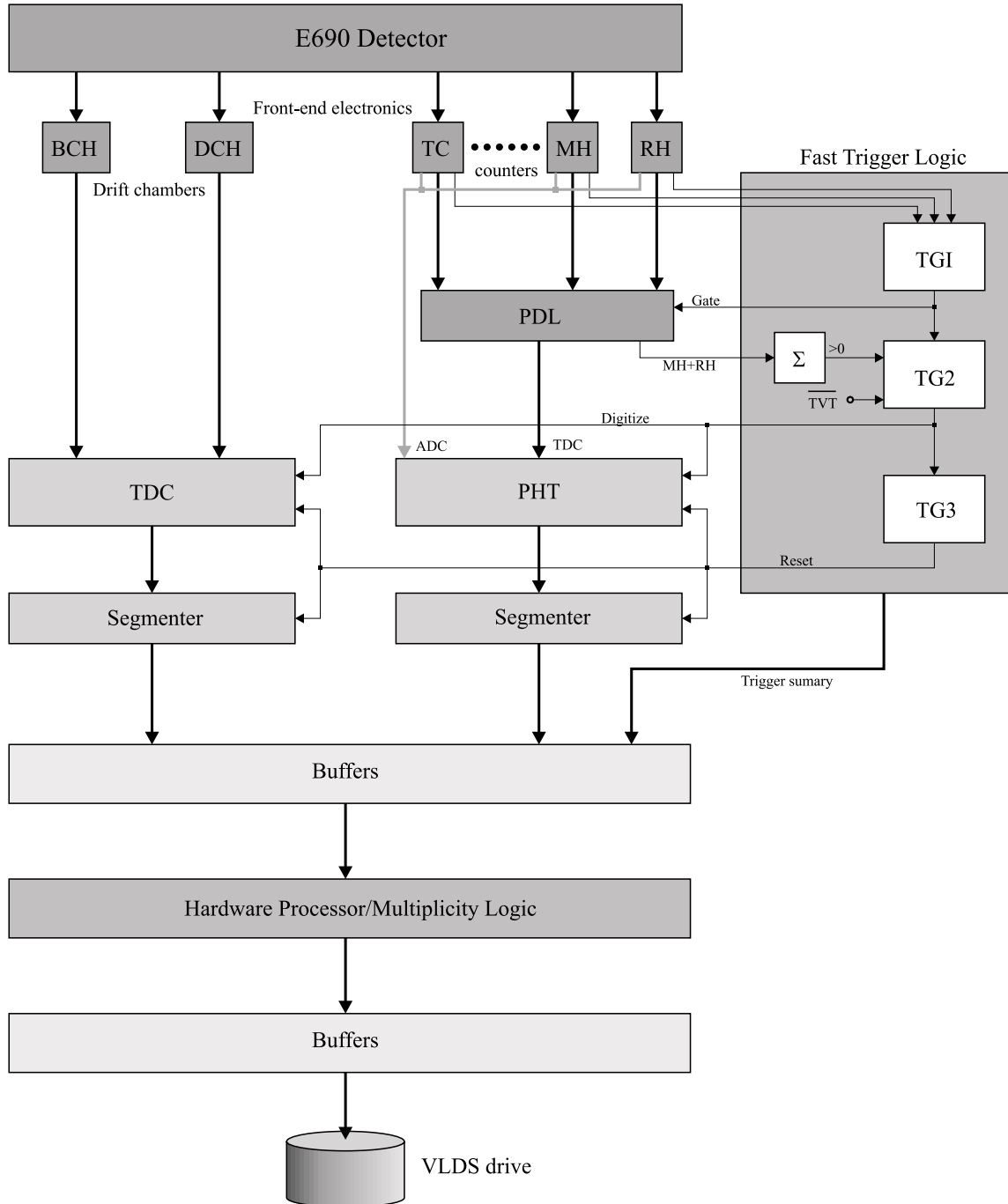


Figure 2.7: Block diagram of the E690 data acquisition system.

2.3. DATA ACQUISITION SYSTEM

Events that passed the FTL conditions were digitized by the TDC and PHT systems and read out by the segmenters. These events were subjected to the next and final level, the Multiplicity Logic, which performed a more sophisticated decision using drift chamber information from the beam and main spectrometers. Up to this point, event information from the various detector components was flowing in separate data streams. For events passing MLOG, all data streams were merged into one and recorded on magnetic tape.

2.3.2 Fast Trigger Logic

Level 1 Trigger (TGI)

The first level trigger in the Fast Trigger Logic was the TGI trigger. Refer to Figure 2.8 for a block diagram of the Fast Trigger Logic. This was also the primary trigger for the data acquisition system.

This trigger required the following conditions to be true:

1. the presence of a signal from the target counter (TC)
2. the presence of a signal from at least one counter from the middle hodoscope and rear hodoscope arrays (Fast OR)
3. the absence of a TGI signal in the last 30 ns
4. the absence of a Master Gate signal.

The signals for the first two conditions were taken from one of the digital outputs of the discriminators built into the bases of the phototubes in the counters. For the second condition, the digital signals from all 102 counters in the middle and rear hodoscope arrays were sent to Fast OR boards that performed a logical OR of all the inputs. The third requirement was enforced by a pulse stretcher within the TGI module that produced a dead time lasting the duration of the stretched pulse.

For the fourth condition, a Master Gate signal was present when any of the following were true:

1. there was no beam

CHAPTER 2. EXPERIMENTAL APPARATUS

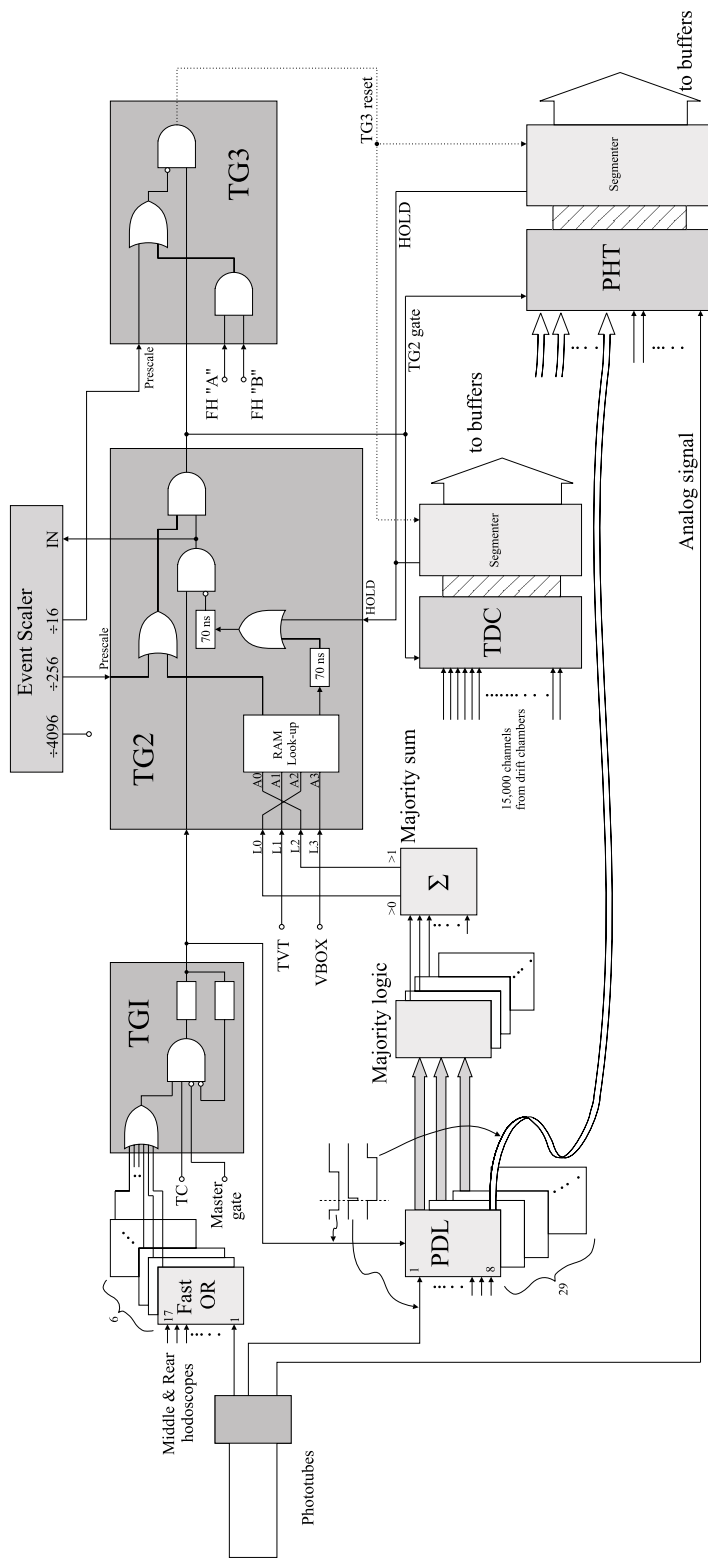


Figure 2.8: Block diagram of the E690 Fast Trigger Logic.

2.3. DATA ACQUISITION SYSTEM

2. a current trip occurred in the drift chamber high voltage
3. beam line magnets were off
4. the manual gate switch was off.

Level 2 Trigger (TG2)

When all the TGI conditions were met, a TGI gate was generated and sent to the PDL boards. The second digital output from the discriminators in the bases of the phototubes in all the counters served as the input to the PDL boards. The PDL boards standardized the signals from the phototubes that arrived within the TGI gate producing an output pulse whose end was fixed relative to the TGI gate. The width of this output pulse was equal to the arrival time of the pulse relative to the TGI gate subtracted from the width of the TGI gate, plus some fixed minimum width. The PDL outputs of the middle and rear hodoscope counters were fed into majority logic boards that counted the number of phototubes with signals. The total count was reported as >0 , >1 , >2 , and >3 output levels on a majority sum board.

The TGI gate was also sent to the second level trigger or TG2. The TG2 module had four logic inputs LI (L0-3) and could be programmed to generate a trigger on any combination of these inputs in coincidence with a TGI gate. This was implemented using a memory lookup table whose address lines were the LI inputs. The contents of each memory location contained the desired logic output state for a given combination of inputs. The LI logic inputs were connected to different combinations of sources during the course of the experiment. In a large portion of the run, these inputs were connected to the >0 and >2 outputs of the majority sum, the output of the Halo counter, and the output of the Veto Box. For most of this portion of the run, the TG2 module was programmed to generate a trigger on a >0 condition from the majority sum and no signal from the Halo counter within the duration of the TGI gate.

CHAPTER 2. EXPERIMENTAL APPARATUS

A self-imposed dead time of about 140 ns was also implemented with pulse stretchers in the TG2 module. This allowed some recovery time for the drift chambers in case there were events that produced many tracks in the main spectrometer but did not meet the TG2 trigger requirements. The TG2 module was also disabled by a HOLD signal generated by the segmenters when they were still busy reading out the previous event.

Thus, a typical TG2 trigger was generated when the following conditions were true:

1. presence of a TGI gate
2. presence of a signal from the > 0 output of the majority sum
3. absence of a signal from the Halo counter
4. absence of a self-imposed dead time in the previous $\simeq 140$ ns
5. absence of a HOLD signal from the segmenters

If all the TG2 conditions were met, the TG2 module generated a signal that initiated digitization in the PHT and TDC systems. After digitization, the events were read out by the segmenter into intermediate buffers.

Level 3 Trigger (TG3)

The signal generated by a successful TG2 trigger was also sent to the third level trigger or TG3. Upon detecting the leading edge of the TG2 trigger, the TG3 module required the following two conditions to be true:

1. presence of a signal from at least one counter in *group A* of the Forward Hodoscope array
2. presence of a signal from at least one counter in *group B* of the Forward Hodoscope array.

If these two conditions were not met, the TG3 module generated a reset pulse which was timed to arrive after the start of digitization in the PHT and TDC systems but before the readout sequence

2.3. DATA ACQUISITION SYSTEM

by the segmenters. This pulse halted the digitization process and discarded the event before it was read out.

When the three triggers described above were met, event readout by the segmenters proceeded without interruption.

2.3.3 Multiplicity Logic

The events read out into the intermediate buffers were subjected to the final level of trigger decisions by the Multiplicity Logic. The MLOG trigger was implemented using a dedicated hardware processor (see Section 3.1) which was also designed to perform online track reconstruction.

The Multiplicity Logic performed a crude pattern recognition by counting the number of clusters in each drift chamber view. A cluster was defined as a set of adjacent wires that produced a signal. The four views were ranked in order of increasing number of clusters as follows: 1 for least populated, 2 for next to least populated, 3 for next to most populated, and 4 for most populated. The trigger required certain chamber views of a selected rank to have cluster counts within a given minimum and maximum.

Table 2.1 shows these requirements as implemented in the Multiplicity Logic for most of the run. The first column specifies three things—a chamber system, a chamber number, and a view within that chamber of a particular cluster count rank. *JGG* indicates the multi-particle spectrometer chamber system, *IBC* indicates the incoming beam chamber system, and *OBC* indicates the outgoing beam chamber system. So the third entry *IBC-123-2* is read as the next to least populated view of chambers 1, 2, and 3 of the incoming beam spectrometer system. The bracketed numbers in the next four columns indicate the required inclusive minimum and maximum cluster counts in the specified view. Thus [3, 4] is read as a cluster count of at least three but not more than four.

An event passes the MLOG trigger if any one of the 4 columns is satisfied. The cluster count requirements for the main spectrometer chambers are consistent with having at least one extra charged track produced by the interaction of the beam proton in the liquid hydrogen target. The

TRG_12				
	1	2	3	4
JGG-2-2	[2,31]	-	[3, 31]	-
JGG-3-2	-	[2,31]	-	[3,31]
IBC-123-2	[3, 4]	[3, 4]	[3, 8]	[3, 8]
IBC-123-3	[4, 5]	[4, 5]	[4, 9]	[4, 9]
OBC-12-1	[1,31]	[1,31]	[2,31]	[2,31]
OBC-12-3	[2,31]	[2,31]	[3,31]	[3,31]
OBC-3-3	[1, 8]	[1, 8]	[3,10]	[3,10]
OBC-45-1	[1, 8]	[1, 8]	[3,10]	[3,10]
OBC-45-3	[2, 8]	[2, 8]	[4,10]	[4,10]

Table 2.1: Multiplicity Logic trigger conditions used for most of the run. These conditions allowed 1 or 2 beam particles but required the same same number in the incoming and outgoing beam spectrometers. See the text for more details on reading this table.

requirements for the beam spectrometers in the first two columns are consistent with having a single incoming and outgoing beam particle. Those for the last two columns are consistent with having two incoming and two outgoing beam particles. Extra counts were allowed to account for noise.

A more restrictive set of conditions used for the multiplicity logic at the beginning of the run is shown in Table 2.2. The cluster count requirements are consistent with having only one beam particle in both the incoming and outgoing beam spectrometers. Unlike TRG_12 which required hit clusters in either chamber 2 or 3 of the multi-particle spectrometer, this set of conditions checked only chamber 3 for hits. A summary of the different trigger conditions used for the entire run is shown in Table 2.3.

2.3.4 Prescale Events

The data acquisition system also employed an event scaler which counted the total number of live TGI triggers. These were the total number of TGI gates which arrived at the TG2 module when it was not busy due to a hold signal generated by the segmenters or due to its self-imposed dead

2.3. DATA ACQUISITION SYSTEM

TRG_DCC	
JGG-3-2	[2,31]
IBC-123-2	[3, 6]
IBC-123-3	[4, 6]
OBC-12-1	[1,31]
OBC-12-2	[2,31]
OBC-12-3	[2,31]
OBC-3-3	[1,31]
OBC-45-1	[1, 8]
OBC-45-2	[2, 8]
OBC-45-3	[2, 8]

Table 2.2: Multiplicity Logic trigger conditions used at the beginning of the run allowing only one beam particle in the incoming and outgoing beam spectrometers.

Geometry Group	Fast Trigger Logic			Multiplicity Logic	Events $\times 10^9$
	TGI	TG2	TG3		
1-3	TC	$GT0 \bullet \overline{TVT}$	-	TRG_DCC	.775
4-5	TC	$GT1 \bullet \overline{TVT}$	-	TRG_12	.72
6	TC	$GT0 \bullet \overline{TVT}$	$FHA \bullet FHB$	TRG_12	.062
7-12	$TC \bullet OR's$	$GT0 \bullet \overline{TVT}$	$FHA \bullet FHB$	TRG_12	2.96
13	$TC \bullet OR's$	$GT0 \bullet \overline{TVT}$	$FHA \bullet FHB$	TRG_12	.54
13 vetoes	$TC \bullet OR's$	$GT0 \bullet \overline{TVT} \bullet \overline{VETO}$	$FHA \bullet FHB$	TRG_12	.36
<i>total</i>					5.417

Table 2.3: Summary of E690 run conditions.

CHAPTER 2. EXPERIMENTAL APPARATUS

time. The scaler had several divided outputs— $\div 16, \dots \div 4096$ —which produced a signal every given number of counts. As shown in Figure 2.8 these divided outputs were sent to the prescale inputs of the TG2 and TG3 modules. Thus an event was accepted after a given number of live TGI gates without any further conditions. Such unbiased events which were not subjected to any of the trigger requirements, save that of TGI, are used for calculating the trigger efficiencies discussed in Chapter 4.

Chapter 3

Event Reconstruction and Selection

The previous chapter discussed the process of signal detection and data acquisition which resulted in a set of recorded measurements representing a high-energy physics event. This process was followed by a sequence of processing steps aimed at putting the recorded data in a meaningful and usable form. The first of these was Pass 1 which searched for tracks and performed a first stage track reconstruction. Then came Pass 2 which attempted to reconstruct the entire event by improving upon Pass 1's results and by reconstructing interaction and decay vertices. Finally, the reconstructed events from Pass 2 were subjected to an event selection process that separated the events into a number of interesting types. This chapter describes these three steps plus an additional selection step for the charm sample used in this thesis.

3.1 First Stage Track Reconstruction (Pass 1)

The first step in event reconstruction was to find and reconstruct the charged particle tracks whose trajectories were recorded as wire hits in the drift chambers. The algorithm used to perform this task was implemented in both software and hardware. The software implementation was a Fortran program called Pass 1. The hardware implementation was a special purpose computer called the

CHAPTER 3. EVENT RECONSTRUCTION AND SELECTION

hardware processor [60–64]. This processor was composed of over a hundred boards that, to some extent, were functionally equivalent to Pass 1’s Fortran subroutines. The hardware processor was designed to serve as an additional trigger level after the Multiplicity Logic trigger described in the previous chapter. Its purpose was to select events that could be fully reconstructed for recording on magnetic tape. In E690, the hardware processor was not implemented as an on-line trigger. It was operated off-line to reconstruct the events recorded on tape that passed the whole sequence of triggers used in the experiment up to the Multiplicity Logic trigger. For the sake of clarity and convenience, we shall take Pass 1 to mean the hardware processor from here on.

The Pass 1 track finding and reconstruction algorithm is discussed in greater detail in References [51, 52]. We shall provide a brief description of the basic idea before embarking on a more detailed discussion of the second phase of event reconstruction by Pass 2. Pass 1 used similar algorithms to find tracks in both the beam spectrometer and the multi-particle spectrometer. To illustrate the basic principle, we will take the simpler case of the beam chamber tracks. Straight line tracks in both the incoming and forward spectrometers were found using only three chambers. In the case of the forward spectrometer, these were the last three chambers where there was no magnetic field. Recall from the Section 2.2.6 that all drift chambers used in the E690 detector had four anode planes forming different angles with the vertical. The reconstruction procedure was initiated by taking all combinations of wire hits in a given wire plane view of the first and third chambers to form a straight line (see Figure 3.1). The intersection of this straight line with the plane of the same view in the second drift chamber was used to predict a wire hit in that plane. A candidate track was found if a measured hit existed within a given distance of the prediction. The two-dimensional track found in this plane was then paired with a track in another wire plane view to form a three dimensional representation of the track. This three dimensional track was then used to predict the wire hits in the other two wire plane views. If no more than one hit was missing from the other pair, the algorithm proceeded to the fitting stage where an iterative least squares fit was performed on the track. Tracks were parametrized with their x and y coordinates in the first and third chambers.

3.1. FIRST STAGE TRACK RECONSTRUCTION (PASS 1)

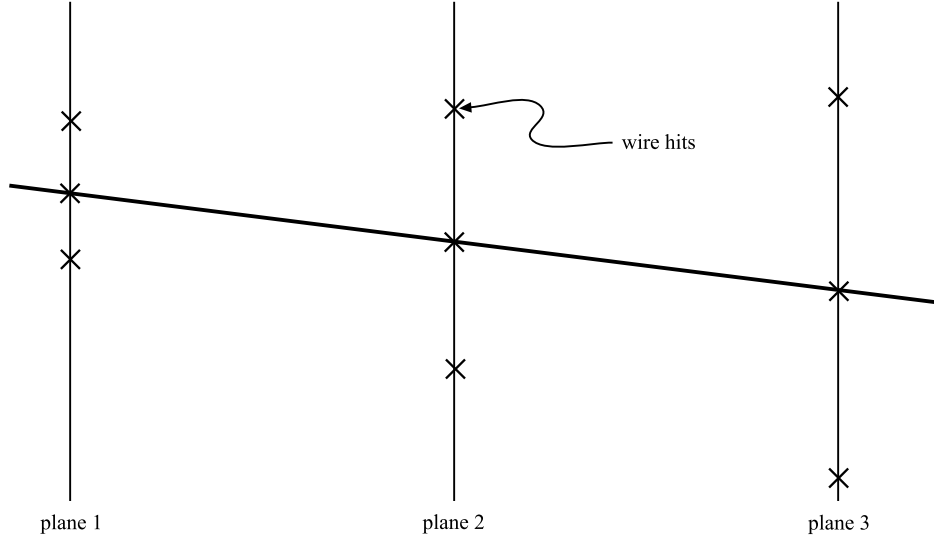


Figure 3.1: 3-plane line finder used in Pass 1 for reconstructing beam chamber tracks.

Those passing the fit were then checked for duplicates by comparing their parameters. If duplicates were found, the tracks with a poorer fit quality were dropped.

The procedure used to find and reconstruct curved tracks in the multi-particle spectrometer proceeded in a similar fashion. The main difference was that more chambers were used to search for three types of tracks shown in Figure 3.2. These were 6 chamber tracks that went through all chambers, front 4 chamber tracks that went through chambers 1-4 and back 4 chamber tracks that went through chambers 3-6. The tracks were also described using a new set of 5 parameters, x_0 , y_0 , dx/dz , dy/dz and the sagitta. x_0 and y_0 are the intercepts with an intermediate chamber of a straight line passing through the end points of the track. dx/dz and dy/dz are the slopes of the straight line. The sagitta represents the curvature of the track by measuring its deviation from the straight line. This curvature was also used to pair the tracks in the matching stage. Unlike the beam chamber algorithm, drift time information, which measured the distance from a track to the closest wire, was also used for reconstructing multi-particle spectrometer tracks.

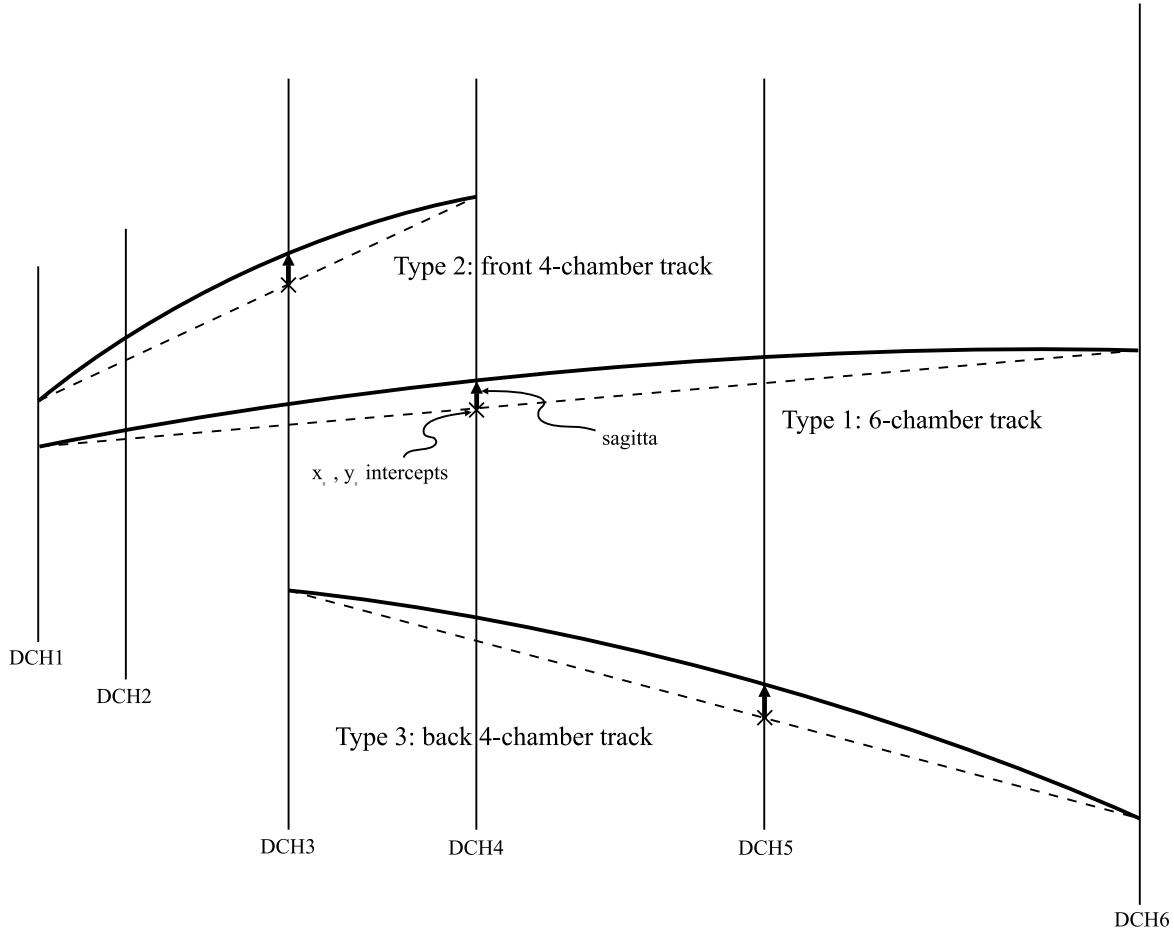


Figure 3.2: Multi-particle spectrometer track types reconstructed by Pass 1.

3.2 Track and Vertex Reconstruction (Pass 2)

3.2.1 Beam Track Reconstruction

Pass 1 found beam tracks separately in the incoming (IBC) and outgoing (OBC) beam chamber systems. The Pass 2 event reconstruction process began by trying to match these separately found beam tracks into interacted and uninteracted pairs. First, it tried to find the uninteracted pairs. This was done by predicting the position of an IBC track at the third and fifth chambers of the OBC system under the assumption the IBC track did not interact in the target. If the predicted positions were close enough to the positions of a reconstructed OBC track, the two were matched as

3.2. TRACK AND VERTEX RECONSTRUCTION (PASS 2)

an uninteracted pair. Then it checked for duplicate tracks separately in the IBC and OBC systems. Two tracks whose positions at the third chamber of either system were close enough were considered duplicates. An exception was made if they were matched to different tracks in the other beam chamber system by the previous step. For duplicates, the track having more planes with missing hits or having a poorer fit was dropped. If more than one track remained after this first duplicate removal attempt, tracks with too many shared hits were considered duplicates and the same criteria applied to decide which one to drop.

After removing duplicates, a check was made to see if any uninteracted tracks in the OBC were missed. This was done by assuming that an IBC track did not interact in the target. With this assumption, the positions of the track in all 20 wire planes (4 planes \times 5 chambers) of the OBC system were predicted. If these predictions came within a certain limit of actual wire hits for more than 17 planes, then a new uninteracted OBC track was found. The hits were assigned to the new track and the duplicate check was repeated. This process of finding missed OBC tracks was repeated as long as there were more IBC tracks than OBC tracks. Finally, remaining tracks were matched as interacted pairs. Then an iterative fit was performed on both interacted and uninteracted pairs. For the interacted tracks, the momentum lost by the incident beam track was also calculated.

3.2.2 Reconstruction of Multi-Particle Spectrometer Tracks

Once the beam tracks were reconstructed, Pass 2 checked to see which wire hits in the drift chambers of the multi-particle spectrometer could be assigned to the beam tracks. Then it reparametrized the multi-particle spectrometer tracks found by Pass 1 to the new set— x , y , dx/dz , dy/dz , and Q/p_z at the z -position of drift chamber 3. The first two parameters are the track coordinates at chamber 3. The next pair are the slopes and Q/p_z is the charge of the track divided by the z -component of its momentum. Using this new set of parameters, wire hits were reassigned to the tracks. Tracks that had fewer than 7 wire hits uniquely assigned to them in the last 3 drift chambers were removed from the track list.

CHAPTER 3. EVENT RECONSTRUCTION AND SELECTION

Pass 2 then performed a least squares fit of the reparameterized tracks involving 3 separate phases. Initially, the fit was done using only the originally assigned wire hits. After a certain number of iterations or if the the parameter Q/p_z ceased to change by more than some amount from the previous iteration, it proceeded to the next two phases. In the second phase, the original wire hits assigned to the track were replaced with other hits in an attempt to improve the fit. Finally, in the third phase, drift time information from the chambers was incorporated into the fitting procedure. In the process, Pass 2 also checked to see if it could extend short tracks that did not go through all six chambers to the adjacent chambers.

3.2.3 Primary Vertex Reconstruction

After refitting the tracks found by the processor and removing duplicates, the very first step in vertex reconstruction was to locate the primary interaction point. This was the primary vertex and was normally the point in the liquid hydrogen target where the incident beam proton interacted to produce additional particles in the spectrometer. Pass 2 began this search by going through the list of reconstructed tracks in the multi-particle spectrometer to find the first track whose transverse distance from the beam track at the point of closest approach was within a given limit. This point of closest approach or crossing point was the position along the z -axis where the transverse distance between the two tracks was a minimum. This search was done using only tracks that went through the first drift chamber, and whose reconstructed trajectories projected back to the z -plane of the target. Using this crossing point as an initial guess of the primary vertex's position, the transverse distance squared of all other tracks from the beam track were calculated at this z -plane. If they were within a certain limit, they were assigned to this primary vertex candidate. This procedure of assigning tracks was iterated a number of times and the z -position of the crossing point was varied to minimize the squared transverse distances from the beam track. At each succeeding iteration, attempts were made to assign tracks which had previously failed. Among tracks which had previously succeeded, only the worst of those which failed was dropped at each iteration.

3.2. TRACK AND VERTEX RECONSTRUCTION (PASS 2)

The entire procedure was repeated with the remaining unassigned tracks to see if other candidates for the primary vertex could be found. A new candidate replaced the existing one if it had more tracks assigned to it. If both candidates had the same number of tracks, the one with a smaller average squared distance of closest approach was kept. If this average was similar, the one with a wider opening angle was chosen. After going through all the unassigned tracks, Pass 2 proceeded to the next stage with the best candidate for the primary vertex. In this next stage, all the tracks assigned to the best candidate were simultaneously refit with the requirement that they originated from the vertex. If the number of tracks assigned to the primary vertex was greater than 3, the coordinates of the vertex were allowed to vary during the fit. Otherwise, the vertex was constrained to the x and y coordinates of the beam track. In the case of the free primary vertex, the number of parameters in the fit were three for the coordinates of the primary and three each for Q/p_z and the slopes dx/dz , dy/dz of each reconstructed track at drift chamber 3. If composites decaying into secondary vertices (see next section) were included, this added one extra parameter for the z -distance of each additional vertex from its parent. The x and y coordinates of the additional vertices were not free since the composites were required to originate from their parents. In the case where the primary vertex was constrained to the beam track, the number of parameters would be two less than for the free primary. If this fit failed, the track with the greatest transverse distance from the primary was dropped and the fitting procedure repeated. If the fit succeeded, tracks whose mean square errors increased after the fit were dropped from the primary vertex and the whole procedure repeated with the remaining tracks. The improved position of the primary vertex resulting from this stage was used as a constraint to which the remaining unassigned tracks were individually refit. Those which passed this constrained fit were folded into the primary.

3.2.4 Secondary Vertex Reconstruction

Pass 2 then proceeded to the next phase where it searched for secondary vertices using the unassigned tracks which could not be folded into the primary. Just as in the primary vertex phase, it started

CHAPTER 3. EVENT RECONSTRUCTION AND SELECTION

Vertex Type	Search Phase	Vertex Location	Mass (GeV/c ²)	Range (GeV/c ²)
$K_S^0 \rightarrow \pi\pi$	1st Pass	$ZP < 6$	0.4977	± 0.005
		$6 \leq ZP < 9$		± 0.006
		$ZP \geq 9$		± 0.01
	2nd Pass	$ZP < 6$		± 0.008
		$6 \leq ZP < 9$		± 0.009
		$ZP \geq 9$		± 0.012
$\Lambda \rightarrow p\pi$	1st Pass	$ZP < 6$	1.1156	± 0.005
		$6 \leq ZP < 9$		± 0.002
		$ZP \geq 9$		± 0.003
	2nd Pass	$ZP < 6$		± 0.005
		$6 \leq ZP < 9$		± 0.004
		$ZP \geq 9$		± 0.004
$\Xi \rightarrow (\Lambda \rightarrow p\pi)\pi$			1.3214	± 0.007
$\Omega \rightarrow (\Lambda \rightarrow p\pi)K$			1.6724	± 0.008
$K \rightarrow \pi\pi\pi$			0.4937	± 0.01

Table 3.1: Mass limits used for identifying secondary vertex types in Pass 2. ZP in the 3rd column refers to the z -planes used in Pass 2. z -plane 6 is located at drift chamber 1 while z -plane 9 is located between drift chambers 2 and 3.

the search for secondaries by looking for the crossing point between two tracks. Initially, this was done using only oppositely charged pairs of unassigned tracks. The search range was limited to a region downstream of the primary vertex and upstream of the first drift chamber. If an acceptable crossing point was found between the pair, it calculated the invariant mass of the pair by assigning masses to each track such as two pion masses for possible K_S^0 's and a pion and proton mass for possible Λ^0 's. Before it did this, it checked to see if the transverse momenta of the tracks relative to the pair's momentum vector were not greater than the allowable maximum. This maximum was the magnitude of the momentum for two body decay in the rest frame of the presumed parent particle. The vertex was assigned the particle types shown in Table 3.1 if the calculated invariant mass was within the limits for that particle type shown in the same table. If the transverse momenta of the two tracks were smaller than a certain limit, it was typed as a *small opening angle* or $\gamma \rightarrow e^+e^-$ pair.

3.2. TRACK AND VERTEX RECONSTRUCTION (PASS 2)

The Ξ , Ω , and K hypotheses were tried in later stages after Λ^0 's had been found or additional tracks had been assigned and the search no longer limited to oppositely charged pairs. Some secondary vertices could not be uniquely identified on the basis of the calculated invariant mass. Such vertices were termed *ambiguous* types. Other vertices could not be assigned any particle type and were termed *type 0* or *interaction* vertices just like the primary vertex.

If the secondary vertex could be assigned a particle type, Pass 2 performed a global refit of the vertex's assigned tracks and position similar to the procedure for the primary vertex. In this fit, the composite track decaying into the secondary was required to originate from the primary. If the secondary vertex was a type 0, Pass 2 attempted to assign other unassigned tracks to the secondary vertex. If less than 4 tracks were assigned to the secondary after this step, it repeated the vertex typing process described above. If 4 or more tracks were assigned, the primary vertex was compared with this secondary vertex. The primary was replaced with this secondary if it had fewer tracks assigned to it than the secondary. If the primary had more assigned tracks, Pass 2 attempted to fold this secondary into the primary if it was close enough. The primary was refit if it was replaced or updated. Remaining type 0 vertices with less than 4 tracks that could not be assigned particle types were dropped.

After this first pass of the secondary vertex search, Pass 2 attempted to find new tracks that were missed by Pass 1's initial reconstruction. Then it proceeded to the second pass of the secondary vertex search. Before doing so, it dropped all type 0 secondaries and other secondaries that were upstream of the primary. The second pass was similar to the first except that a looser set of requirements was used. For instance, the z -range used for the search was widened, the composite track was not constrained to originate from the primary in the refit, and no attempt was made to assign a vertex type before the refit. The mass limits used in assigning vertex types were also loosened. Eventually, even tracks assigned to the primary vertex were paired with remaining unassigned tracks in the search for secondary vertices.

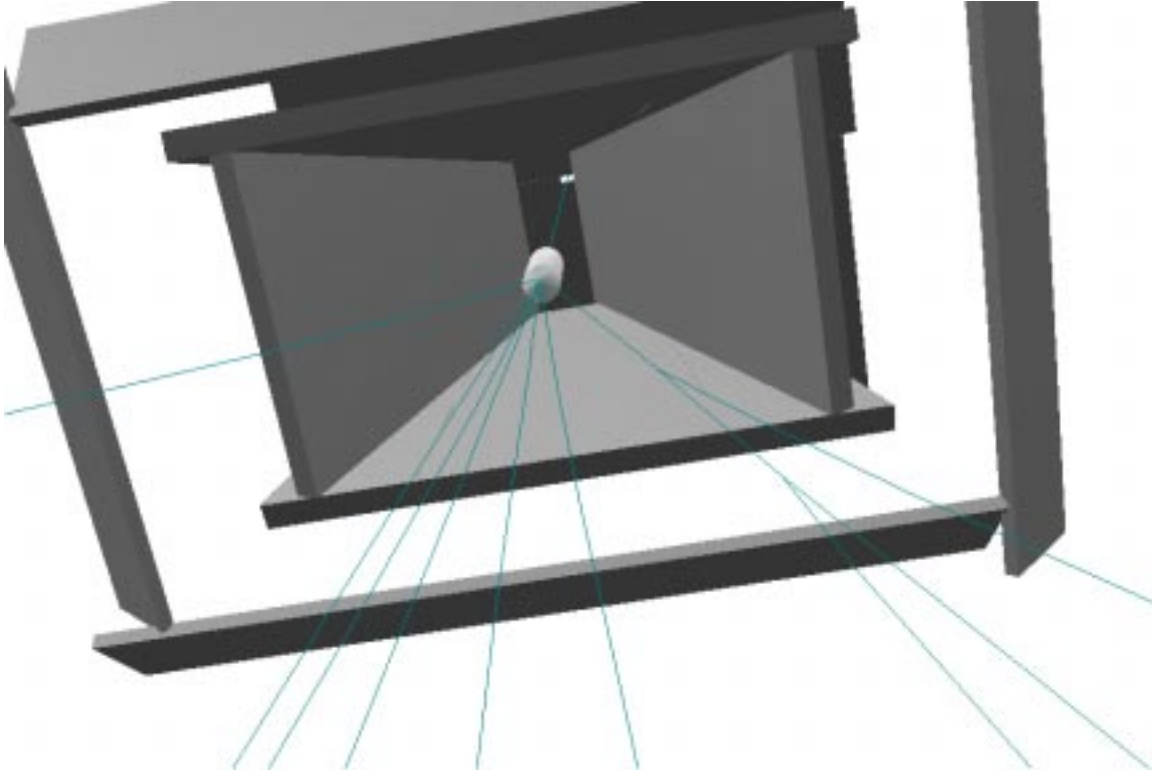


Figure 3.3: Event reconstructed by Pass 2 with two secondary vertices from a possible decay of the type $\Xi^+ \rightarrow (\bar{\Lambda}^0 \rightarrow \bar{p}\pi^+)\pi^+$.

After completing the second pass of the search for secondary vertices, Pass 2 dropped all remaining unassigned tracks with fewer than 7 unique wire assignments in the last three drift chambers. If unassigned tracks remained after this clean-up step, it attempted a constrained fit of these tracks to the primary vertex position. If there were still unassigned tracks after this stage, Pass 2 made one last attempt to search for secondary vertices using these tracks before quitting.

There were times when Pass 2 found no suitable candidates for the primary vertex. In this case, it would look for secondary vertices first and use the composites formed by the secondaries to find a crossing with the beam track for locating the primary. In fact, even before beginning the search for the primary vertex, Pass 2 checked to see if there were exactly two reconstructed tracks in the multi-particle spectrometer. If so, it used these two tracks to find a secondary vertex whose composite track might be used to locate the primary.

3.2. TRACK AND VERTEX RECONSTRUCTION (PASS 2)

Identifier Bit	Type
0 (1)	V^0 events
1 (2)	events with Čerenkov identified tracks
2 (4)	Type I exclusive candidates
3 (8)	Type II exclusive candidates
4 (16)	$pp \rightarrow p(\phi\phi)p$ events
5 (32)	$pp \rightarrow p(\pi^+\pi^-)p$ events
6 (64)	prescale events

Table 3.2: Event types selected in Pass 2’s select output.

3.2.5 Pass 2 Output

The Pass 2 program wrote data out in two separate streams—a *One-to-One* output and a *Select* output. As the name implies, all input events were written out in the One-to-One sample. Only a subset of all input events were written out in the Select output. These were events of the types indicated in Table 3.2. V^0 events are those with at least one typed secondary vertex. The events with Čerenkov identified tracks in the second entry of the table are those having at least one track whose Čerenkov information was consistent with being neither an electron nor a pion. Exclusive candidates are events that might be fully reconstructed. Events with a total charge of $Q = +1$, missing longitudinal momentum $\Delta p_z \leq 5$ GeV/c and missing transverse momentum squared $\Delta p_T^2 \leq 0.02$ (GeV/c)² qualified as exclusive candidates. For Type I exclusive candidates, the quantities Q , Δp_z , and Δp_T^2 were calculated using only tracks assigned to the primary vertex. For Type II exclusive candidates, unassigned tracks were also included in the calculation of these quantities. $pp \rightarrow p(\phi\phi)p$ represents double pomeron exchange candidates in which the two centrally produced ϕ ’s each decayed into a pair of oppositely charged K ’s. $pp \rightarrow p(\pi^+\pi^-)p$ represents the double pomeron exchange candidates selected for the analysis described in Ref. [52].

Strip Output Stream	Type
1	V^0 events
2	$pp \rightarrow p(\pi^+\pi^-)p$ events
3	D^0/D events
4	D^* events
5	$D^*(bkg)$ events
6	meson events
7	exclusive events

Table 3.3: Output streams produced by the Strip Job.

3.3 Strip Job

Although events in the Pass 2 Select output were tagged according to the types listed in Table 3.2, they were all written to the same tape. This third step which will be referred to as the Strip Job sorted these different types of events and wrote them onto separate output tapes. In addition to the types identified in the Pass 2 select output, a number of new types were included for a total of 7 separate output streams. A list of all seven event types is shown in Table 3.3. The new types were written to a meson stream and three charm D meson streams. The meson stream included the original $pp \rightarrow p(\phi\phi)p$ candidates identified in the Pass 2 select output and a number of new meson final state candidates such as $pp \rightarrow p(K^+K^-)p$ and $pp \rightarrow p(K_S^0K_S^0)p$. The criteria used for selecting events in the D meson streams is shown in Table 3.4. The $D^*(bkg)$ stream was meant for background studies of D^* candidate events. The criteria used in this stream were identical to that for D^* 's except that the K and one of the π tracks were required to have incorrect charges opposite those of the D^* candidates.

3.4 D^* Candidates Selection

Since the cross section measurement in this thesis is made using the D^* sample, we list the D^* selection criteria used in the Strip Job separately and in more detail in Table 3.5 . These D^*

3.4. D^* CANDIDATES SELECTION

	Charm Decay Mode	Selection Criteria
D^0/D	$D^0 \rightarrow K^- \pi^+$ $\bar{D}^0 \rightarrow K^+ \pi^-$	$M(D^0) = 1.865 \pm 0.2 \text{ GeV}/c^2$ and Čerenkov identified K
	$D^+ \rightarrow \bar{K}^0 \pi^+$ $D^- \rightarrow K^0 \pi^-$	$M(D) = 1.869 \pm 0.2 \text{ GeV}/c^2$
	$D^0 \rightarrow \bar{K}^0 \pi^+ \pi^-$ $\bar{D}^0 \rightarrow K^0 \pi^- \pi^+$	$M(D^0) = 1.865 \pm 0.2 \text{ GeV}/c^2$
	$D^+ \rightarrow K^- \pi^+ \pi^+$ $D^- \rightarrow K^+ \pi^- \pi^-$	$M(D) = 1.869 \pm 0.2 \text{ GeV}/c^2$ and Čerenkov identified K
	D^*	$D^{*+} \rightarrow K^- \pi^+ \pi^+$ $D^{*-} \rightarrow K^+ \pi^- \pi^-$
$D^*(bkg)$	$D^{*+}(bkg) \rightarrow K^+ \pi^- \pi^+$ $D^{*-}(bkg) \rightarrow K^- \pi^+ \pi^-$	$M(D^*) = 2.010 \pm 0.2 \text{ GeV}/c^2$ and Čerenkov identified K

Table 3.4: Selection criteria for charm meson strip.

	Selection Criteria
D^* Strip	<ul style="list-style-type: none"> (a) $NTB > 0$: at least one reconstructed beam track (b) $NT > 0$: at least one reconstructed multi-spectrometer track (c) $NV > 0$: at least one reconstructed vertex (d) at least 3 tracks assigned to primary vertex with correct charges to form a $K^\mp \pi^\pm \pi^\pm$ invariant mass combination (e) Čerenkov id on track assigned K mass in forming $K\pi\pi$ mass combination (f) invariant mass $M(K\pi\pi)$ within $\pm 200 \text{ MeV}/c^2$ of $2.010 \text{ GeV}/c^2$
D^* Ntuple	<ul style="list-style-type: none"> (a) $\Delta p_z = p_{z_i}^{beam} - p_{z_f}^{beam} \geq 0$ where Δp_z is the missing longitudinal momentum of the event, $p_{z_i}^{beam}$ is the momentum of the incident beam proton and $p_{z_f}^{beam}$ is the momentum of the scattered beam proton (b) $0 < Q < 11.66 \text{ MeV}/c^2$ where $Q = M(K\pi\pi) - M(K\pi) - M(\pi)$

Table 3.5: Selection criteria for D^* candidates.

Group	Pass2 Select	D^* Strip	D^{*+} Ntuple	D^{*-} Ntuple
1	51443041	7802474	28351	32404
3	20267198	3037972	10006	12433
4	49337079	7761515	26230	31624
5	31911022	5057440	17014	20170
7	68743780	11683644	37908	45631
8	42025057	7061250	22396	26695
9	106792854	17506525	55072	65848
10	68634517	11175481	34830	40799
12	140632220	23877890	76035	93180
13	58396476	9847727	31940	39228
Total	638183244	104811918	339782	408012

Table 3.6: D^* Candidates selection summaries

candidates from the Strip Job were subjected to a second set of criteria shown in the same table to select events that were written to an Ntuple [65]. We will refer to this second D^* sample as the D^* Ntuple sample. Each entry in this Ntuple corresponded to a mass combination so there were more entries than events. A summary of the number of surviving events at each stage of the D^* selection process is shown in Table 3.6.

Using the D^* Ntuple sample two separate sets of cuts were applied to plot histograms of the $K\pi\pi$ and $K\pi$ invariant masses for the D^{*+} and D^{*-} samples. For the D^{*+} , the following cuts were used:

- Čerenkov identification on the π^+ from the D^0 decay
- a tighter Q cut $\Rightarrow |Q - 5.83| < 0.5 \text{ MeV}/c^2$
- time-of-flight identification on the slow π^+ coming directly from the D^{*+} decay, where the measured flight time was required to be within 3σ of the expected time for a π and the pion momentum was required to be $< 1.0 \text{ GeV}/c$ for good π/p separation.

3.4. D^* CANDIDATES SELECTION

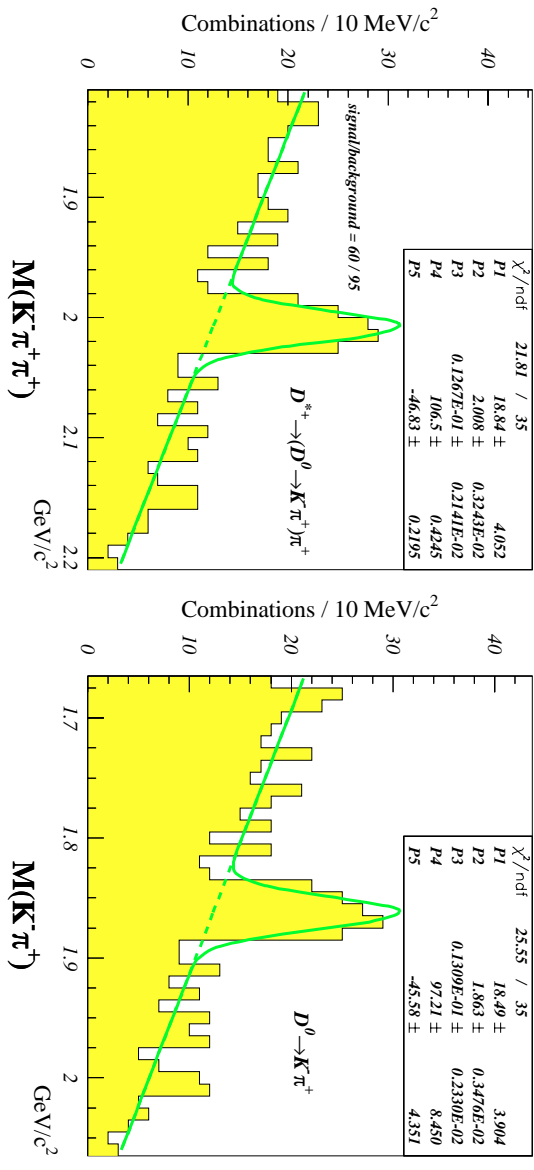


Figure 3.4: Invariant mass plots of the D^{*+} and D^0

Plotting only those entries satisfying the cuts enumerated above resulted in 575 entries between 1.810 and 2.210 GeV/c^2 for the $K^-\pi^+\pi^+$ invariant mass and 574 entries between 1.665 and 2.065 GeV/c^2 for the $K^-\pi^+$ invariant mass as shown in Figure 3.4.

The same set of cuts above was also used for the D^{*-} except for the time-of-flight requirement on the slow pion since, in this case, the background was due mostly to other pions instead of protons

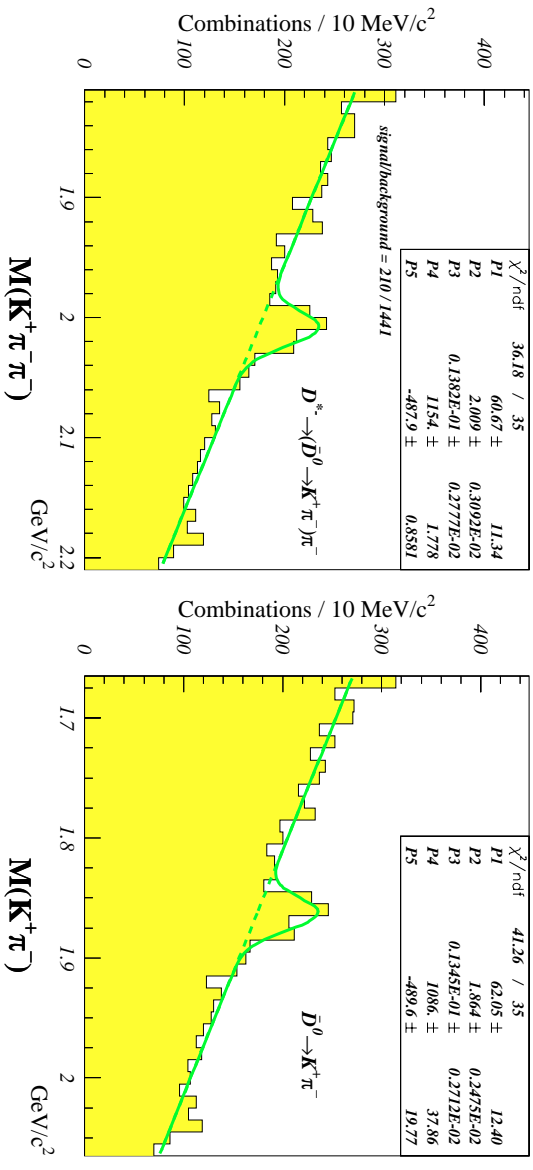


Figure 3.5: Invariant mass plots for the D^{*-} and D^0

CHAPTER 3. EVENT RECONSTRUCTION AND SELECTION

as was true in the case of the D^{*+} . This resulted in 7,186 entries between 1.810 and 2.210 GeV/c^2 for the $K^+\pi^-\pi^-$ invariant mass and 7,173 entries between 1.665 and 2.065 GeV/c^2 for the $K^+\pi^-$ invariant mass as shown in Figure 3.5.

Fitting these distributions to a Gaussian plus a linear background resulted in an estimate of 60 events in the signal over a background of 95 for the D^{*+} and 210 events in the signal over a background of 1,441 for the D^{*-} .

Chapter 4

Cross Section Measurement

The total cross section σ for a reaction between a beam of incident particles and a target of scattering centers is defined as:

$$\sigma = \frac{\# \text{ interactions/sec.}}{(\# \text{ incident particles/sec.}) (\# \text{ scattering centers/unit area})} \quad (4.1)$$

Based on this general definition, the total single diffractive charm cross section can be written as:

$$\sigma_{\text{diff}}(c\bar{c}) = \frac{A}{N_A \rho l} \frac{N_{\text{diff}}(c\bar{c})}{N_{\text{beam}}} \quad (4.2)$$

where:

$$\frac{N_A \rho l}{A} \equiv \frac{\text{Avogadro's number} \times \text{target density} \times \text{target thickness}}{\text{Atomic weight}} \quad (4.3)$$

= number of scattering centers per unit area

N_{beam} = number of beam particles during the live time of the experiment

$N_{\text{diff}}(c\bar{c})$ = number of single diffractive charm events during the
live time of the experiment

CHAPTER 4. CROSS SECTION MEASUREMENT

The two unknown quantities determined here are $N_{\text{diff}}(c\bar{c})$ and N_{beam} . To determine $N_{\text{diff}}(c\bar{c})$, charm events are identified by looking for D^* mesons decaying into a $D^0(K\pi)$ and a π . This decay channel was selected for its attributes in rejecting background events. The D^0 and the π are produced practically at rest in the D^* center of mass resulting in a very low Q value¹ with a very narrow width that is $< 1.0 \text{ MeV}/c^2$ (FWHM).

To minimize systematic effects such as those due to changes and variations in trigger efficiencies, the total number of beam particles, N_{beam} , is determined with respect to a reference process that has a similar dependence on such variations as the $D^* \rightarrow (D^0 \rightarrow K\pi)\pi$ events being measured. For this reference process, we choose events consisting of a Ξ^- decaying into a $\Lambda^0(p\pi)$ and a π . In effect, we are calculating a ratio, $N_{\text{diff}}^{\text{obs}}(D^*)/N^{\text{obs}}(\Xi^-)$, which is proportional to the total single diffractive charm cross section, $\sigma_{\text{diff}}(c\bar{c})$, and is insensitive to the systematic variations mentioned above.

The determination of $N_{\text{diff}}(c\bar{c})$ and N_{beam} are discussed in more detail in the following two sections.

4.1 Determination of N_{beam}

In calculating the total single diffractive charm cross in equation 4.2, the total number of beam particles is normalized to the number of reconstructed $\Xi^- \rightarrow (\Lambda^0 \rightarrow p\pi^-)\pi^-$ events according to:

$$\frac{1}{C} \times N_{\text{beam}} = N^{\text{obs}}(\Xi^-) \quad (4.4)$$

where C is the normalization constant that needs to be determined. This constant can be written as:

$$C^{-1} = \varepsilon_{tgi} \times \varepsilon_{tg2} \varepsilon_{tg3} \varepsilon_{mlog} \varepsilon_{B\Delta p_z} \times \frac{N^{\text{obs}}(\Xi^-)}{N_{B\Delta p_z}} \quad (4.5)$$

¹ $Q = M(D^*) - M(D^0) - M(\pi) = 5.83 \text{ MeV}/c^2$ using values of the D^* , D^0 , and π masses from Ref. [58].

4.1. DETERMINATION OF N_{BEAM}

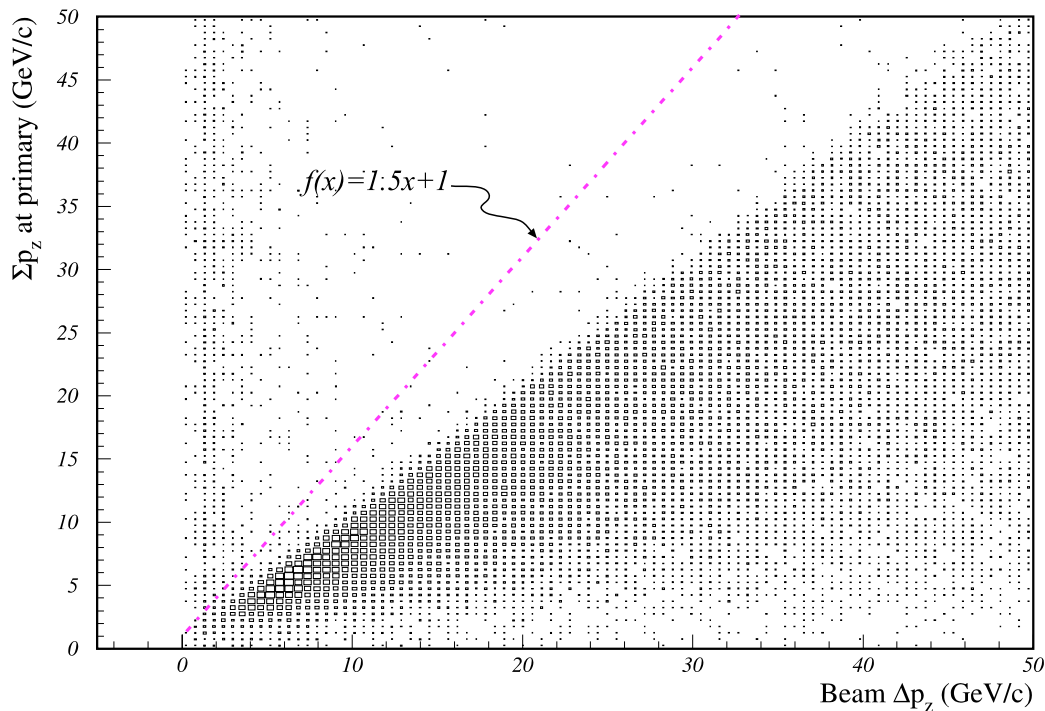


Figure 4.1: p_z sum of all reconstructed tracks assigned to the primary vertex versus Δp_z of the beam proton. Box sizes in the plot are proportional to the density of points.

$$= \frac{N_{tgi}}{N_{tc}} \times \frac{N_{tg2}}{N_{tgi}} \frac{N_{tg3}}{N_{tg2}} \frac{N_{mlog}}{N_{tg3}} \frac{N_{B\Delta p_z}}{N_{mlog}} \times \frac{N^{obs}(\Xi^-)}{N_{B\Delta p_z}}$$

The first four quantities, ε_{tgi} through ε_{mlog} , are the efficiencies for the TGI, TG2, TG3, and Multiplicity Logic triggers discussed in Section 2.3. The number of signals, N_{tc} , from the Target Counter is taken to be the number of incident beam protons. The fifth quantity is the fraction of all events passing the Multiplicity Logic trigger that survive a Beam Δp_z cut. This cut removes non-diffractive events in which an incoming beam proton is accompanied by a spectator beam proton. The first beam proton which interacts does not make it to the outgoing beam spectrometer but leaves other tracks in the main spectrometer. The spectator beam proton which does not interact makes it to the outgoing beam spectrometer. Such an event with extra charged tracks in the main spectrometer and a beam proton in the outgoing beam spectrometer can fake a diffractive event that satisfies the experiment's triggers and gets recorded on tape. Figure 4.1 shows a scatter plot for some events

Ξ^- selection criteria	
(a)	secondary vertex compatible with $\Xi^- \rightarrow \Lambda^0(p\pi^-)\pi^-$
(b)	Ξ^- vertex must originate from the primary vertex
(c)	Ξ^- lifetime $> 0.1 \times (1.639 \times 10^{-10} \text{ sec.})$

Table 4.1: Cuts used to select Ξ^- events for normalizing the number incident beam protons.

of the sum of the longitudinal components of the momenta of all reconstructed tracks assigned to the primary vertex versus the longitudinal component of the momentum lost by the reconstructed beam proton. The vertical band near Beam $\Delta p_z = 0$ are the fake diffractive events where the total p_z at the primary vertex is greater than the p_z lost by the beam proton. The dash-dotted line with a slope of 1.5 and a y -intercept of 1 represents the Beam Δp_z cut. Only the events below this line in the scatter plot are selected.

The last quantity in Equation 4.5 is the fraction of all events surviving the Beam Δp_z cut that have a Ξ^- . Ξ^- events are selected by requiring a reconstructed secondary vertex that is compatible with a Ξ^- (see Section 3.2). The Ξ^- must have exactly two daughter tracks assigned to it, one of which must be a composite track whose decay vertex is compatible with a $\Lambda^0 \rightarrow p\pi$. The composite track associated with the Ξ^- must be assigned to the primary and must have a proper lifetime greater than one-tenth the mean Ξ^- lifetime of 1.639×10^{-10} sec. [58]. These cuts are summarized in Table 4.1.

The second through fifth factors in Equation 4.5, ε_{tg2} through $\varepsilon_{B\Delta p_z}$, were determined using prescale events from a number of selected Pass 2 One-to-One tapes belonging to geometry groups 7 to 13. As mentioned in Section 2.3, these were events written to tape as long as they satisfied the TGI condition without any further requirements. The trigger efficiencies ε_{tg2} , ε_{tg3} , and ε_{mlog} were determined by counting the number of these prescale events surviving each of the succeeding levels—TG2, TG3, and Multiplicity Logic. The factor $\varepsilon_{B\Delta p_z}$ was calculated by counting the fraction of the prescale events surviving the Multiplicity Logic trigger that also passed the Beam Δp_z cut. Only prescales having a single incident beam proton that was not accompanied by beam halo were

4.1. DETERMINATION OF N_{BEAM}

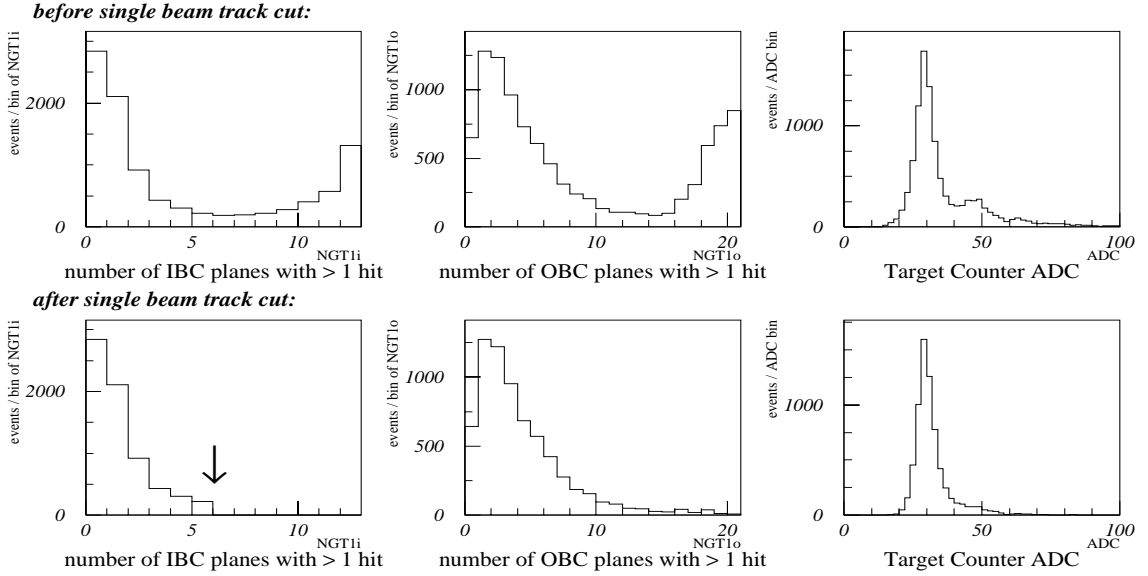


Figure 4.2: Cut used to select events with single incident beam protons.

used for these studies. The *no beam halo* requirement was imposed by requiring no signals from the Halo counter (see Section 2.2). The single incident beam proton requirement was imposed by requiring the total number of wire planes in the incoming beam chambers that have more than one hit to be less than 6. The first two plots in the first row of Figure 4.2 show the number of planes in both the incoming (IBC) and outgoing (OBC) beam chambers that have more than one wire hit. The peaks at zero in both cases correspond to single beam track events while the peaks at 12 for the IBC and at 20 for the OBC correspond to events which have more than one incident beam proton. The third plot in the first row shows the ADC signal of the Target Counter (TC) with a big peak corresponding to single beam track events followed by a series of decreasing peaks corresponding to events with two, three, or more incident beam tracks. The next three plots in the second row show the same quantities after the single beam track cut referred to above is applied. These histograms show that this cut eliminates the second peak close to 20 in the plot of the number of OBC planes having more than one hit and most of the smaller peaks following the first one in the plot of the TC ADC signal.

CHAPTER 4. CROSS SECTION MEASUREMENT

The first factor in Equation 4.5, ε_{tgi} , was determined using prescales from geometry group 3 since the TGI trigger used in this group required only the presence of a signal from the Target Counter. Once again, only prescales with single incident beam protons were selected for this calculation. The TGI efficiency, ε_{tgi} , was calculated by counting the number of prescales surviving the TGI condition ($TC \bullet OR's$) as defined for geometry groups 7 to 13. The last factor in Equation 4.5 was determined by taking all the recorded events (not just prescales) on each of the selected Pass 2 One-to-One tapes from geometry groups 7 to 13 that satisfied all of the trigger requirements plus the single incident beam proton and the Beam Δp_z cut and counting the fraction of these that were Ξ^- events meeting the requirements in Table 4.1. Thus, the normalization constant was found to be:

$$C = (2.795 \pm 0.025) \times 10^6 \frac{\text{beam protons}}{\Xi^-'s} \quad (4.6)$$

where the uncertainty is due to the finite number of events used in determining the efficiencies in Equation 4.5.

With this normalization constant, the total number of incident beam protons was determined by counting the total number of Ξ^- events meeting the selection criteria outlined in Table 4.1. In addition, these events were required to satisfy the Beam Δp_z cut and to meet all of the experiment's trigger conditions. The second additional requirement was imposed to exclude a small fraction of recorded events that did not meet the trigger conditions. Figure 4.3 plots histograms of the invariant Ξ^- mass from the selected events in each geometry group of the E690 data used in the cross section measurement. The number of Ξ^- events, $N^{obs}(\Xi^-)$, from each group is summarized in Table 4.2. Multiplying the total number of selected Ξ^- 's by the normalization factor in Equation 4.6 gives the total number of incident beam particles:

$$\begin{aligned} N_{beam} &= 446,232 \Xi^-'s \times [(2.795 \pm 0.025) \times 10^6 \text{ beam protons}/\Xi^-] \\ &= (1.247 \pm 0.011) \times 10^{11} \text{ beam protons.} \end{aligned}$$

4.1. DETERMINATION OF N_{BEAM}

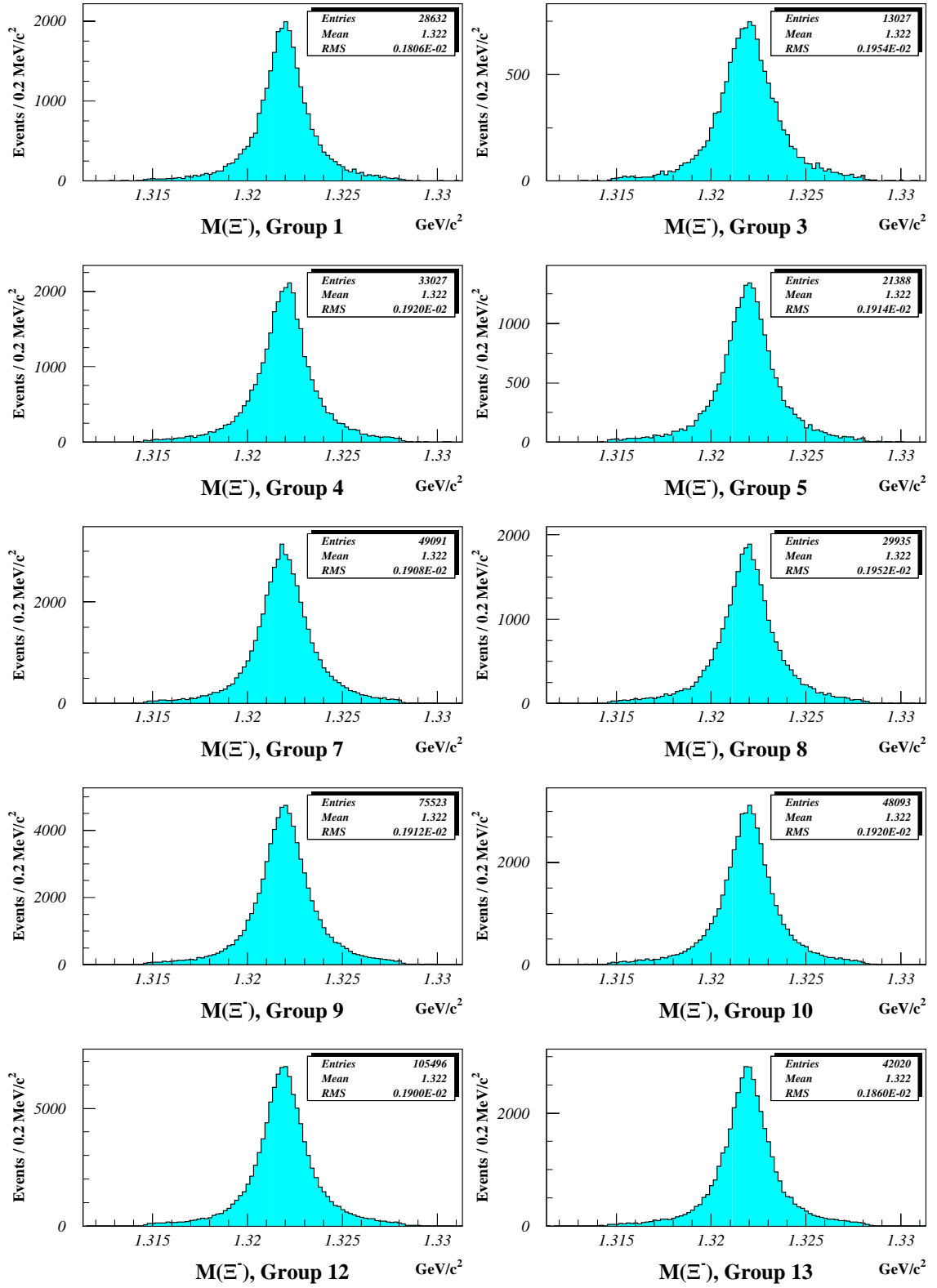


Figure 4.3: Invariant mass of the Ξ^- for events selected according to Table 4.1 from each of the geometry groups used in the cross section measurement.

Geometry Group	Number of Ξ^- 's selected
1	28632
3	13,027
4	33,027
5	21,388
7	49,091
8	29,935
9	75,523
10	48093
12	105,496
13	42,020
Total	446,232

Table 4.2: Number of Ξ^- 's selected according to Table 4.1 in each geometry group used in the cross section measurement.

4.2 Determination of $N_{\text{diff}}(c\bar{c})$

As mentioned in the introduction to this chapter, charm events were selected by identifying decays of the type $D^* \rightarrow (D^0 \rightarrow K\pi)\pi$. In this case, $N_{\text{diff}}(c\bar{c})$ can be related to the number of reconstructed D^* 's, $N_{\text{diff}}^{\text{obs}}(D^*)$, using:

$$N_{\text{diff}}(c\bar{c}) = \frac{N_{\text{diff}}^{\text{obs}}(D^*)}{\varepsilon(D^*) \times F \times B.R.(D^* \rightarrow D^0\pi) \times B.R.(D^0 \rightarrow K\pi)} \quad (4.7)$$

where $B.R.(D^0 \rightarrow K\pi)$ is the branching ratio for a D^0 to decay into a K and a π and $B.R.(D^* \rightarrow D^0\pi)$ is the branching ratio for a D^* to decay into a D^0 and a π . F is the ratio $\sigma_{\text{diff}}(D^*)/\sigma_{\text{diff}}(c\bar{c})$ or the fraction of D^* 's in a single diffractive $c\bar{c}$ event. The first factor, $\varepsilon(D^*)$, is the overall detection efficiency for events containing a decay of the type $D^* \rightarrow (D^0 \rightarrow K\pi)\pi$ and is given by:

$$\varepsilon(D^*) = (\varepsilon'_{tgi}\varepsilon'_{tg2}\varepsilon'_{tg3}\varepsilon'_{mlog}) \times \varepsilon_{\text{rec}}\varepsilon_{\text{cut}}. \quad (4.8)$$

4.2. DETERMINATION OF $N_{\text{DIFF}}(C\bar{C})$

The first four factors enclosed in parentheses are the TGI, TG2, TG3, and Multiplicity Logic trigger efficiencies for $D^* \rightarrow (D^0 \rightarrow K\pi)\pi$ events. ε_{rec} and ε_{cut} represent the reconstruction and cut efficiencies for $D^* \rightarrow (D^0 \rightarrow K\pi)\pi$ events in the track reconstruction and analysis routines.

4.2.1 Determining $N_{\text{diff}}^{obs}(D^*)$

The number of reconstructed $D^{*'}s$, $N_{\text{diff}}^{obs}(D^*)$, was determined from each of the E690 data geometry groups listed in Table 4.2. $N_{\text{diff}}^{obs}(D^*)$ was the number of events which, in addition to satisfying all the D^* candidate selection criteria described in Table 3.5 and Section 3.4, also satisfied the following requirements:

- must satisfy the Beam Δp_z cut: $\Sigma p_z(\text{primary}) < 1.5(\text{Beam}\Delta p_z) + 1$
- must meet all of the trigger requirements of the experiment
- must originate from within the Liquid Hydrogen target.
- must satisfy the coherence condition of $x_F > 0.85$ (Equation 1.1).

The histograms in Figure 4.4 show the $K\pi\pi$ invariant mass distributions for the D^{*+} and D^{*-} events meeting all these requirements. Data from Groups 1 and 3 were excluded from the D^{*+} distributions since time-of-flight particle identification was unusable due to problems with the Middle and Rear Hodoscope counters. From the fits of a Gaussian plus a linear background, $f(x) = P_1 \exp\left(-\frac{(x-P_2)^2}{2P_3^2}\right) + P_4 + P_5x$, to these two histograms, the number of reconstructed D^* 's is estimated to be $N_{\text{diff}}^{obs}(D^{*+}) = 44 \pm 11$ events and $N_{\text{diff}}^{obs}(D^{*-}) = 169 \pm 32$ events. Figure 4.5 shows histograms of the $K\pi$ invariant mass distributions of the D^0 and \bar{D}^0 's corresponding to those of the D^{*+} and D^{*-} shown in Figure 4.4. Figures 4.6 and 4.7 show the same two histograms for the D^* 's and D^0 's with the coherence condition increased to $x_F > 0.90$.

The Q distributions of the reaction $D^* \rightarrow (D^0 \rightarrow K\pi)\pi$ are shown in Figure 4.8 for both charge states. The criteria used in selecting events for these histograms were identical to those used for the

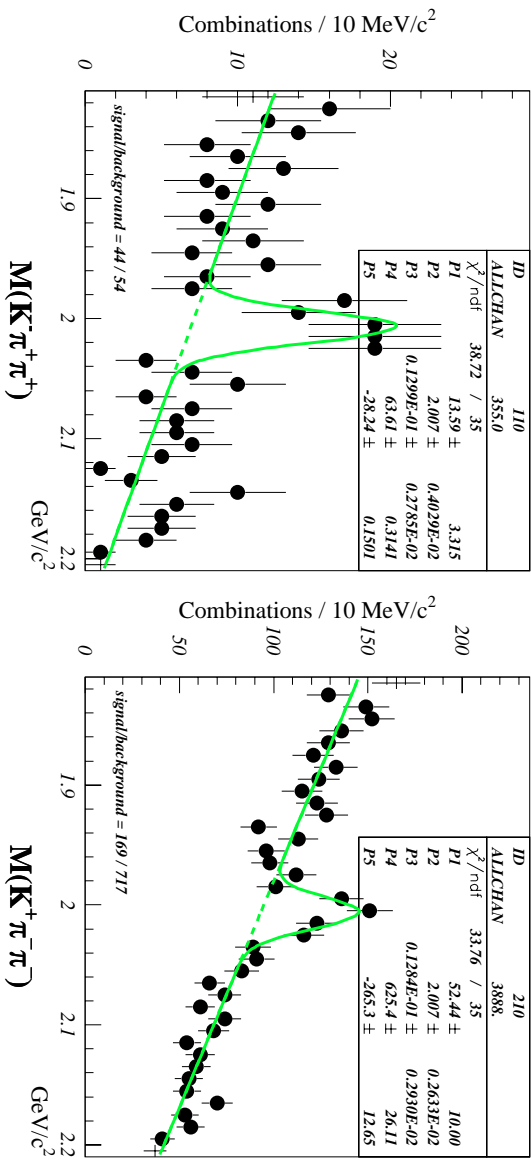


Figure 4.4: $K\pi\pi$ invariant mass distributions for the D^* candidates used in determining $N_{\text{diff}}^{\text{obs}}(D^*)$ for the cross section measurement meeting all requirements described in Section 4.2.

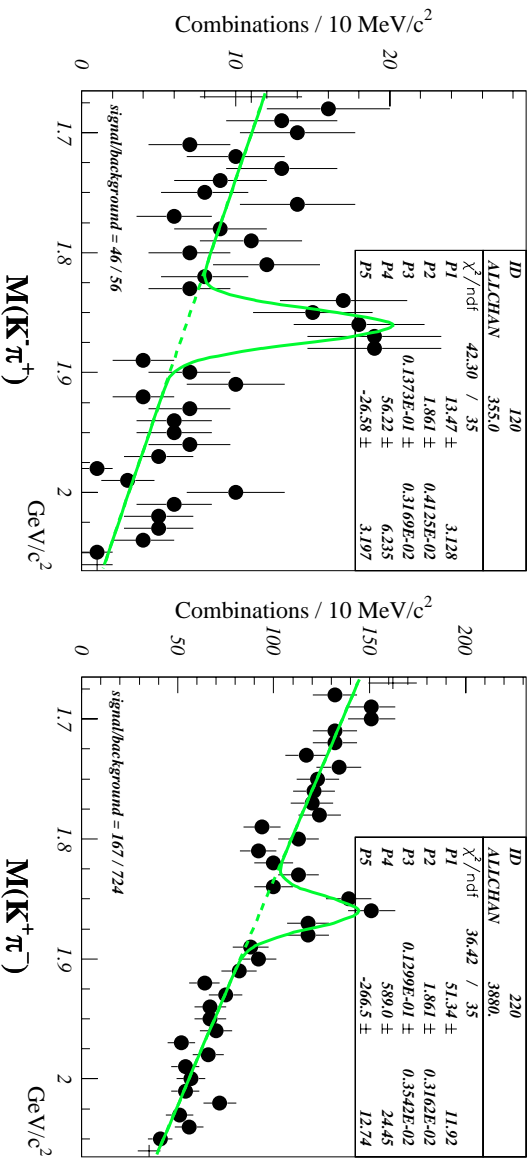


Figure 4.5: $K\pi$ invariant mass distributions of the D^0 's decaying from the D^* candidates shown in Figure 4.4

4.2. DETERMINATION OF $N_{\text{DIFF}}(C\bar{C})$

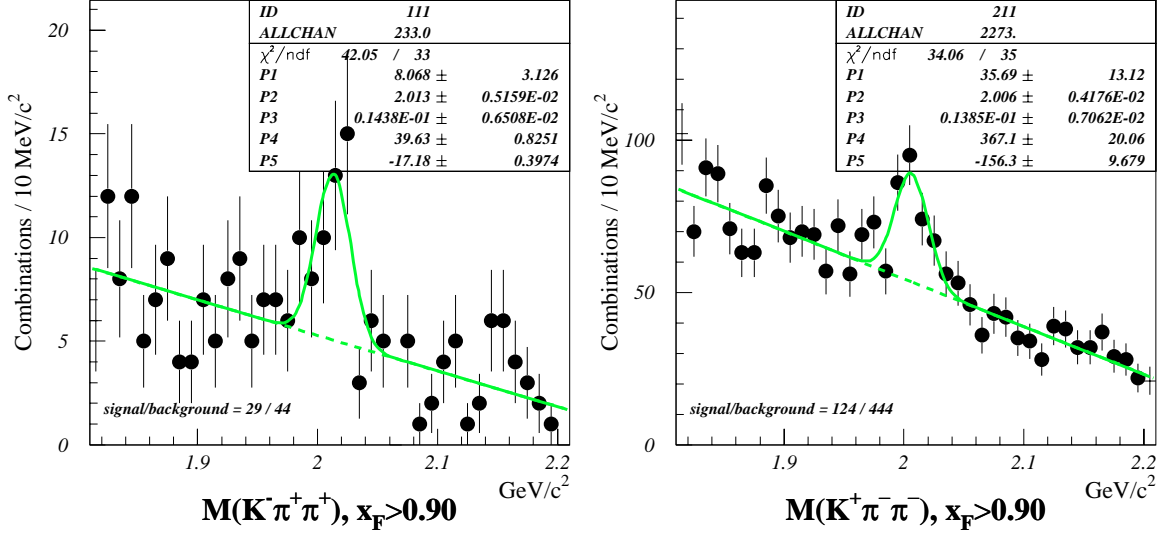


Figure 4.6: $K\pi\pi$ invariant mass distributions for the D^* candidates shown in Figure 4.4 with coherence condition increased to $x_F > 0.90$.

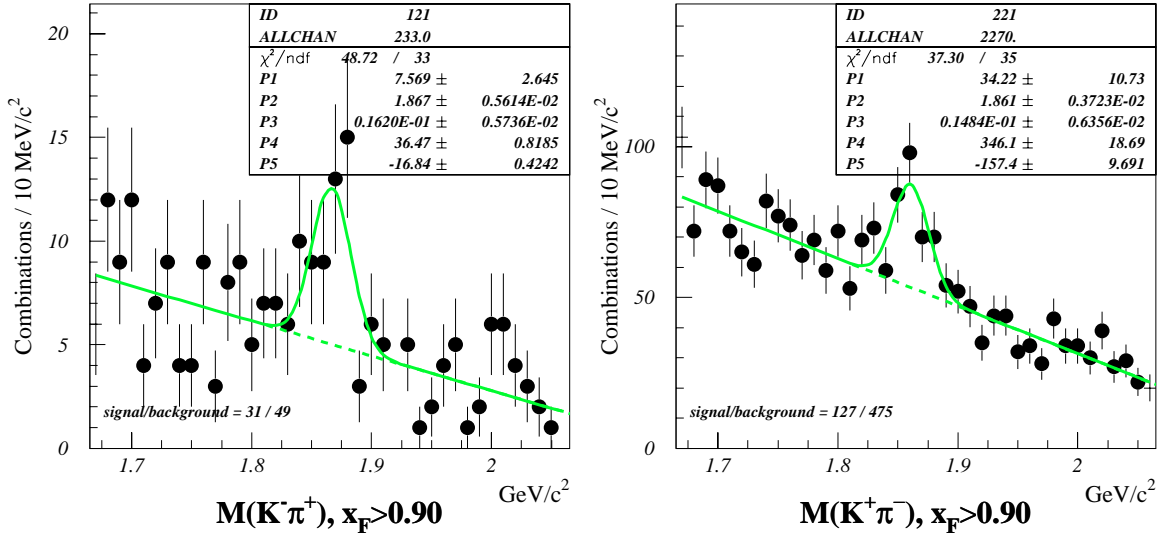


Figure 4.7: $K\pi$ invariant mass distributions of the D^0 candidates shown in Figure 4.5 with coherence condition increased to $x_F > 0.90$.

CHAPTER 4. CROSS SECTION MEASUREMENT

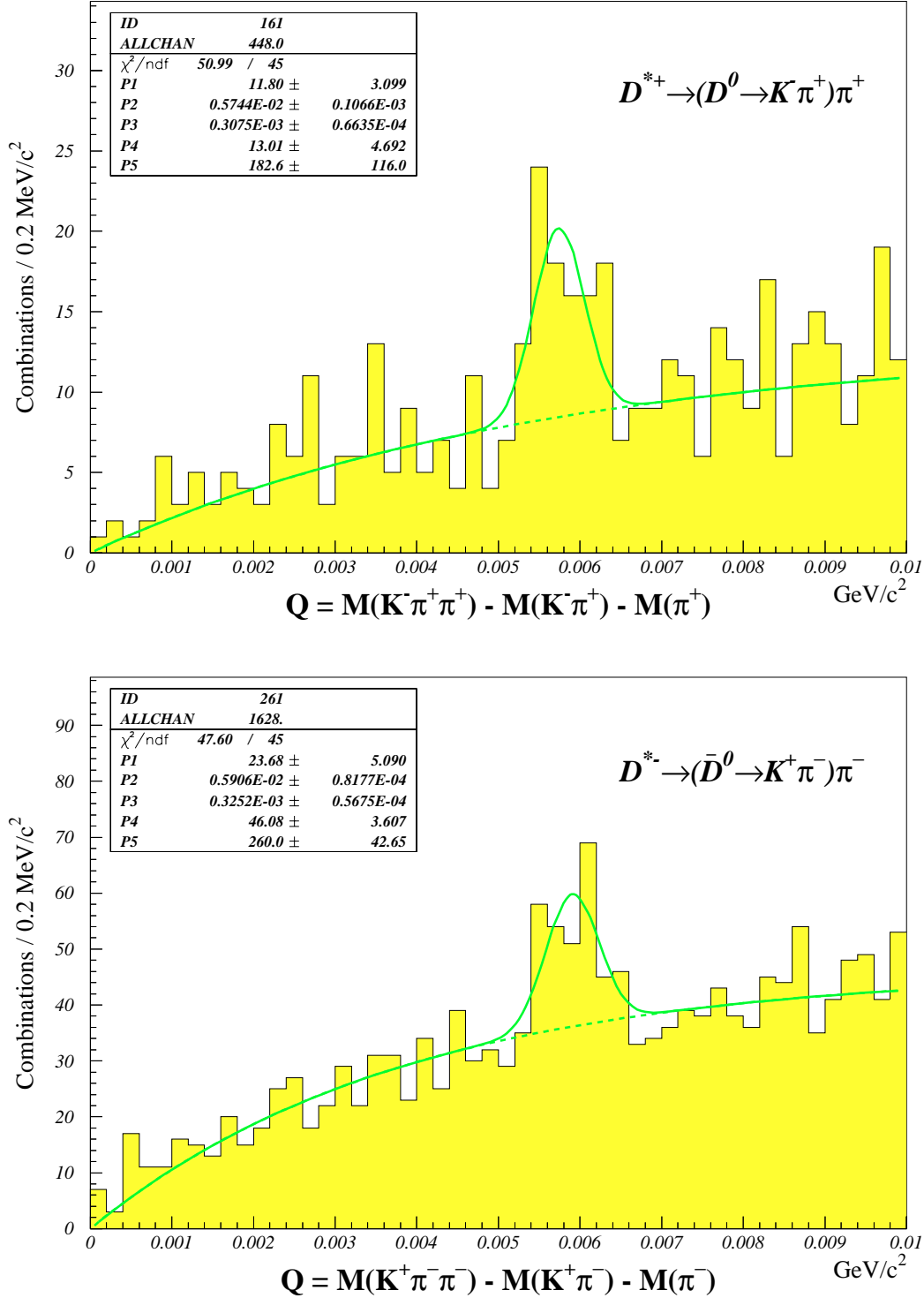


Figure 4.8: Q distributions of the D^* candidate events whose invariant mass distributions are shown in Figure 4.4. The $K^- \pi^+ \pi^+$ invariant mass for the top plot was required to be within 30 MeV/c^2 of 2.010 GeV/c^2 . For the bottom plot, the $K^+ \pi^- \pi^-$ invariant mass was required to be within 10 MeV/c^2 of 2.010 GeV/c^2 . Refer to Section 4.2 for details on the fit parameters.

4.2. DETERMINATION OF $N_{\text{DIFF}}(C\bar{C})$

invariant mass histograms in Figure 4.4 except that the cut on Q was replaced with a cut on the $K\pi\pi$ invariant mass. For the Q distribution of the D^{*+} candidates in Figure 4.8, the $K^-\pi^+\pi^+$ invariant mass was required to be $|M(K\pi\pi) - 2.010 \text{ GeV}/c^2| < .03 \text{ GeV}/c^2$. For the D^{*-} candidates, the $K^+\pi^-\pi^-$ invariant mass was required to be $|M(K\pi\pi) - 2.010 \text{ GeV}/c^2| < .01 \text{ GeV}/c^2$. Fitting these distributions to the functional form $f(x) = P_1 \exp\left(-\frac{(x-P_2)^2}{2P_3^2}\right) + P_4(1 - e^{-P_5x})$, consisting of a gaussian and an exponential, yielded mean values of $Q = .00574 \pm .0001 \text{ GeV}/c^2$ for the D^{*+} reaction and $Q = .00591 \pm .00008 \text{ GeV}/c^2$ for the D^{*-} reaction. These values are consistent with the value of $Q = M(D^*) - M(D^0) - M(\pi) = (2.01 - 1.8646 - .13957) \text{ GeV}/c^2 = .000583 \text{ GeV}/c^2$ calculated using the masses of the D^* , D^0 , and π from Reference [58]. The gaussian widths of both Q distributions are roughly $\sigma \simeq 3 \text{ MeV}/c^2$.

Distributions for the fractional momenta, $x_F = p_{||}/p_{||,max}$, of the D^* , p_{fast} , and X system in the c.m. frame of the initial state protons are shown in Figure 4.9. In this case, p_{fast} refers to the scattered beam proton and the X system refers to all other particles produced by the pp interaction excluding the D^* . These distributions show that the D^* is well separated in x_F from the scattered forward proton. Rapidity gaps ($rapidity = y = \frac{1}{2} \ln\left(\frac{E+P_L}{E-P_L}\right)$) are often taken as a signature of a diffractive interaction (see Section 1.3.1). In Figure 4.10, rapidity distributions of the the D^* , p_{fast} , and X system are shown. A wide gap spanning four or more units of rapidity is clearly seen separating the scattered beam proton from the D^* and the other products of the pp interaction. This gap, however, cannot be equated with the absence of hadronic activity since the E690 detector has no acceptance in this region of rapidity. The events used to plot both the x_F and rapidity distributions are exactly the same events used to produce the invariant mass distributions in Figure 4.4.

Transverse momentum squared, p_T^2 , distributions of the scattered beam proton for the D^* candidates are shown in Figure 4.11. In addition to the selection criteria for the events in Figure 4.4, these events were required to satisfy a tighter mass cut of $|M(K\pi\pi) - 2.010| < 0.03 \text{ GeV}/c^2$. Both distributions exhibit strong forward peaks that decay exponentially with slope parameters of $|b| \simeq 8 - 9$

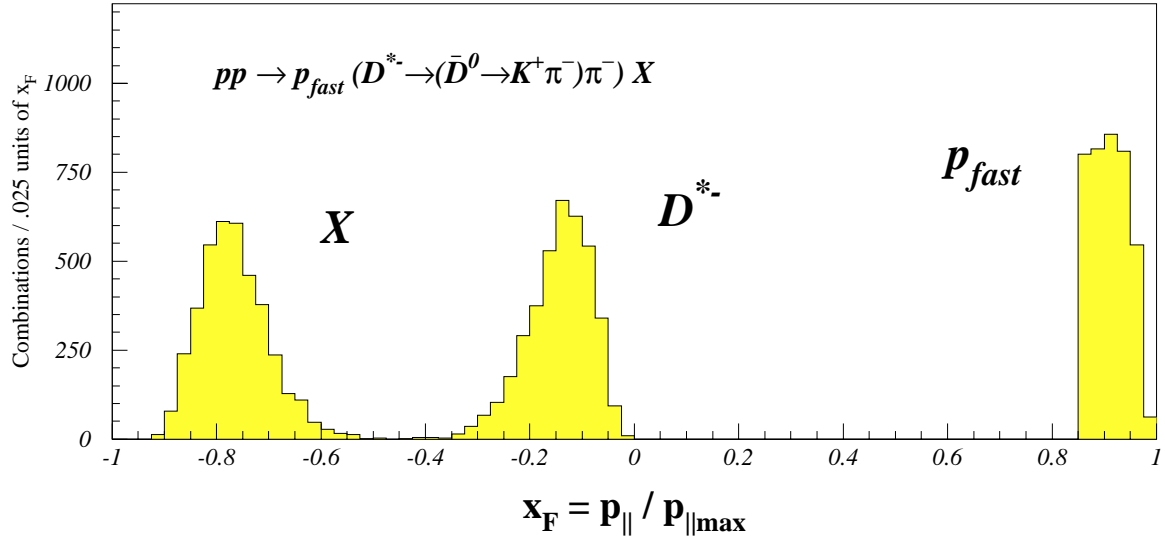
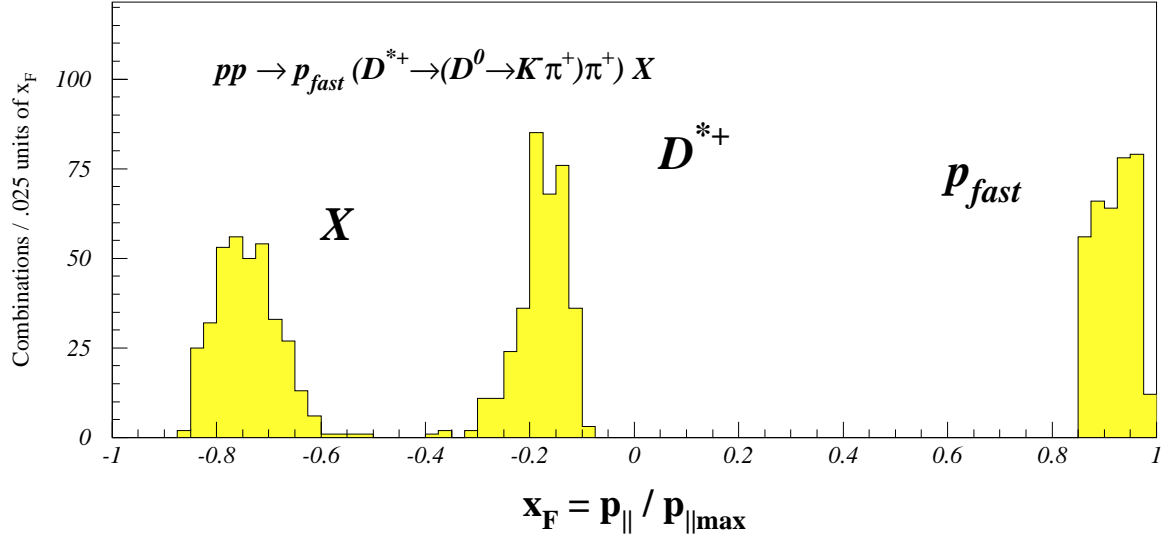


Figure 4.9: x_F distributions of the D^* , X system, and scattered beam proton, p_{fast} , of the D^* candidate events selected for the cross section measurement.

4.2. DETERMINATION OF $N_{\text{DIFF}}(C\bar{C})$

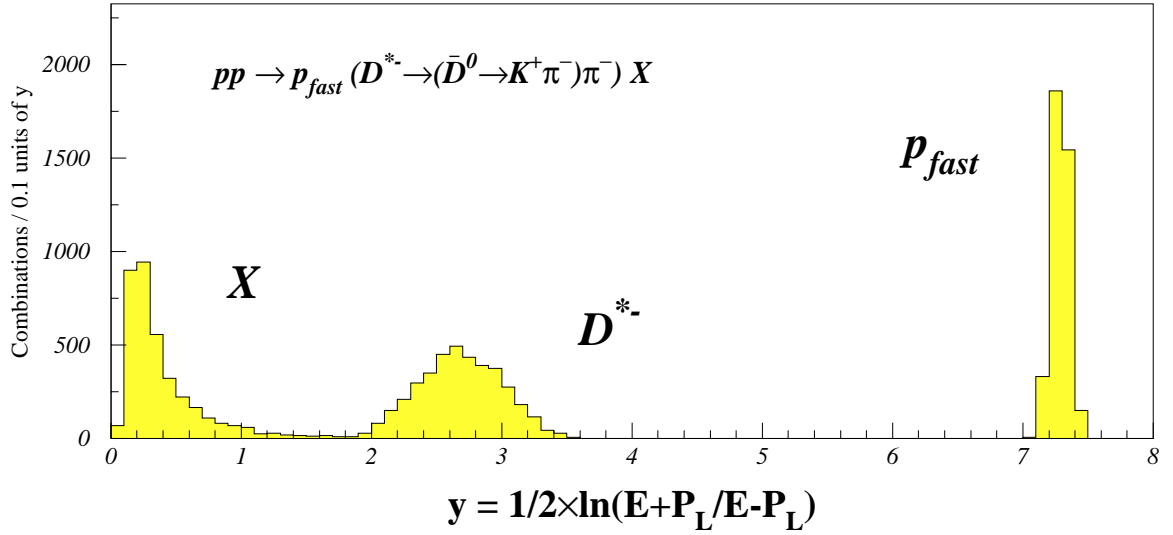
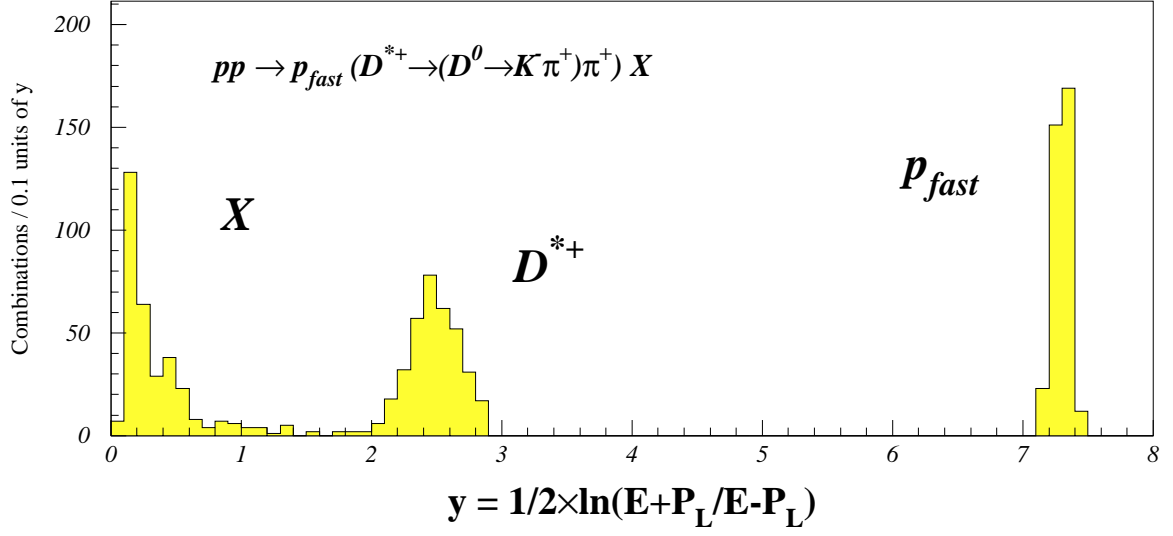


Figure 4.10: Rapidity, y , distributions of the D^* , X system, and scattered beam proton, p_{fast} , of the D^* candidate events selected for the cross section measurement.

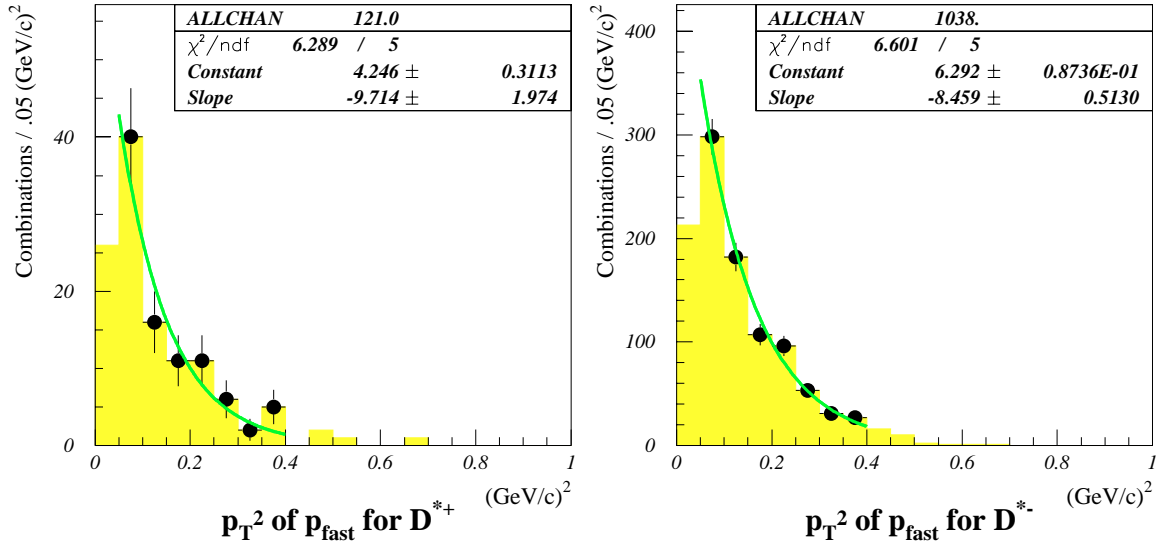


Figure 4.11: p_T^2 distributions of the scattered beam proton for the selected D^{*+} and D^{*-} candidate events. Both distributions exhibit exponentially decaying forward peaks characteristic of diffraction.

$(\text{GeV}/c)^{-2}$. As mentioned in Section 1.1, these are characteristics associated with diffraction. The first bin in both p_T^2 distributions show a depletion of events. This is because the Pass 2 vertex reconstruction program described in Section 3.2 required interacted beam protons with $p_T^2 > 0$.

Figure 4.12 shows a 2-dimensional histogram of the invariant $K^-\pi^+\pi^+$ mass against the fractional momentum, x_F , of the scattered beam proton for the D^{*+} candidate events. The events used to make these histograms satisfy the same set of requirements as those of Figure 4.4 except that the coherence condition of $x_F > 0.85$ was not imposed. Figure 4.13 shows the same histograms for the D^{*-} candidates.

4.2.2 D^* Acceptance Calculation

The overall D^* acceptance, $\varepsilon(D^*)$, was determined using the Monte Carlo technique. Complete $D^* \rightarrow (D^0 \rightarrow K\pi)\pi$ events were generated using POMPYT 2.6 [29] and PYTHIA 5.7 [66]. POMPYT is a program that works in conjunction with PYTHIA to generate single diffractive events based on the model of Ingelman and Schlein [1] (see also Section 1.3.1). Pomeron emission from the incident proton is simulated by POMPYT and the subsequent hard scattering process between the partonic

4.2. DETERMINATION OF $N_{\text{DIFF}}(C\bar{C})$

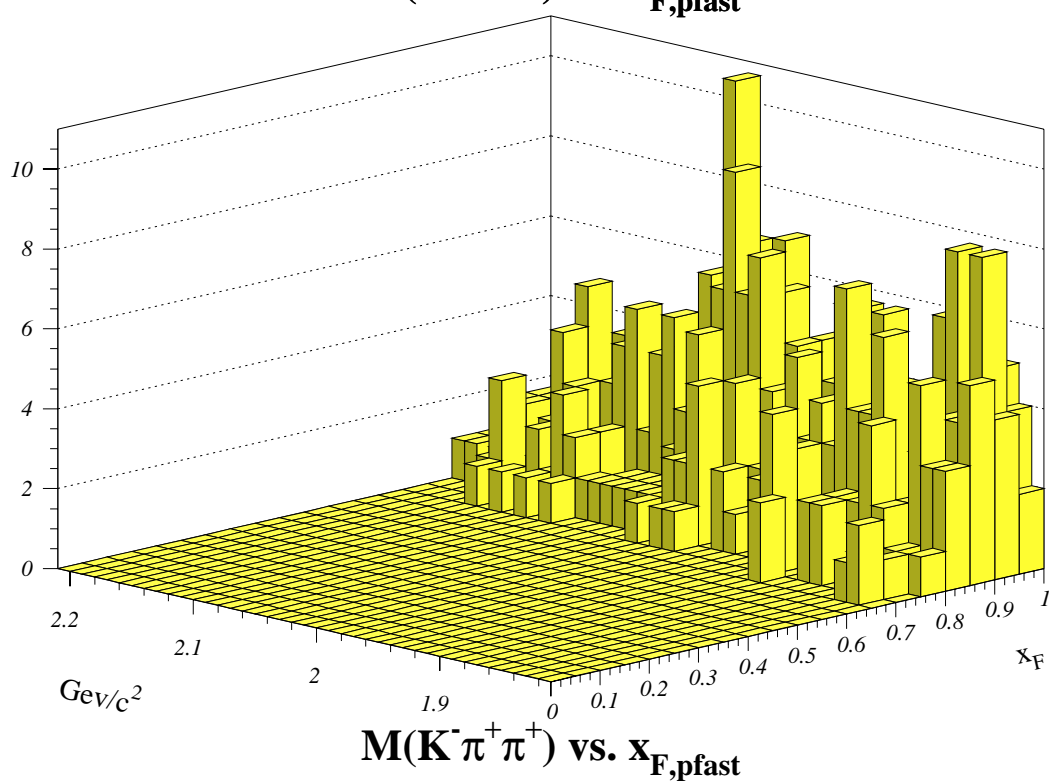
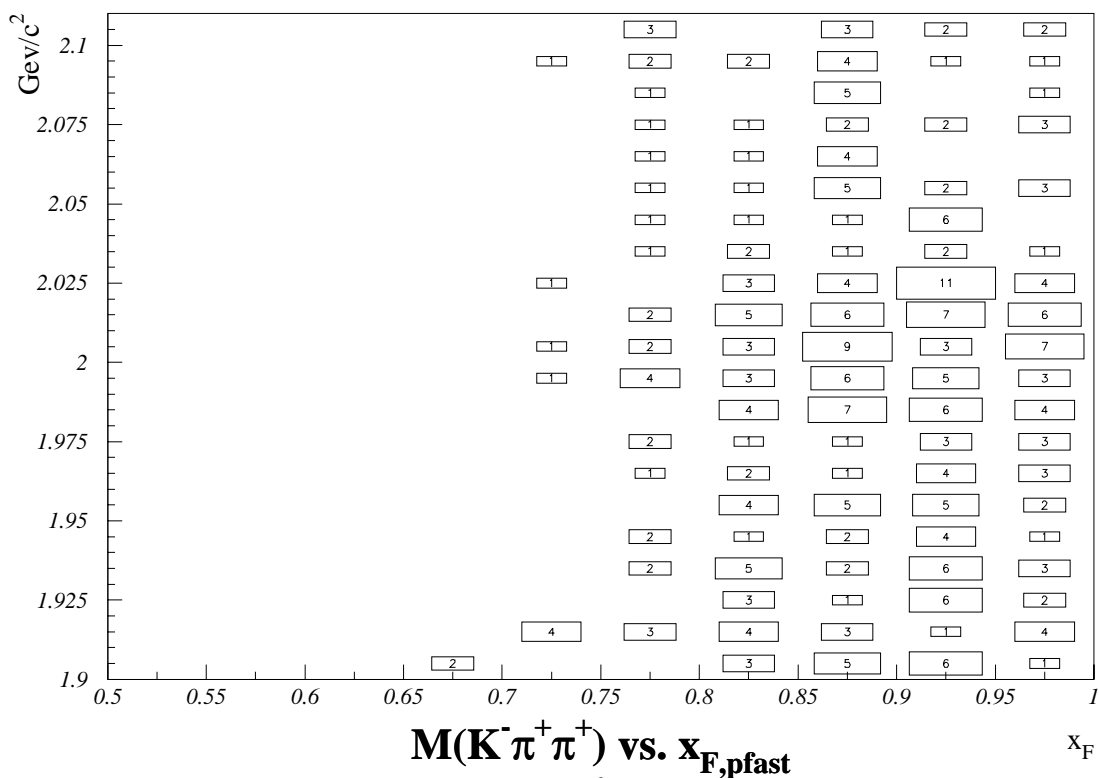


Figure 4.12: Invariant $K^- \pi^+ \pi^+$ mass in $10 \text{ MeV}/c^2$ bins plotted versus x_F of the scattered beam proton for the D^{*+} candidate events.

CHAPTER 4. CROSS SECTION MEASUREMENT

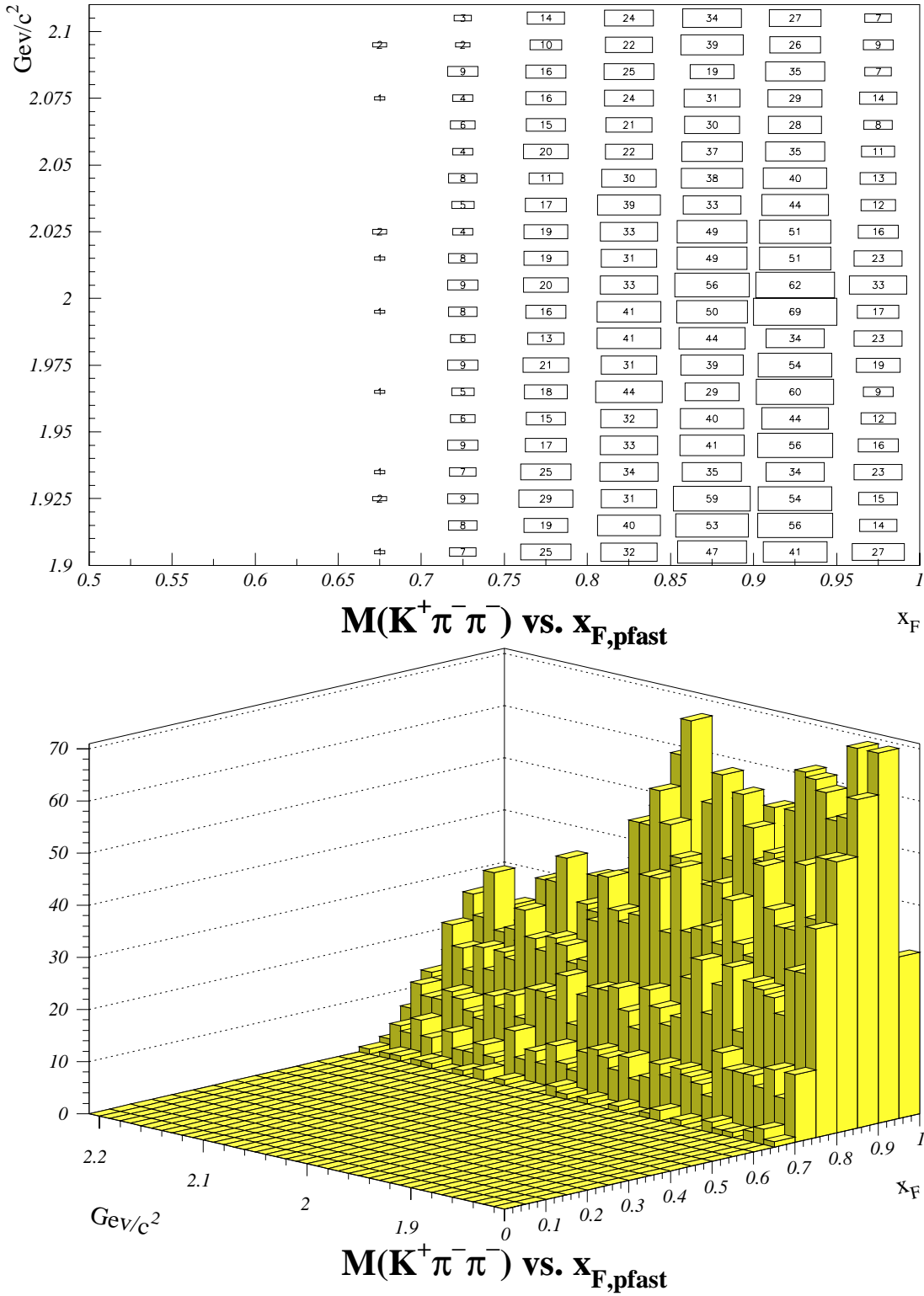


Figure 4.13: Invariant $K^+ \pi^- \pi^-$ mass in $10 \text{ MeV}/c^2$ bins plotted versus x_F of the scattered beam proton for the D^{*-} candidate events.

4.2. DETERMINATION OF $N_{\text{DIFF}}(C\bar{C})$

constituents of the pomeron and those of the target proton are simulated by PYTHIA based on the LUND string fragmentation model [67].

In generating charm events, only the leading order processes, $qq \rightarrow c\bar{c}$ and $gg \rightarrow c\bar{c}$, were turned on in PYTHIA. The pomeron flux factor used was the standard form of Donnachie and Landshoff [27, 28]:

$$f_{\mathcal{P}/p}(x_{\mathcal{P}}, t) = \frac{9\beta_0^2}{4\pi^2} [F_1(t)]^2 \left(\frac{1}{x_{\mathcal{P}}}\right)^{2\alpha(t)-1} \quad (4.9)$$

with a pomeron-quark coupling constant of $\beta_0^2 = 3.24 \text{ GeV}^{-2}$ and a pomeron Regge trajectory given by [30]:

$$\alpha(t) = 1 + 0.115 + 0.26t.$$

The t dependence of the flux factor is contained in the proton form factor given by [28]:

$$F_1(t) = \frac{4m_p^2 - 2.8t}{4m_p^2 - t} \left(\frac{1}{1 - t/0.7}\right)^2. \quad (4.10)$$

The pomeron structure function used was one composed of quarks and gluons:

$$f_{\mathcal{P}}(z) = R_q f_{q/\mathcal{P}}(z) + (1 - R_q) f_{g/\mathcal{P}}(z) \quad (4.11)$$

with a quark fraction of $R_q = 0.46$ [22] and a *flat* parton density function given by:

$$f_{q,g/\mathcal{P}}(z) = \frac{1}{z}. \quad (4.12)$$

Figure 4.14 compares the flat parton density function with two other commonly used forms, the *soft* distribution given by:

$$f_{q,g/\mathcal{P}}(z) = \frac{6(1-z)^5}{z} \quad (4.13)$$

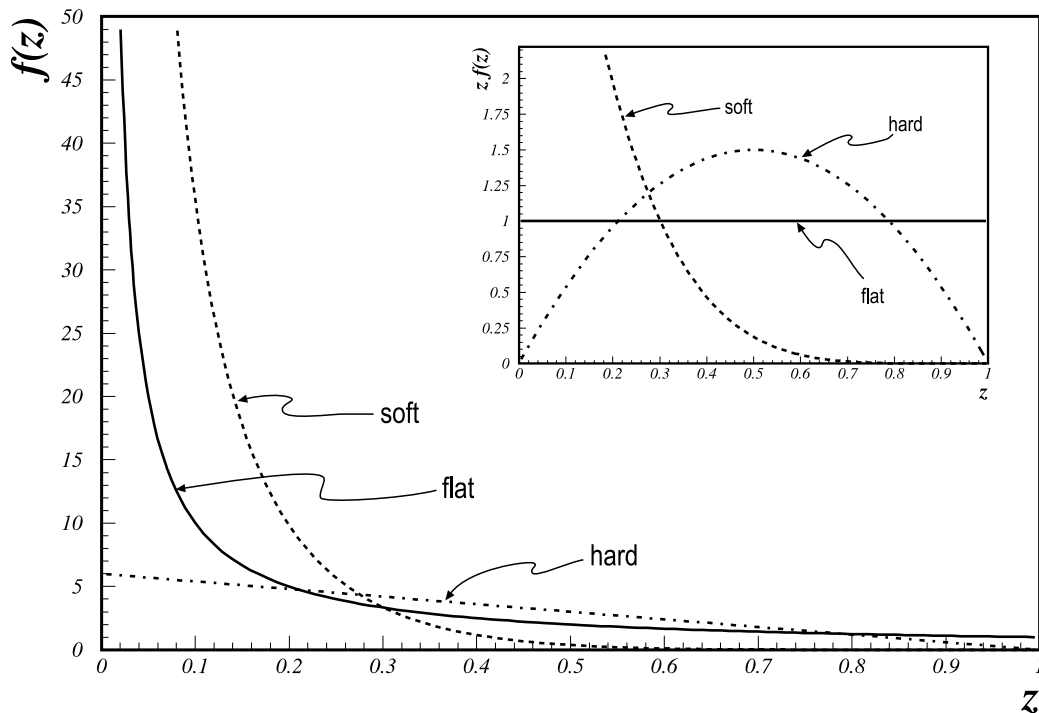


Figure 4.14: Comparison of the *flat*, *soft*, and *hard* parton distribution functions of Equations 4.12 to 4.14. The inset shows plots of the same distributions multiplied by z .

and the *hard* distribution of:

$$f_{q,g/P}(z) = 6(1 - z). \quad (4.14)$$

Events were generated from a minimum X system mass of $M_X \sim 4.8 \text{ GeV}/c^2$ to a maximum of $M_X \sim 15 \text{ GeV}/c^2$. The minimum value corresponds to the charm threshold of $M(D^0) + M(\Lambda_c)$ in pp interactions. The maximum value corresponds to the coherence condition of $x_F > 0.85$ for the fast proton as defined in Equation 1.1. Parameter settings used in POMPYT are shown in Appendix B.

Instead of using JETSET [66] to handle decays, all unstable particles generated by PYTHIA were decayed using specially written code. This code decayed the particles with correct lifetimes [58] into an allowed channel randomly selected according to known branching fractions [58] in the case of the seen decay modes and branching fractions estimated from available phase space in the case of the unseen modes. Photons were also allowed to convert into e^+/e^- pairs in the material of the detector at a frequency determined by the pair production cross section for that material [68–70].

4.2. DETERMINATION OF $N_{\text{DIFF}}(C\bar{C})$

Using the generator described above, two inclusive samples for the D^{*+} and the D^{*-} were produced. The only requirement for each event was the presence of at least one D^* of the correct charge which was forced to decay through the channel $D^* \rightarrow D^0(K\pi)\pi$. All other unstable particles were allowed to decay into all possible channels using the method described in the previous paragraph. The generated events were propagated through a Monte Carlo simulation of the detector using code specifically written for experiment E690. Relevant physics processes such as multiple Coulomb scattering and energy loss straggling were included in the detector simulation. The output of the simulation, which was written in a format identical to that of a real data tape, was then subjected to the same track finding, vertex reconstruction, and analysis stages as the real data.

The D^* acceptance, $\varepsilon(D^*)$, was calculated by taking the ratio of reconstructed events to generated events. This was done for the three different trigger conditions used in Groups 1-3, 4-5, and 7-13 of the E690 data set (see Table 2.3). Roughly 5×10^9 events were generated for these calculations. The acceptance calculated using the pomeron structure function of Equation 4.11 with the flat distribution of Equation 4.12 and $R_q = 0.46$ is shown in the first two rows of Table 4.3. For comparison, the acceptances calculated using a pomeron structure function consisting only of quarks ($R_q = 1$) or only of gluons ($R_q = 0$) for all three parton distribution functions described by Equations 4.12 to 4.14 are also presented in the same table. The number of events generated for each of these other cases was one tenth that of the *flat quark+gluon* case. All acceptances are calculated for both coherence conditions of $x_F > 0.85$ and $x_F > 0.90$.

4.2.3 Results for $N_{\text{diff}}(c\bar{c})$

Using the acceptances calculated with the *flat quark+gluon* distribution function shown in the first two rows of Table 4.3, weighted versions of the histograms shown in Figure 4.4 were made. Each invariant $K\pi\pi$ mass combination was entered $1/\varepsilon(D^*)$ times into these weighted histograms, where $\varepsilon(D^*)$ corresponded to the acceptance for the geometry group the event belonged to. These weighted histograms were then fitted to a Gaussian plus a linear background to determine the

CHAPTER 4. CROSS SECTION MEASUREMENT

Parton distribution $f_{g,q/\mathbb{P}}(z)$	Charge state	D^* Acceptance for $x_F > 0.85$			D^* Acceptance for $x_F > 0.90$		
		Trigger conditions			Trigger conditions		
		Grp 1-3	Grp 4-5	Grp 7-13	Grp 1-3	Grp 4-5	Grp 7-13
<i>flat quark+gluon</i> $R_q = 0.46$	D^{*+}	0.0260	0.0260	0.0250	0.0313	0.0313	0.0301
	D^{*-}	0.0939	0.0939	0.0904	0.1158	0.1158	0.1115
<i>soft quark</i> $R_q = 1$	D^{*+}	0.0296	0.0296	0.0284	0.0282	0.0282	0.0272
	D^{*-}	0.1262	0.1261	0.1216	0.1483	0.1481	0.1428
<i>soft gluon</i> $R_q = 0$	D^{*+}	0.0188	0.0188	0.0180	0.0241	0.0241	0.0231
	D^{*-}	0.0887	0.0887	0.0854	0.1107	0.1107	0.1068
<i>flat quark</i> $R_q = 1$	D^{*+}	0.0320	0.0319	0.0308	0.0358	0.0358	0.0345
	D^{*-}	0.1059	0.1058	0.1019	0.1285	0.1284	0.1236
<i>flat gluon</i> $R_q = 0$	D^{*+}	0.0235	0.0235	0.0226	0.0291	0.0291	0.0280
	D^{*-}	0.0891	0.0891	0.0858	0.1099	0.1098	0.1057
<i>hard quark</i> $R_q = 1$	D^{*+}	0.0322	0.0322	0.0310	0.0359	0.0359	0.0345
	D^{*-}	0.1047	0.1046	0.1006	0.1282	0.1281	0.1232
<i>hard gluon</i> $R_q = 0$	D^{*+}	0.0233	0.0233	0.0224	0.0286	0.0286	0.0274
	D^{*-}	0.0901	0.0901	0.0867	0.1115	0.1114	0.1073

Table 4.3: D^* acceptance, $\varepsilon(D^*)$, calculated using POMPYT events generated with the three different parton density functions shown in Figure 4.14 for each trigger condition (see Section 2.3). The pomeron is assumed to be a mixture of quarks and gluons such that $R_q + R_g = 1$, where R_q is the quark fraction and R_g is the gluon fraction. Acceptances are shown for both coherence conditions of $x_F > 0.85$ and $x_F > 0.90$.

ratio $N_{\text{diff}}^{\text{obs}}(D^*)/\varepsilon(D^*)$ in Equation 4.7 which is equivalent to the acceptance-corrected number of

$D^* \rightarrow (D^0 \rightarrow K\pi)\pi$ events

$$N_{\text{diff}}(D^{*+} \rightarrow (D^0 \rightarrow K^- \pi^+) \pi^+) = \frac{N_{\text{diff}}^{\text{obs}}(D^{*+})}{\varepsilon(D^{*+})} = [1, 786 \pm 429(\text{stat})] \text{ events}$$

$$N_{\text{diff}}(D^{*-} \rightarrow (\bar{D}^0 \rightarrow K^+ \pi^-) \pi^-) = \frac{N_{\text{diff}}^{\text{obs}}(D^{*-})}{\varepsilon(D^{*-})} = [1, 849 \pm 388(\text{stat})] \text{ events}$$

where the errors include contributions from statistical uncertainties in the determination of the beam normalization factor in Equation 4.6, in the fits, and in the acceptance calculation. Using the

4.2. DETERMINATION OF $N_{\text{DIFF}}(C\bar{C})$

Parton distribution $f_{q,g/\mathbb{P}}(z)$	$x_F > 0.85$		$x_F > 0.90$	
	$\frac{\sigma_{\text{diff}}(D^{*+})}{\sigma_{\text{diff}}(c\bar{c})}$	$\frac{\sigma_{\text{diff}}(D^{*-})}{\sigma_{\text{diff}}(c\bar{c})}$	$\frac{\sigma_{\text{diff}}(D^{*+})}{\sigma_{\text{diff}}(c\bar{c})}$	$\frac{\sigma_{\text{diff}}(D^{*-})}{\sigma_{\text{diff}}(c\bar{c})}$
<i>flat quark+gluon</i> ($R_q = 0.46$)	26.7%	28.6%	26.2%	28.0%
<i>soft quark</i> ($R_q = 1$)	20.4%	30.4%	17.7%	30.5%
<i>soft gluon</i> ($R_q = 0$)	23.0%	28.6%	21.9%	28.0%
<i>flat quark</i> ($R_q = 1$)	27.6%	28.7%	26.5%	28.1%
<i>flat gluon</i> ($R_q = 0$)	26.7%	28.7%	26.1%	28.3%
<i>hard quark</i> ($R_q = 1$)	27.6%	29.0%	26.5%	28.3%
<i>hard gluon</i> ($R_q = 0$)	26.2%	28.9%	25.7%	28.4%

Table 4.4: The factor $F = \sigma_{\text{diff}}(D^*)/\sigma_{\text{diff}}(c\bar{c})$ in Equation 4.7 determined from POMPYPY for each parton distribution function and for the two coherence conditions $x_F > 0.85$ and $x_F > 0.90$.

following branching ratios from Ref. [58]:

$$\begin{aligned}
 B.R.(D^* \rightarrow D^0\pi) &= (68.3 \pm 1.4)\% \\
 B.R.(D^0 \rightarrow K\pi) &= (3.85 \pm 0.09)\%.
 \end{aligned}
 \tag{4.15}$$

we find the total number of $D^{*\pm}$'s to be:

$$\begin{aligned}
 N_{\text{diff}}(D^{*+}) &= [67,920 \pm 16,301(\text{stat})] \text{ events} \\
 N_{\text{diff}}(D^{*-}) &= [70,316 \pm 15,469(\text{stat})] \text{ events}
 \end{aligned}$$

where the errors include the uncertainties in the branching fractions. The factor F in Equation 4.7 was determined from POMPYPY by calculating the fraction of all charm events generated that had a D^* present. The values for the *flat quark+gluon* distribution is shown in the first row of Table 4.4. The values for the *soft*, *flat*, and *hard distributions* for pomerons consisting only of quarks or only of gluons is also included in the table for comparison. These fractions are determined for both coherence conditions of $x_F > 0.85$ and $x_F > 0.90$. Using F determined from POMPYPY with the *flat quark+gluon* distribution and for the coherence condition $x_F > 0.85$, the total number of single

CHAPTER 4. CROSS SECTION MEASUREMENT

diffractive charm events during the live time of the experiment is found from the reconstructed D^* events to be:

$$\begin{aligned} \text{using } D^{*+} \text{ data} & : N_{\text{diff}}(c\bar{c}) = \frac{1786}{.267 \times .683 \times .0385} = [254,383 \pm 61,052(\text{stat})] \text{ events} \\ \text{using } D^{*-} \text{ data} & : N_{\text{diff}}(c\bar{c}) = \frac{1849}{.286 \times .683 \times .0385} = [245,861 \pm 54,089(\text{stat})] \text{ events.} \end{aligned}$$

4.3 Total cross section

The total single diffractive $D^{*\pm}$ cross section is calculated using the following values of the constants:

$$\begin{aligned} A & = 1.00794 \text{ gm/mole} \\ N_A & = 6.0221367 \times 10^{23} / \text{mole} \\ \rho & = .0708 \text{ gm/cm}^3 \\ l & = 5.45 \text{ in} = 13.84 \text{ cm} \end{aligned}$$

in the cross section equation:

$$\sigma_{\text{diff}}(c\bar{c}) = \frac{A}{N_A \rho l} \frac{N_{\text{diff}}(D^{*\pm})}{N_{\text{beam}}} \times 2$$

with a factor of 2 included to account for the fact that our measurement was confined to only one hemisphere of the diffractive reaction. The calculated cross sections using the results for $N_{\text{diff}}(D^{*\pm})$ and N_{beam} determined above are thus:

$$\begin{aligned} \sigma_{\text{diff}}(D^{*+}) & = [0.209 \pm .050(\text{stat})_{-.040}^{+.083}(\text{syst})] \mu\text{b} \\ \sigma_{\text{diff}}(D^{*-}) & = [0.196 \pm .043(\text{stat})_{-.046}^{+.014}(\text{syst})] \mu\text{b}. \end{aligned}$$

4.3. TOTAL CROSS SECTION

Parton distribution $f_{g,q/\mathbb{P}}(z)$	$x_F > 0.85$			
	$\sigma_{\text{diff}}(D^{*+})$	$\sigma_{\text{diff}}(c\bar{c})$	$\sigma_{\text{diff}}(D^{*-})$	$\sigma_{\text{diff}}(c\bar{c})$
<i>flat quark+gluon</i> ($R_q = 0.46$)	$0.209 \pm 0.050 \mu\text{b}$	$0.78 \pm 0.19 \mu\text{b}$	$0.196 \pm 0.043 \mu\text{b}$	$0.69 \pm 0.15 \mu\text{b}$
<i>soft quark</i> ($R_q = 1$)	$0.184 \pm 0.044 \mu\text{b}$	$0.90 \pm 0.22 \mu\text{b}$	$0.15 \pm 0.028 \mu\text{b}$	$0.480 \pm 0.092 \mu\text{b}$
<i>soft gluon</i> ($R_q = 0$)	$0.292 \pm 0.068 \mu\text{b}$	$1.27 \pm 0.29 \mu\text{b}$	$0.21 \pm 0.045 \mu\text{b}$	$0.73 \pm 0.16 \mu\text{b}$
<i>flat quark</i> ($R_q = 1$)	$0.171 \pm 0.039 \mu\text{b}$	$0.62 \pm 0.14 \mu\text{b}$	$0.17 \pm 0.033 \mu\text{b}$	$0.60 \pm 0.12 \mu\text{b}$
<i>flat gluon</i> ($R_q = 0$)	$0.231 \pm 0.055 \mu\text{b}$	$0.87 \pm 0.21 \mu\text{b}$	$0.21 \pm 0.041 \mu\text{b}$	$0.72 \pm 0.14 \mu\text{b}$
<i>hard quark</i> ($R_q = 1$)	$0.169 \pm 0.038 \mu\text{b}$	$0.61 \pm 0.14 \mu\text{b}$	$0.18 \pm 0.037 \mu\text{b}$	$0.61 \pm 0.13 \mu\text{b}$
<i>hard gluon</i> ($R_q = 0$)	$0.237 \pm 0.053 \mu\text{b}$	$0.91 \pm 0.20 \mu\text{b}$	$0.20 \pm 0.042 \mu\text{b}$	$0.71 \pm 0.14 \mu\text{b}$

Table 4.5: Total single diffractive charm cross sections calculated with the values of $F = \sigma_{\text{diff}}(D^*)/\sigma_{\text{diff}}(c\bar{c})$ and $\varepsilon(D^*)$ determined using POMPYT with different parton density functions for the pomeron. Also shown are the total single diffractive $D^{*\pm}$ cross sections, $\sigma_{\text{diff}}(D^{*\pm})$. The coherence condition imposed on the scattered beam proton is $x_F > 0.85$. Errors shown are statistical only.

Using the same equation with $N_{\text{diff}}(D^{*\pm})$ replaced with the results for $N_{\text{diff}}(c\bar{c})$ determined above give the following results for the total single diffractive charm cross section:

$$\text{using } D^{*+} \text{ data : } \quad \sigma_{\text{diff}}(c\bar{c}) = [0.78 \pm 0.19(\text{stat})_{-17}^{+49}(\text{syst})] \mu\text{b}$$

$$\text{using } D^{*-} \text{ data : } \quad \sigma_{\text{diff}}(c\bar{c}) = [0.69 \pm 0.15(\text{stat})_{-21}^{+04}(\text{syst})] \mu\text{b}.$$

The systematic errors for the diffractive D^* and $c\bar{c}$ cross sections presented above are determined from the variation of these cross sections depending on the model of the pomeron (*soft*, *flat*, or *hard* consisting only of quarks or gluons) used in POMPYT for the acceptance correction. The cross sections determined using these different models are shown in Table 4.5. The same cross sections are also presented in Table 4.6 for the coherence condition of $x_F > 0.90$.

Parton distribution $f_{g,q/\mathcal{P}}(z)$	$x_F > 0.90$			
	$\sigma_{\text{diff}}(D^{*+})$	$\sigma_{\text{diff}}(c\bar{c})$	$\sigma_{\text{diff}}(D^{*-})$	$\sigma_{\text{diff}}(c\bar{c})$
<i>flat quark+gluon</i> ($R_q = 0.46$)	$0.113 \pm 0.043 \mu\text{b}$	$0.43 \pm 0.16 \mu\text{b}$	$0.117 \pm 0.044 \mu\text{b}$	$0.41 \pm 0.16 \mu\text{b}$
<i>soft quark</i> ($R_q = 1$)	$0.126 \pm 0.047 \mu\text{b}$	$0.71 \pm 0.27 \mu\text{b}$	$0.091 \pm 0.035 \mu\text{b}$	$0.30 \pm 0.11 \mu\text{b}$
<i>soft gluon</i> ($R_q = 0$)	$0.147 \pm 0.055 \mu\text{b}$	$0.67 \pm 0.25 \mu\text{b}$	$0.121 \pm 0.046 \mu\text{b}$	$0.43 \pm 0.16 \mu\text{b}$
<i>flat quark</i> ($R_q = 1$)	$0.100 \pm 0.038 \mu\text{b}$	$0.38 \pm 0.14 \mu\text{b}$	$0.105 \pm 0.040 \mu\text{b}$	$0.37 \pm 0.14 \mu\text{b}$
<i>flat gluon</i> ($R_q = 0$)	$0.122 \pm 0.046 \mu\text{b}$	$0.47 \pm 0.18 \mu\text{b}$	$0.12 \pm 0.046 \mu\text{b}$	$0.43 \pm 0.16 \mu\text{b}$
<i>hard quark</i> ($R_q = 1$)	$0.100 \pm 0.037 \mu\text{b}$	$0.38 \pm 0.14 \mu\text{b}$	$0.121 \pm 0.040 \mu\text{b}$	$0.37 \pm 0.14 \mu\text{b}$
<i>hard gluon</i> ($R_q = 0$)	$0.125 \pm 0.047 \mu\text{b}$	$0.49 \pm 0.18 \mu\text{b}$	$0.116 \pm 0.046 \mu\text{b}$	$0.43 \pm 0.16 \mu\text{b}$

Table 4.6: Same total diffractive charm and D^* cross sections as those shown in Table 4.5 with the coherence condition increase to $x_F > 0.90$. Errors are statistical only.

Chapter 5

Conclusion

Analyzing 4.72 billion events comprising 87% of the entire E690 data sample, we have found 169 ± 32 events of the single diffractive dissociative reaction:

$$pp \rightarrow p(D^{*-} \rightarrow (\bar{D}^0 \rightarrow K^+ \pi^-) \pi^-) X. \quad (5.1)$$

For 4.01 billion events or 74% of the entire E690 data sample, we have found 44 ± 11 events of the single diffractive dissociative reaction:

$$pp \rightarrow p(D^{*+} \rightarrow (D^0 \rightarrow K^- \pi^+) \pi^+) X. \quad (5.2)$$

Based on these results, the total pp single diffractive D^* cross sections at $\sqrt{s}=40$ GeV were found to be $\sigma_{\text{diff}}(D^{*-}) = [0.196 \pm .043(\text{stat})_{-.046}^{+.014}(\text{syst})] \mu\text{b}$ from events of reaction 5.1 and $\sigma_{\text{diff}}(D^{*+}) = [0.209 \pm .050(\text{stat})_{-.040}^{+.083}(\text{syst})] \mu\text{b}$ from events of reaction 5.2. Using the POMPYT (*flat quark+gluon* model) values of $\frac{\sigma_{\text{diff}}(D^{*-})}{\sigma_{\text{diff}}(c\bar{c})} = 28.6\%$ and $\frac{\sigma_{\text{diff}}(D^{*+})}{\sigma_{\text{diff}}(c\bar{c})} = 26.7\%$, yielded total single diffractive charm cross sections of $\sigma_{\text{diff}}(c\bar{c}) = [0.69 \pm 0.15(\text{stat})_{-.21}^{+.04}(\text{syst})] \mu\text{b}$ and $\sigma_{\text{diff}}(c\bar{c}) = [0.78 \pm 0.19(\text{stat})_{-.17}^{+.49}(\text{syst})] \mu\text{b}$ from events of the two respective reactions.

5.1 Comparison with Theoretical Predictions

To compare these results with theoretical predictions based on the model of Ingelman and Schlein, the cross sections were calculated using the POMPYT Monte Carlo event generator discussed in the previous chapter. POMPYT calculates the diffractive charm cross sections using Equation 1.23 assuming only the leading order flavor creation subprocesses $gg \rightarrow c\bar{c}$ and $q\bar{q} \rightarrow c\bar{c}$. For these calculations, it is assumed that pomerons consist of a mixture of gluons and light quarks (u and d). Furthermore, the momentum sum rule is assumed to hold. In other words, the pomeron's momentum is entirely taken up by its partonic constituents. In Figure 5.1, these calculated cross sections are plotted as a function of R_g , the gluon fraction in the pomeron (Equation 4.11), for the soft, flat, and hard parton distribution functions of Equations 4.12-4.14. The flux factor used in these predictions was the standard Donnachie-Landshoff form of Equation 4.9. The coherence condition of $x_F > 0.85$ for the scattered beam proton was also imposed. The two experimental results from E690 are shown as horizontal lines in Figure 5.1. These lines represent the E690 measurements including statistical errors. As discussed in Section 1.3, the CDF collaboration determined the gluon fraction to be $R_g = 0.54^{+0.16}_{-0.14}$ [22]. At this value of the gluon fraction, POMPYT predicts D^{*-} cross sections of $\sigma_{\text{diff}}(D^{*-}) = 0.22\mu\text{b}$, $0.46\mu\text{b}$, and $0.54\mu\text{b}$ and D^{*+} cross sections of $\sigma_{\text{diff}}(D^{*+}) = 0.17\mu\text{b}$, $0.43\mu\text{b}$, and $0.50\mu\text{b}$ for the soft, flat and hard distribution functions, respectively. From the figure, the POMPYT predictions using the soft distribution function seem consistent with both E690 measurements. One must bear in mind, however, that the HERA results favor a flat Pomeron structure function [18, 19]. The POMPYT predictions with the flat distribution at $R_g = 0.54$ are a factor of $\simeq 2$ higher than the E690 measurements.

In trying to interpret these results, two additional things must be pointed out. First is the fact that POMPYT uses PYTHIA to calculate charm cross sections and PYTHIA takes into account only leading order flavor creation contributions. Mainly because of this fact, the PYTHIA total charm cross section of $15.24\mu\text{b}$ is about a factor of 2-3 times lower than the experimentally determined

5.1. COMPARISON WITH THEORETICAL PREDICTIONS

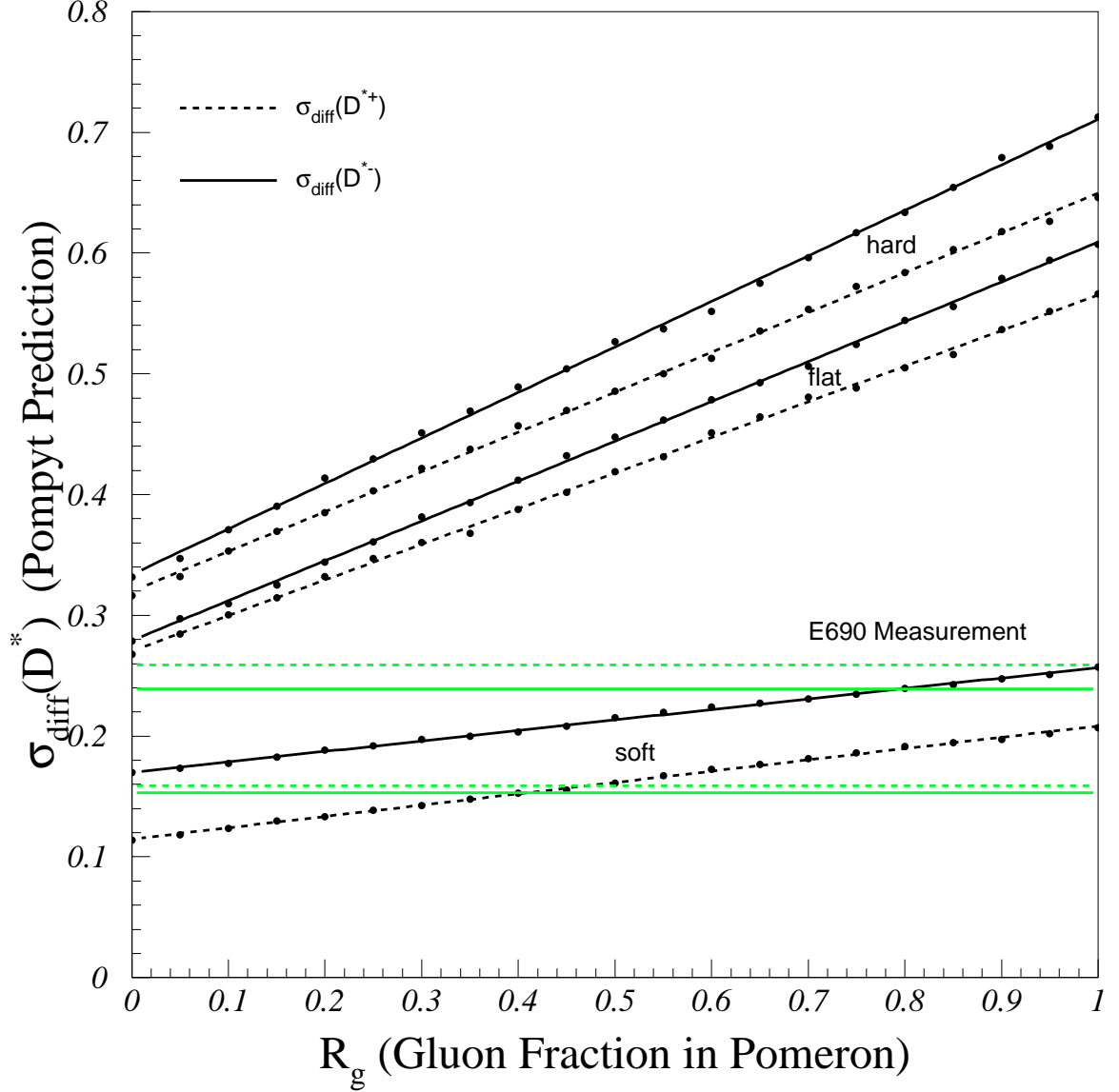


Figure 5.1: Total pp single diffractive D^* cross sections in μb at $\sqrt{s} = 40$ GeV predicted by POMPYPY plotted as a function of R_g , the gluon fraction in the pomeron. Predicted cross sections are shown for the soft, flat, and hard parton distribution functions of Equations 4.12-4.14. The solid horizontal lines represent the E690 results from events of Reaction 5.1 and the dashed horizontal lines represent the results from events of Reaction 5.2.

cross sections. If it is assumed that neglecting higher order contributions has the same effect on the calculated diffractive cross sections as it does for the total cross section, then the POMPYT results in Figure 5.1 may need to be increased by a factor of about 2-3. The second point is that our experimentally determined cross sections are for the total charm produced in association with a leading proton having $x_F > 0.85$. In other words, no distinction is made as to what fraction of these cross sections are due, separately, to diffractive and non-diffractive mechanisms. Since POMPYT accounts only for the diffractive contribution, the non-diffractive background may need to be determined from PYTHIA (see next section) and added to the POMPYT predictions.

5.2 Comparison with Other Experiments

5.2.1 Comparison with CDF and ZEUS

For further comparisons of our results with predictions from the pomeron model of Ingelman and Schlein and with the diffractive hard scattering results from ZEUS and CDF, we calculate a discrepancy factor, D , which is a measure of the deviation of the experimental from the predicted result. We calculate D based on two different definitions as follows.

D According to Definition 1

In the first method, we define D as:

$$D = \frac{\sigma_{\text{diff}}^{\text{exp}}(c\bar{c})}{\sigma_{\text{diff}}^{\text{MC}}(c\bar{c})} \quad (5.3)$$

where $\sigma_{\text{diff}}^{\text{exp}}(c\bar{c})$ is our experimentally determined cross section and $\sigma_{\text{diff}}^{\text{MC}}(c\bar{c})$ is the Monte Carlo predicted cross section. Both quantities are defined as the cross section for the total charm produced with a leading proton having $x_F > 0.85$. They represent sums of the diffractive and non-diffractive contributions for $x_F > 0.85$. For the experimental result, it is implicitly assumed that the acceptances calculated in Section 4.2.2 are identical for both contributions.

5.2. COMPARISON WITH OTHER EXPERIMENTS

The Monte Carlo prediction is calculated as follows:

$$\sigma_{\text{diff}}^{MC}(c\bar{c}) = \sigma_{\text{Pom}}(c\bar{c}) + \sigma_{\text{Pyt}}^{bkg}(c\bar{c}) \quad (5.4)$$

where $\sigma_{\text{Pom}}(c\bar{c})$ is the diffractive contribution predicted by POMPYYT and $\sigma_{\text{Pyt}}^{bkg}(c\bar{c})$ is the non-diffractive background predicted by PYTHIA. The POMPYYT prediction, $\sigma_{\text{diff}}^{MC}(c\bar{c})$, is calculated as a function of R_g , the gluon fraction in the pomeron, according to:

$$\sigma_{\text{Pom}}(c\bar{c}) = (1 - R_g) \times \sigma_{\text{Pom}}^{HQ}(c\bar{c}) + R_g \times \sigma_{\text{Pom}}^{HG}(c\bar{c}) \quad (5.5)$$

where $\sigma_{\text{Pom}}^{HQ}(c\bar{c})$ and $\sigma_{\text{Pom}}^{HG}(c\bar{c})$ are, respectively, the POMPYYT predictions using a hard quark ($R_g = 0$) and hard gluon ($R_g = 1$) structure function for the pomeron. We use the hard structure function (Equation 4.14) in these comparisons since this is what the ZEUS and CDF collaborations used to calculate D . With over 1.8 million events generated for each structure function, POMPYYT predicts $\sigma_{\text{Pom}}^{HQ}(c\bar{c}) = (1.1312 \pm 0.0008) \mu\text{b}$ and $\sigma_{\text{Pom}}^{HG}(c\bar{c}) = (2.488 \pm 0.002) \mu\text{b}$.

The non-diffractive contribution is determined by generating 1 million $c\bar{c}$ events using PYTHIA with default settings for all parameters (see Appendix C) and counting the number having a leading proton with $x_F > 0.85$. Figure 5.2 shows the x_F distribution of final state leading protons from $pp \rightarrow c\bar{c}X$ events generated by PYTHIA at the E690 c.m. energy of $\sqrt{s} \simeq 40$ GeV. From this figure, the fraction of all events generated by PYTHIA with a leading proton having $x_F > 0.85$ is $\simeq 2 \times 0.8797\%$ with a factor of 2 included to account for both x_F hemispheres. Since the total charm cross section predicted by PYTHIA is $15.24 \mu\text{b}$, the non-diffractive contribution is $\sigma_{\text{Pyt}}^{bkg}(c\bar{c}) = 0.27 \mu\text{b}$.

We also calculate $\sigma_{\text{diff}}^{exp}(c\bar{c})$ as a function of the gluon fraction in the pomeron, according to:

$$\sigma_{\text{diff}}^{exp}(c\bar{c}) = (1 - R_g) \times \sigma_{\text{diff}}^{AHQ}(c\bar{c}) + R_g \times \sigma_{\text{diff}}^{AHG}(c\bar{c}) \quad (5.6)$$

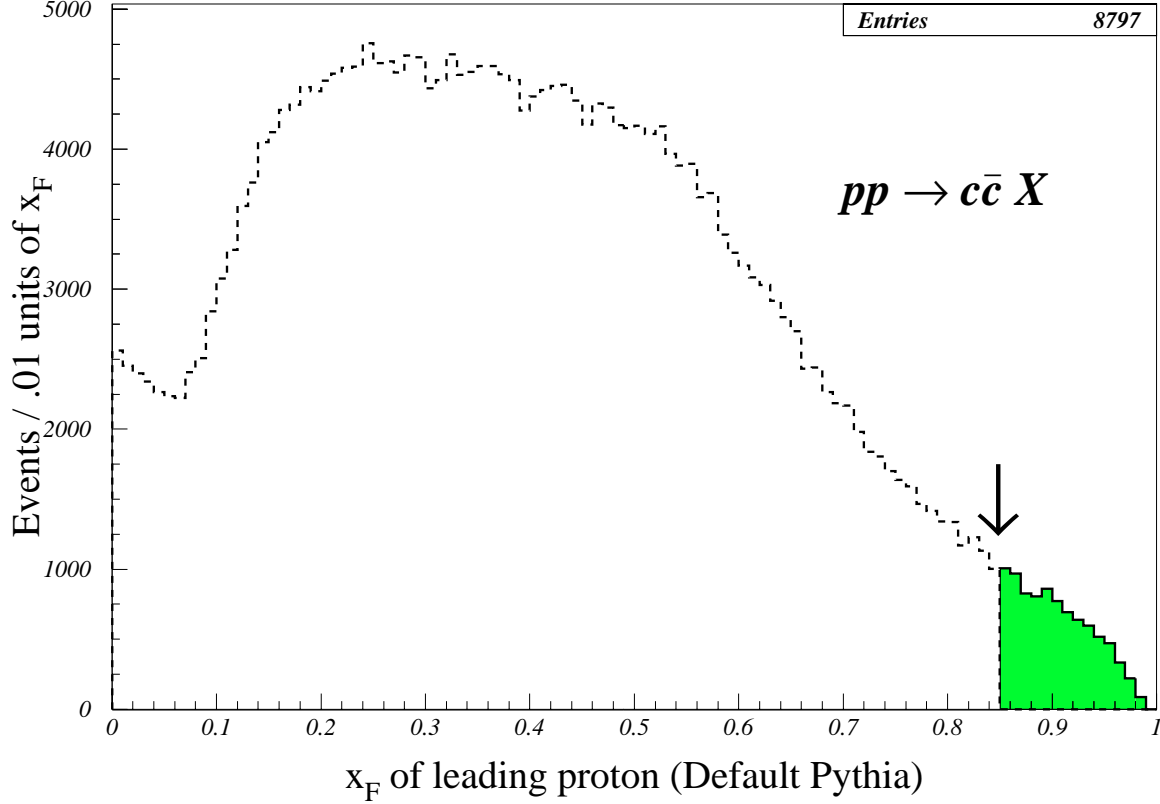


Figure 5.2: x_F distribution of leading protons from 1 million charm events generated by PYTHIA at $\sqrt{s} \simeq 40$ GeV using default values for all parameters. 8,797 events have a leading proton with $x_F > 0.85$.

where $\sigma_{\text{diff}}^{AHQ}(c\bar{c})$ and $\sigma_{\text{diff}}^{AHG}(c\bar{c})$ are our measured results with the acceptances calculated using POMPYT with hard-quark ($R_g = 0$) and hard-gluon ($R_g = 1$) structure functions, respectively. From Table 4.5, the values for these quantities are $\sigma_{\text{diff}}^{AHQ}(c\bar{c}) = (0.61 \pm 0.13) \mu\text{b}$ and $\sigma_{\text{diff}}^{AHG}(c\bar{c}) = (0.71 \pm 0.14) \mu\text{b}$ for events of reaction 5.1 and $\sigma_{\text{diff}}^{AHQ}(c\bar{c}) = (0.61 \pm 0.14) \mu\text{b}$ and $\sigma_{\text{diff}}^{AHG}(c\bar{c}) = (0.91 \pm 0.20) \mu\text{b}$ for events of reaction 5.2.

Figure 5.3 shows our results for D as a function of the gluon fraction in the pomeron. Superimposed on the E690 results in this figure are the ZEUS and CDF curves taken from Reference [22]. For the E690 curves, the solid lines represent the measurements including errors using events of reaction 5.1 and the dashed lines for those of reaction 5.2. For a pomeron gluon fraction of $R_g = 0.54$, the E690 measurements yield $D = 0.310 \pm 0.064$ from events of Reaction 5.1 and $D = 0.362 \pm 0.080$

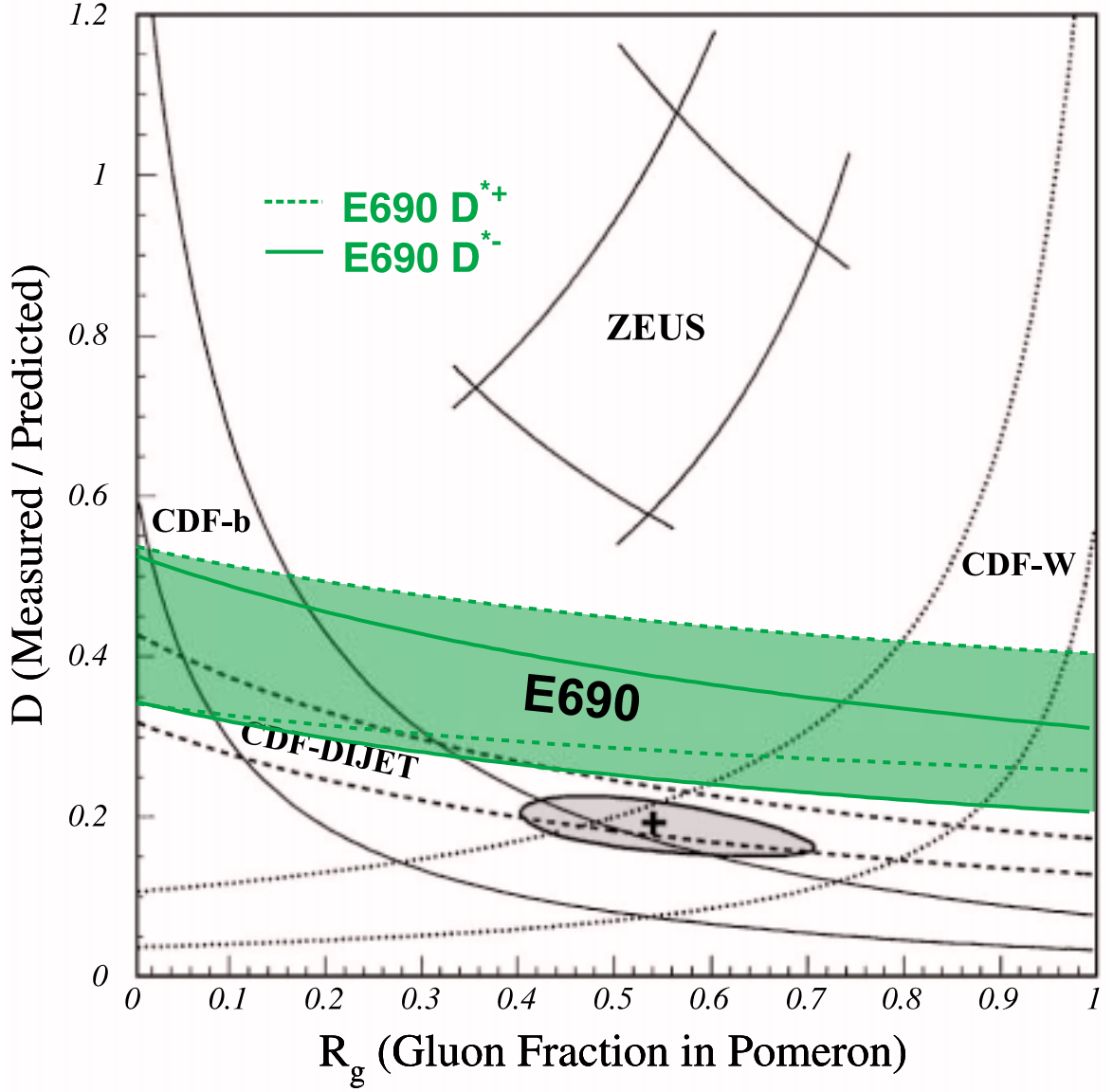


Figure 5.3: Discrepancy factor (D) defined according to Equation 5.3 as a function of the gluon fraction in the pomeron (R_g). Solid E690 curves are from events of Reaction 5.1 and dashed curves from events of Reaction 5.2. Both sets of curves include only statistical errors. Superimposed on the E690 results are the CDF and ZEUS plots from Reference [22].

CHAPTER 5. CONCLUSION

from events of Reaction 5.2. The DIS and photoproduction data from ZEUS yield $0.5 < D < 1.1$ and $0.35 < R_g < 0.7$ [19] while the CDF W -boson, dijet, and b -quark results yield $D = 0.19 \pm 0.04$ and $R_g = 0.54_{-0.14}^{+0.16}$ [22]. The E690 results are about a factor of 2 smaller than the ZEUS results and a factor of 2 larger than the CDF results.

D According to Definition 2

As pointed out in Section 5.1, POMPYT and PYTHIA include only leading order processes in calculating charm cross sections resulting in predicted cross sections that may be lower than what they would be with higher order contributions included. This means that the discrepancy factor, D , calculated in the previous section may be higher than it should be.

To circumvent this issue, we calculate the discrepancy factor according to a second definition:

$$D = \frac{R_{c\bar{c}}^{exp}}{R_{c\bar{c}}^{MC}} \quad (5.7)$$

where $R_{c\bar{c}}^{exp}$ and $R_{c\bar{c}}^{MC}$ are the measured and predicted values of the diffractive to total charm production ratios. The experimental value is calculated as a function of the gluon fraction in the pomeron, R_g , according to:

$$R_{c\bar{c}}^{exp} = \frac{\sigma_{\text{diff}}^{exp}(c\bar{c})}{\sigma_{\text{tot}}^{exp}(c\bar{c})} = \frac{(1 - R_g)\sigma_{\text{diff}}^{AHQ}(c\bar{c}) + R_g\sigma_{\text{diff}}^{AHG}(c\bar{c})}{\sigma_{\text{tot}}^{exp}(c\bar{c})} \quad (5.8)$$

where $\sigma_{\text{diff}}^{AHQ}(c\bar{c})$ and $\sigma_{\text{diff}}^{AHG}(c\bar{c})$ are as defined in Equation 5.6. The experimental value of the total charm cross section, $\sigma_{\text{tot}}^{exp}(c\bar{c})$, is determined using published results tabulated in Reference [71]. Taking the weighted mean of the E653 [72] and E743 (LEBC-MPS) [73] results for $\sigma(D\bar{D})$, we find $\sigma(D\bar{D}) = [28 \pm 5(\text{stat})] \mu\text{b}$. Multiplying this by $\simeq 1.5$ to account for Λ_c and D_s production [71], the total pp charm cross section at 800 GeV/c is $\sigma_{\text{tot}}^{exp}(c\bar{c}) \simeq [42 \pm 7.6(\text{stat})] \mu\text{b}$.

5.2. COMPARISON WITH OTHER EXPERIMENTS

The predicted value of the diffractive to total charm production ratio is calculated as a function of R_g as follows:

$$R_{c\bar{c}}^{MC} = \frac{\sigma_{\text{Pom}}(c\bar{c}) + \sigma_{\text{Pyt}}^{bk g}(c\bar{c})}{\sigma_{\text{Pom}}(c\bar{c}) + \sigma_{\text{Pyt}}^{\text{tot}}(c\bar{c})} \quad (5.9)$$

with $\sigma_{\text{Pom}}(c\bar{c})$ and $\sigma_{\text{Pyt}}^{bk g}(c\bar{c})$ as defined in Equations 5.4 and 5.5. $\sigma_{\text{Pyt}}^{\text{tot}}(c\bar{c})$ is the total charm cross section of $15.24 \mu\text{b}$ determined from 1 million Monte Carlo events generated with PYTHIA using default parameter settings (see Appendix C).

Figure 5.4 shows D calculated according to this second definition as a function of the gluon fraction in the pomeron. As in Figure 5.3, the CDF and ZEUS curves from Reference [22] are shown superimposed on the E690 results. For the E690 curves, the solid lines represent the measurements including errors using events of reaction 5.1 and the dashed lines for those of reaction 5.2. For a pomeron gluon fraction of $R_g = 0.54$, the E690 measurements yield $D = 0.128 \pm 0.035$ from events of Reaction 5.1 and $D = 0.149 \pm 0.043$ from events of Reaction 5.2. These results appear to lie right on top of the CDF diffractive b -quark and W curves and are about a factor of 6 lower than the ZEUS results.

5.2.2 Comparison with Other Charm Experiments

The E690 cross sections are consistent with the upper limit of $\sigma_{\text{diff}}(c\bar{c}) < 26 \mu\text{b}/\text{Si nucleus}$ at $\sqrt{s} = 40$ GeV set by FNAL E653 in 1993 [38]. As mentioned in Section 1.5, this upper limit is equivalent to $\sigma_{\text{diff}}(c\bar{c}) < 2.8 \mu\text{b}$ and $\sigma_{\text{diff}}(c\bar{c}) < 0.93 \mu\text{b}$ in the pp case if the cross section is assumed to scale with atomic weight as $A^{2/3}$ and A , respectively. The total diffractive charm cross sections measured by E690 lie below these limits and hence beyond the sensitivity of E653.

Among the CERN ISR experiments mentioned in Section 1.5, that of Giboni and collaborators [41] claimed measuring the diffractive cross section for the reaction $pp \rightarrow p(\Lambda_c^+ \rightarrow pK^- \pi^+)X$. For the x_F of the Λ_c^+ ranging from 0.3 to 0.8, they reported a cross section of $0.7 \mu\text{b} < \sigma B < 1.8 \mu\text{b}$ where B represents the branching ratio for the decay process $\Lambda_c^+ \rightarrow pK^- \pi^+$. Taking the average of

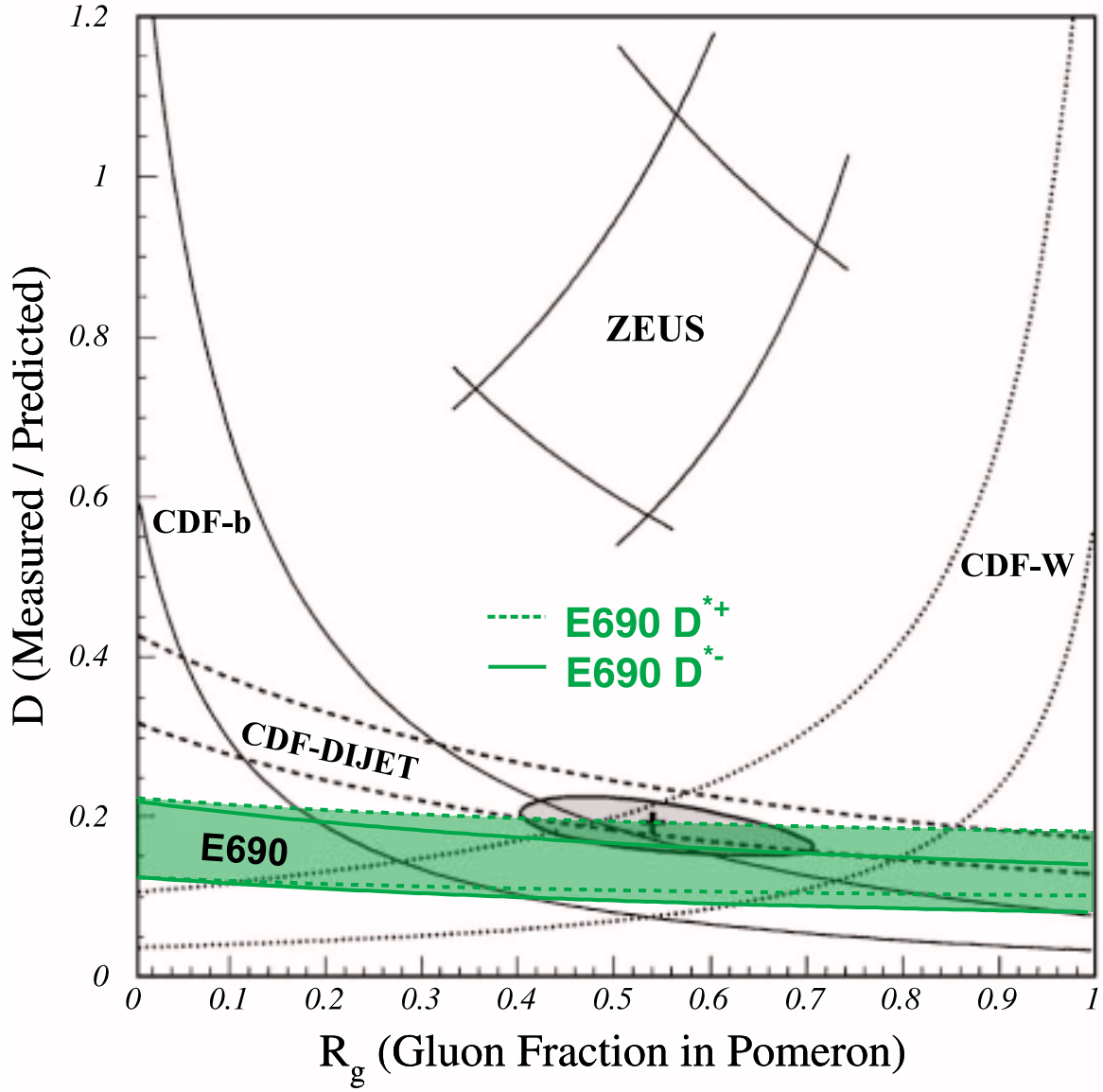


Figure 5.4: Discrepancy factor (D) defined according to Equation 5.7 as a function of the gluon fraction in the pomeron (R_g). Solid E690 curves are from events of Reaction 5.1 and dashed curves from events of Reaction 5.2. Both sets of curves include only statistical errors. Superimposed on the E690 results are the CDF and ZEUS plots from Reference [22].

5.2. COMPARISON WITH OTHER EXPERIMENTS

$\sigma B = 1.25 \mu\text{b}$ and using a branching ratio of $B = 5.0\%$ [58] for this decay process gives $\sigma = 25 \mu\text{b}$ for $0.3 < x_F < 0.8$. Further assuming a flat x_F distribution for the Λ_c^+ results in $\sigma = 50 \mu\text{b}$ for the entire x_F range from 0 to 1. These results were for $\sqrt{s} = 63 \text{ GeV}$ and $M_X^2/s < 0.2$. To compare these results with the E690 measurements for $\sqrt{s} = 40 \text{ GeV}$ and which satisfy the coherence condition $(M_X^2 - M_p^2)/s < 0.15$, we assume that $d\sigma/dM_X^2 \propto 1/M_X^2$ and integrate from a lower limit corresponding to the charm threshold of $M_c^2 \simeq (5 \text{ GeV}/c^2)^2$ to an upper limit of $M_{X,\text{hi}}^2$:

$$\sigma = \int_{M_{X,\text{lo}}^2}^{M_{X,\text{hi}}^2} \frac{d\sigma}{dM_X^2} dM_X^2 = \int_{M_c^2}^{M_{X,\text{hi}}^2} \frac{C}{M_X^2} dM_X^2 = C \times \ln \left(\frac{M_{X,\text{hi}}^2}{M_c^2} \right).$$

The CERN ISR result corresponding to the E690 energy of $\sqrt{s} = 40 \text{ GeV}$ and upper M_X^2 limit of $M_X^2 < M_p^2 + 0.15s$ can therefore be written as:

$$\begin{aligned} \sigma_{40}(M_{X,\text{hi}}^2 = M_p^2 + 0.15s) &= \frac{\ln \left(\frac{1+0.15(40)^2}{25} \right)}{\ln \left(\frac{0.2(63)^2}{25} \right)} \times 50 \mu\text{b} \\ &= 33 \mu\text{b}. \end{aligned}$$

If we assume that the Λ_c^+ accounts for $\simeq 20\%$ of the total pp charm cross section [71], then the CERN ISR result translates to a total pp single diffractive charm cross section of $\sigma_{\text{diff}}(c\bar{c}) \simeq 165 \mu\text{b}$ which is over two orders of magnitude greater than the E690 measurements.

Finally, to get an idea of the diffractive to total charm production ratio, we compare our measurements with those from other fixed target charm experiments tabulated in Reference [71]. As discussed in the previous section, the weighted mean of the E653 [72] and E743 (LEBC-MPS) [73] results for $\sigma(D\bar{D})$ is $\sigma(D\bar{D}) = [28 \pm 5(\text{stat})] \mu\text{b}$. Multiplying by $\simeq 1.5$ for Λ_c and D_s production [71] gives $\sigma_{\text{tot}}(c\bar{c}) \simeq [42 \pm 7(\text{stat})] \mu\text{b}$ for the total pp charm cross section at 800 GeV/c. Dividing our results by this value, we find $R_{c\bar{c}} = (1.7 \pm 0.5)\%$ and $R_{c\bar{c}} = (1.9 \pm 0.6)\%$ for the diffractive cross sections determined using events of Reactions 5.1 and 5.2 respectively.

5.3 Conclusions

The Ingelman-Schlein model described in Section 1.3.1 assumes that all diffractive interactions between two particles can be described with the two-step process involving (1) the emission of a pomeron from the diffracted particle and (2) the interaction of the pomeron with the second particle. All that one needs to know is the pomeron emission probability from the diffracted particle and the interaction cross section between the pomeron and the second particle. In this model, the pomeron is a QCD object with a partonic structure that is universal and independent of the emission process and the interaction involved. Knowledge of its structure should allow one to calculate the cross section for any diffractive process using QCD.

However, as mentioned in Section 1.3.3, predictions from this model using structure functions extracted from DIS at HERA are significantly higher than the measured pp cross sections at the Tevatron. This was interpreted as a breakdown of factorization in the Ingelman-Schlein picture of diffraction. Figures 5.3 and 5.4 show that our results for D are a factor of $\simeq 2 - 6$ times smaller than the ZEUS results at HERA. These results provide further evidence to support the view that the pomeron does not seem to have a universal nature that is independent of the process involved.

In conclusion, the E690 results constitute the first observation of diffractively produced charm in hadron-hadron interactions. Roughly $\simeq 2\%$ of the total pp charm cross section at $\sqrt{s} = 40$ GeV can be attributed to diffractive production. The measured diffractive cross section is significantly less than predictions based on the pomeron model of Ingelman and Schlein using a flat or a hard structure function for the pomeron.

Appendix A

The E690 Collaboration

M.H.L.S. Wang^{1†}, M.C. Berisso¹, D.C. Christian²,
J. Félix³, A. Gara^{4‡}, E. Gottschalk^{4§}, G. Gutiérrez²,
E.P. Hartouni^{1†}, B.C. Knapp⁴, M.N. Kreisler^{1†}, S. Lee^{1¶},
K. Markianos^{1*}, G. Moreno³, M.A. Reyes^{3**}, M. Sosa³,
A. Wehmann², D. Wesson^{1***}
(E690 Collaboration)

¹*University of Massachusetts, Amherst, Massachusetts 01003*

²*Fermilab, Batavia, Illinois 60510*

³*Universidad de Guanajuato, León, Guanajuato, México*

⁴*Columbia University, Nevis Laboratories, Irvington, New York 10533*

[†] Present address: LLNL, Livermore, CA 94551.

[‡] Present address: IBM Corp., Yorktown Heights, NY, 10598.

[§] Present address: Fermilab, Batavia, IL, 60510.

[¶] Present address: Cognex Corp., Natick, MA, 01760.

* Present address: U. of Washington, Seattle, WA, 98109.

** Present address: U. Michoacana, Morelia, Mexico.

*** Present address: OAO Corp., Athens, GA, 30605.

APPENDIX A. THE E690 COLLABORATION

Appendix B

POMPYT Parameter Settings

```
-----
POMGEN setup file
NEVGL: number of events to generate.....500000
NEVGMOD: modulus for event gen. tally...10000
NDUMP: number of events to dump.....10
NTOMC: output tape number.....4000
NTOL: number of output tapes.....1
-----
RANDOM NUMBERS (ISEQ: =<-2,-1,>=0 | use default, restore, select sequence)
ISEQG: 1-215 (period ~10^09) for grndm..1
ISEQP: 0-9e8 (period ~10^43) for rlu....119780503
-----
CCBAR setup file (X=Unspecified)
ICHARM(1,1): first charm particle.....413
ICHARM(2,1): second charm particle.....X
IRDCY(1): 1st charm part decay mode.....4
IRDCY(2): 2nd charm part decay mode.....X
-----
POMPAR pompyt switches and parameters (X=Default)
MPOM(1): pomeron flux factor.....3
MPOM(2): pom. parton dens. function.....9
PARPOM(1): pom. total cross section.....X
PARPOM(2): power in 1/(x_pom)^p.....X
PARPOM(3): coeff. a1 in exp t dep.....X
PARPOM(4): coeff. a2 in exp t dep.....X
PARPOM(5): coeff. a3 in exp t dep.....X
PARPOM(6): slope b1 in exp t dep.....X
PARPOM(7): slope b2 in exp t dep.....X
PARPOM(8): slope b3 in exp t dep.....X
PARPOM(9): C in flux factor 2.....X
PARPOM(10): A in flux factors 2 & 3.....X
PARPOM(11): B in flux factors 2 & 3.....X
PARPOM(12): beta_0^2 in flux factor 3...X
PARPOM(13): epsilon in flux factor 3....0.115
PARPOM(14): alpha' in flux factor 3....0.26
PARPOM(21): power 'a' in soft gluon pdf.X
```

APPENDIX B. POMPYT PARAMETER SETTINGS

PARPOM(22): power a in MPOM(2)=7,8 pdf..X
 PARPOM(23): power b in MPOM(2)=7,8 pdf..X
 PARPOM(24): power a in MPOM(2)=9 pdf....0.
 PARPOM(25): power b in MPOM(2)=9 pdf....0.
 PARPOM(26): power c in MPOM(2)=9 pdf....0.
 PARPOM(27): power d in MPOM(2)=9 pdf....0.
 PARPOM(28): a for quark when MPOM(2)=10.X
 PARPOM(29): b for gluon when MPOM(2)=10.X
 PARPOM(30): quark fraction Rq.....0.46

 POMCUT pompyt limits for diffractive variables (X=Default)
 UCUT(1): x_F lower limit.....0.85
 UCUT(2): x_F upper limit.....X
 UCUT(3): Mx lower limit.....4.81767
 UCUT(4): Mx upper limit.....X
 UCUT(5): t lower limit.....X
 UCUT(6): t upper limit.....X
 UCUT(7): p_T lower limit (p_fast).....X
 UCUT(8): p_T upper limit (p_fast).....X

```

*****
*
*           POMPYT version 2.6 (date: 12-SEP-1996)
*
*   A Monte Carlo based on PYTHIA 5.7 to simulate
*   diffractive hard scattering processes through
*   pomeron (pion) exchange in pp(bar), ep, gammap
*
*   Authors: Paolo Bruni, brunipa@vxdesy.desy.de
*            Anders Edin, edin@tsl.uu.se
*            and Gunnar Ingelman, ingelman@desy.de
*
*   WWW: http://www3.tsl.uu.se/thep/pompyt/
*
*****
  
```

JETSET version 7.410 is used.
 PYTHIA version 5.724 is used.

```

*****
*   pomeron -exchange: p      + p      ---> p      + p+      + X      *
*****
  
```

```

*      User limits on diffractive variables      *
*****
*              MIN              MAX              *
*****
* xF          * 0.850000      * 0.999900      *
* MX (GeV)    * 4.81767      * 0.100000E+09 *
* t (GeV**2) * -10.0000      * 0.000000E+00 *
* pT (GeV)    * 0.000000E+00 * 10.0000      *
*****

*      Effective limits on diffractive variables *
*****
*              MIN              MAX              *
*****
* xF          * 0.850000      * 0.978458      *
* MX (GeV)    * 4.81767      * 15.0349      *
* t (GeV**2) * -10.0000      * -.197713E-03 *
* pT (GeV)    * 0.000000E+00 * 3.12797      *
*****

```

Parameter values:

I	MPOM(I)	PARPOM(I)	PARPOM(I+10)	PARPOM(I+20)
1	3	2.300	0.7000	5.000
2	9	1.000	3.240	1.000
3	1	3.190	0.1150	1.000
4	1	0.2120	0.2600	0.0000E+00
5	1	0.0000E+00	0.0000E+00	0.0000E+00
6	2	8.000	0.0000E+00	0.0000E+00
7	0	3.000	0.0000E+00	0.0000E+00
8	0	0.0000E+00	0.0000E+00	1.000
9	0	3.400	0.0000E+00	1.000
10	0	2.800	1.000	0.4600

```

*      SUMMARY of SIMULATION      *
*****
* Global CMS energy (GeV)          * 38.7691      *
* Min pT in hard scat. (GeV)      * 0.000000E+00 *
* Min Q2 in DIS (GeV**2)          * 0.000000E+00 *
*****
*      Diffractive Kinematics      *
*****
*              MIN              MAX              *
*****
* xF          * 0.850000      * 0.978458      *
* MX (GeV)    * 4.81767      * 15.0349      *
* t (GeV**2) * -10.0000      * -.197713E-03 *
* pT (GeV)    * 0.000000E+00 * 3.12797      *
* Whad (GeV) * 0.000000E+00 * 0.000000E+00 *
*****

```

APPENDIX B. POMPYT PARAMETER SETTINGS

Pomeron structure function: $0.46*xq(x)+0.54*xg(x)=$
 $0.46N1*x^{0.00}*(1.-x)^{0.00}+0.54N2*x^{0.00}*(1.-x)^{0.00}$

Coefficients N1 and N2:
 $N1 = (0.00+0.00+1.)!\(0.00!0.00!$
 $N2 = ($
Pomeron/pion flux MPOM(1)= 3 :
Form factor t-dependence: $(4m^{*2}- 2.80t)/(4m^{*2}-t)*1/(1-t/ 0.70)^{*2}$

Parameter values:

I	MPOM(I)	PARPOM(I)	PARPOM(I+10)	PARPOM(I+20)
1	3	2.300	0.7000	5.000
2	9	1.000	3.240	1.000
3	1	3.190	0.1150	1.000
4	1	0.2120	0.2600	0.0000E+00
5	1	0.0000E+00	0.0000E+00	0.0000E+00
6	2	8.000	0.0000E+00	0.0000E+00
7	0	3.000	0.0000E+00	0.0000E+00
8	0	0.0000E+00	0.0000E+00	1.000
9	0	3.400	0.0000E+00	1.000
10	0	2.800	1.000	0.4600

Pomeron - proton total cross section = 2.300 mb
Integrated pomeron flux factor = 0.522
Pomeron - p cross section = 1.550E+03 nb
=====> Overall total cross section = 810. nb

1***** PYSTAT: Statistics on Number of Events and Cross-sections *****

I	I	I	I	I
I	Subprocess	I	Number of points	I
I		I		I
I		I		I
I	N:o Type	I	Generated	I
I		I		I
I	0 All included subprocesses	I	1860703	I
I	81 q + q~ -> Q + Q~, massive	I	504269	I
I	82 g + g -> Q + Q~, massive	I	1356434	I
I		I		I

***** Fraction of events that fail fragmentation cuts = 0.11011 *****

1***** PYSTAT: User-Defined Limits on Kinematical Variables *****

```

=====
I                                                                 I
I          2.000E+00 < m_hard (GeV/c^2) < 9.958E+00          I
I    0.000E+00 ( 1.000E+00) < p_T_hard (GeV/c) < 4.979E+00  I
I                                  m_finite (GeV/c^2) = 1.000E+00  I
I          -1.000E+01 < y*_subsystem < 1.000E+01          I
I          -1.000E+01 < y*_large < 1.000E+01              I
I          -1.000E+01 < y*_small < 1.000E+01              I
I          -1.000E+01 < eta*_large < 1.000E+01             I
I          -1.000E+01 < eta*_small < 1.000E+01            I
I          -1.000E+00 < cos(theta*)_large < 1.000E+00      I
I          -1.000E+00 < cos(theta*)_small < 1.000E+00      I
I          0.000E+00 < x_1 < 1.000E+00                     I
I          0.000E+00 < x_2 < 1.000E+00                     I
I          -1.000E+00 < x_F < 1.000E+00                    I
I          -1.000E+00 < cos(theta_hard) < 1.000E+00        I
I          2.000E+00 < m'_hard (GeV/c^2) < 9.958E+00        I
I                                                                 I
=====

```

1***** PYSTAT: Summary of Status Codes and Parameter Values *****

I	MSTP(I)	PARP(I)	I	MSTP(I)	PARP(I)
1	3	1.900E-01	101	3	5.000E-01
2	1	4.818E+00	102	1	2.800E-01
3	2	0.000E+00	103	0	1.000E+00
4	0	0.000E+00	104	0	8.000E-01
5	0	0.000E+00	105	0	0.000E+00
6	0	0.000E+00	106	0	0.000E+00
7	4	0.000E+00	107	0	0.000E+00
8	0	0.000E+00	108	0	0.000E+00
9	0	0.000E+00	109	0	0.000E+00
10	0	0.000E+00	110	0	0.000E+00
11	1	0.000E+00	111	1	2.000E+00
12	0	0.000E+00	112	1	0.000E+00
13	1	1.000E+00	113	1	0.000E+00
14	0	1.000E-02	114	0	0.000E+00
15	5	6.000E-01	115	0	0.000E+00
16	0	1.000E+00	116	0	0.000E+00
17	0	1.000E+00	117	0	0.000E+00
18	0	0.000E+00	118	0	0.000E+00
19	0	0.000E+00	119	0	0.000E+00
20	0	0.000E+00	120	0	0.000E+00
21	1	0.000E+00	121	1	5.224E-01
22	0	0.000E+00	122	0	4.000E-01
23	1	0.000E+00	123	2	0.000E+00
24	0	0.000E+00	124	1	0.000E+00
25	0	0.000E+00	125	1	0.000E+00

APPENDIX B. POMPYT PARAMETER SETTINGS

26	0	0.000E+00	126	20	0.000E+00
27	0	0.000E+00	127	0	0.000E+00
28	0	0.000E+00	128	0	0.000E+00
29	0	0.000E+00	129	10	0.000E+00
30	1	0.000E+00	130	0	0.000E+00
31	1	1.500E+00	131	0	1.000E-02
32	2	2.000E+00	132	4	0.000E+00
33	0	7.500E-02	133	0	0.000E+00
34	1	1.000E+00	134	1	0.000E+00
35	0	2.000E-01	135	0	0.000E+00
36	2	0.000E+00	136	0	0.000E+00
37	1	2.000E+00	137	0	0.000E+00
38	5	7.000E-01	138	0	0.000E+00
39	2	6.000E-03	139	0	0.000E+00
40	0	0.000E+00	140	0	0.000E+00
41	1	2.000E-02	141	0	0.000E+00
42	1	2.000E+00	142	0	0.000E+00
43	3	1.000E-01	143	0	0.000E+00
44	7	1.000E+03	144	0	0.000E+00
45	3	2.054E+03	145	0	0.000E+00
46	1	1.230E+02	146	0	0.000E+00
47	1	2.460E+02	147	0	0.000E+00
48	2	0.000E+00	148	0	0.000E+00
49	2	0.000E+00	149	0	0.000E+00
50	0	0.000E+00	150	0	0.000E+00
51	9	1.000E+00	151	0	0.000E+00
52	1	0.000E+00	152	0	0.000E+00
53	1	0.000E+00	153	0	0.000E+00
54	1	0.000E+00	154	0	0.000E+00
55	5	0.000E+00	155	0	0.000E+00
56	1	0.000E+00	156	0	0.000E+00
57	1	0.000E+00	157	0	0.000E+00
58	6	0.000E+00	158	0	0.000E+00
59	1	0.000E+00	159	0	0.000E+00
60	0	0.000E+00	160	0	0.000E+00
61	1	1.900E-01	161	0	2.200E+00
62	3	1.000E+00	162	0	2.360E+01
63	2	2.500E-01	163	0	1.840E+01
64	2	1.000E+00	164	0	1.150E+01
65	1	2.000E+00	165	0	0.000E+00
66	1	1.000E-03	166	0	0.000E+00
67	2	4.000E+00	167	0	0.000E+00
68	0	1.000E-03	168	0	0.000E+00
69	0	0.000E+00	169	0	0.000E+00
70	0	0.000E+00	170	0	0.000E+00
71	1	4.000E+00	171	1	6.623E-01
72	0	1.900E-01	172	2	0.000E+00
73	0	0.000E+00	173	1	5.224E-01
74	0	0.000E+00	174	0	1.000E+00
75	0	0.000E+00	175	0	0.000E+00
76	0	0.000E+00	176	0	0.000E+00

77	0	0.000E+00	177	0	0.000E+00
78	0	0.000E+00	178	0	0.000E+00
79	0	0.000E+00	179	0	0.000E+00
80	0	0.000E+00	180	0	0.000E+00
81	1	1.400E+00	181	5	0.000E+00
82	1	1.550E+00	182	724	0.000E+00
83	100	5.000E-01	183	1997	0.000E+00
84	0	2.000E-01	184	6	0.000E+00
85	0	3.300E-01	185	4	0.000E+00
86	0	6.600E-01	186	408	0.000E+00
87	0	7.000E-01	187	0	0.000E+00
88	0	5.000E-01	188	0	0.000E+00
89	0	0.000E+00	189	0	0.000E+00
90	0	0.000E+00	190	0	0.000E+00
91	1	4.400E-01	191	0	0.000E+00
92	4	2.000E-01	192	0	0.000E+00
93	1	2.000E+00	193	0	0.000E+00
94	2	1.000E+00	194	0	0.000E+00
95	0	0.000E+00	195	0	0.000E+00
96	0	3.000E+00	196	0	0.000E+00
97	0	1.000E+00	197	0	0.000E+00
98	0	7.500E-01	198	0	0.000E+00
99	0	4.400E-01	199	0	0.000E+00
100	0	2.000E+00	200	0	0.000E+00

APPENDIX B. POMPYT PARAMETER SETTINGS

Appendix C

PYTHIA Parameter settings

```
-----  
SCIGEN setup file  
NEVGL: number of events to generate.....1000000  
NEVMOD: modulus for event gen. tally...100000  
NDUMP: number of events to dump.....10  
-----
```

```
EVENT TYPE  
ENCM: c.m. energy .....38.76846  
HAD1: hadron 1 .....p  
HAD2: hadron 2 .....p  
NSUB: what to generate c:1,b:2,W:3 .....1  
-----
```

```
SCI SWITCHES (X=Default)  
MSTP(188): SCI switch .....0  
PARP(188): R parameter .....X  
PARJ(42): b in area law .....X  
MSTP(187): sea quark switch .....X  
PARP(187): width for sea q virt .....X  
MSTP(92): E part. bet. remnants.....X  
PARJ(82): final cascade Q_0 .....X  
PARP(62): initial cascade Q_0 .....X  
CKIN(3): pT cutoff for 2->2 processes...X  
MSTP(81): Multiple interactions.....1  
MSTP(51): parton-distribution set.....X  
MSTP(52): PYTHIA:1 or PDFLIB:2 pdf.....X  
-----
```

APPENDIX C. PYTHIA PARAMETER SETTINGS

1***** PYINIT: initialization of PYTHIA routines *****

```

=====
I
I          PYTHIA will be initialized for a p on p collider
I          at      38.768 GeV center-of-mass energy
I
I
=====

```

***** PYMAXI: summary of differential cross-section maximum search *****

```

=====
I
I  ISUB  Subprocess name
I
I
=====
I
I  81    q + q~ -> Q + Q~, massive
I  82    g + g -> Q + Q~, massive
I  96    Semihard QCD 2 -> 2
I
I
=====

```

***** PYINIT: initialization completed *****

1***** PYSTAT: Statistics on Number of Events and Cross-sections *****

```

=====
I
I          Subprocess
I
I          Number of points
I          Sigma
I          (mb)
I
I  N:o Type
I          Generated      Tried
I
I
=====
I
I  0 All included subprocesses
I  81 q + q~ -> Q + Q~, massive
I  82 g + g -> Q + Q~, massive
I
I
=====

```

***** Fraction of events that fail fragmentation cuts = 0.00002 *****

1***** PYSTAT: User-Defined Limits on Kinematical Variables *****

```

=====
I                                                                 I
I          2.000E+00 < m_hard (GeV/c^2) < 3.877E+01          I
I    0.000E+00 ( 1.000E+00) < p_T_hard (GeV/c) < 1.938E+01  I
I          m_finite (GeV/c^2) = 1.000E+00                    I
I          -1.000E+01 < y*_subsystem < 1.000E+01           I
I          -1.000E+01 < y*_large < 1.000E+01                I
I          -1.000E+01 < y*_small < 1.000E+01                I
I          -1.000E+01 < eta*_large < 1.000E+01              I
I          -1.000E+01 < eta*_small < 1.000E+01              I
I          -1.000E+00 < cos(theta*)_large < 1.000E+00       I
I          -1.000E+00 < cos(theta*)_small < 1.000E+00       I
I          0.000E+00 < x_1 < 1.000E+00                       I
I          0.000E+00 < x_2 < 1.000E+00                       I
I          -1.000E+00 < x_F < 1.000E+00                      I
I          -1.000E+00 < cos(theta_hard) < 1.000E+00         I
I          2.000E+00 < m'_hard (GeV/c^2) < 3.877E+01        I
I                                                                 I
=====

```

1***** PYSTAT: Summary of Status Codes and Parameter Values *****

I	MSTP(I)	PARP(I)	I	MSTP(I)	PARP(I)
1	3	1.900E-01	101	3	5.000E-01
2	1	1.000E+01	102	1	2.800E-01
3	2	0.000E+00	103	0	1.000E+00
4	0	0.000E+00	104	0	8.000E-01
5	0	0.000E+00	105	0	0.000E+00
6	0	0.000E+00	106	0	0.000E+00
7	4	0.000E+00	107	0	0.000E+00
8	0	0.000E+00	108	0	0.000E+00
9	0	0.000E+00	109	0	0.000E+00
10	0	0.000E+00	110	0	0.000E+00
11	1	0.000E+00	111	1	2.000E+00
12	0	0.000E+00	112	1	0.000E+00
13	1	1.000E+00	113	1	0.000E+00
14	0	1.000E-02	114	0	0.000E+00
15	5	6.000E-01	115	0	0.000E+00
16	0	1.000E+00	116	0	0.000E+00
17	0	1.000E+00	117	0	0.000E+00
18	0	0.000E+00	118	0	0.000E+00
19	0	0.000E+00	119	0	0.000E+00
20	0	0.000E+00	120	0	0.000E+00
21	1	0.000E+00	121	0	1.000E+00
22	0	0.000E+00	122	1	4.000E-01
23	1	0.000E+00	123	2	0.000E+00
24	0	0.000E+00	124	1	0.000E+00

APPENDIX C. PYTHIA PARAMETER SETTINGS

25	0	0.000E+00	125	1	0.000E+00
26	0	0.000E+00	126	20	0.000E+00
27	0	0.000E+00	127	0	0.000E+00
28	0	0.000E+00	128	0	0.000E+00
29	0	0.000E+00	129	10	0.000E+00
30	1	0.000E+00	130	0	0.000E+00
31	1	1.500E+00	131	0	1.000E-02
32	2	2.000E+00	132	4	0.000E+00
33	0	7.500E-02	133	0	0.000E+00
34	1	1.000E+00	134	1	0.000E+00
35	0	2.000E-01	135	0	0.000E+00
36	2	0.000E+00	136	0	0.000E+00
37	1	2.000E+00	137	0	0.000E+00
38	5	7.000E-01	138	0	0.000E+00
39	2	6.000E-03	139	0	0.000E+00
40	0	0.000E+00	140	0	0.000E+00
41	1	2.000E-02	141	0	0.000E+00
42	1	2.000E+00	142	0	0.000E+00
43	3	1.000E-01	143	0	0.000E+00
44	7	1.000E+03	144	0	0.000E+00
45	3	2.054E+03	145	0	0.000E+00
46	1	1.230E+02	146	0	0.000E+00
47	1	2.460E+02	147	0	0.000E+00
48	2	0.000E+00	148	0	0.000E+00
49	2	0.000E+00	149	0	0.000E+00
50	0	0.000E+00	150	0	0.000E+00
51	9	1.000E+00	151	0	0.000E+00
52	1	0.000E+00	152	0	0.000E+00
53	1	0.000E+00	153	0	0.000E+00
54	1	0.000E+00	154	0	0.000E+00
55	5	0.000E+00	155	0	0.000E+00
56	1	0.000E+00	156	0	0.000E+00
57	1	0.000E+00	157	0	0.000E+00
58	6	0.000E+00	158	0	0.000E+00
59	1	0.000E+00	159	0	0.000E+00
60	0	0.000E+00	160	0	0.000E+00
61	1	1.900E-01	161	0	2.200E+00
62	3	1.000E+00	162	0	2.360E+01
63	2	2.500E-01	163	0	1.840E+01
64	2	1.000E+00	164	0	1.150E+01
65	1	2.000E+00	165	0	0.000E+00
66	1	1.000E-03	166	0	0.000E+00
67	2	4.000E+00	167	0	0.000E+00
68	0	1.000E-03	168	0	0.000E+00
69	0	0.000E+00	169	0	0.000E+00
70	0	0.000E+00	170	0	0.000E+00
71	1	4.000E+00	171	0	0.000E+00
72	0	1.900E-01	172	2	0.000E+00
73	0	0.000E+00	173	0	0.000E+00
74	0	0.000E+00	174	0	1.000E+00
75	0	0.000E+00	175	0	0.000E+00

76	0	0.000E+00	176	0	0.000E+00
77	0	0.000E+00	177	0	0.000E+00
78	0	0.000E+00	178	0	0.000E+00
79	0	0.000E+00	179	0	0.000E+00
80	0	0.000E+00	180	0	0.000E+00
81	1	1.400E+00	181	5	0.000E+00
82	1	1.550E+00	182	724	0.000E+00
83	100	5.000E-01	183	1997	0.000E+00
84	0	2.000E-01	184	6	0.000E+00
85	0	3.300E-01	185	4	0.000E+00
86	0	6.600E-01	186	408	0.000E+00
87	0	7.000E-01	187	0	0.000E+00
88	0	5.000E-01	188	0	0.000E+00
89	0	0.000E+00	189	0	0.000E+00
90	0	0.000E+00	190	0	0.000E+00
91	1	4.400E-01	191	0	0.000E+00
92	4	2.000E-01	192	0	0.000E+00
93	1	2.000E+00	193	0	0.000E+00
94	2	1.000E+00	194	0	0.000E+00
95	0	0.000E+00	195	0	0.000E+00
96	0	3.000E+00	196	0	0.000E+00
97	0	1.000E+00	197	0	0.000E+00
98	0	7.500E-01	198	0	0.000E+00
99	0	4.400E-01	199	0	0.000E+00
100	0	2.000E+00	200	0	0.000E+00

APPENDIX C. PYTHIA PARAMETER SETTINGS

Bibliography

- [1] G. Ingelman and P. E. Schlein. Jet structure in high mass diffractive scattering. *Phys. Lett.*, B152:256, 1985.
- [2] K. Goulianos. Diffractive interactions of hadrons at high energies. *Phys. Rep.*, 101:169, 1983.
- [3] G. Alberi and G. Goggi. Diffraction of subnuclear waves. *Phys. Rep.*, 74:1, 1981.
- [4] U. Umaldi, M. Jacob, and G. Matthiae. Diffraction of hadronic waves. *Ann. Rev. Nucl. Sci.*, 26:385 (1976).
- [5] J. R. Forshaw and D. A. Ross. *Quantum Chromodynamics and the Pomeron*. Cambridge University Press, 1997.
- [6] P. D. B. Collins and E. J. Squires. *Regge Poles in Particle Physics*. Springer-Verlag, 1968.
- [7] E. J. Squires. *Complex Angular Momenta and Particle Physics*. W. A. Benjamin, Inc., 1964.
- [8] S. C. Frautschi. *Regge Poles and S-Matrix Theory*. W. A. Benjamin, Inc., 1963.
- [9] M. L. Perl. *High Energy Hadron Physics*. John Wiley and Sons, 1974.
- [10] J. Mathews and R. L. Walker. *Mathematical Methods of Physics*. W. A. Benjamin, Inc., 1970.
- [11] A. Sommerfeld. *Partial Differential Equations in Physics*. Academic Press, Inc., 1949.
- [12] A. H. Mueller. *Phys. Rev.*, D2:2963, 1970.
- [13] A. H. Mueller. *Phys. Rev.*, D4:150, 1971.
- [14] F. Low. Model of the bare pomeron. *Phys. Rev.*, D12:163, 1975.
- [15] S. Nussinov. Perturbative recipe for quark-gluon theories and some of its applications. *Phys. Rev.*, D14:246, 1976.
- [16] R. Bonino *et al.*. Evidence for transverse jets in high-mass diffraction. *Phys. Lett.*, B211:239, 1988.
- [17] A. Brandt *et al.*. Evidence for super-hard pomeron structure. *Phys. Lett.*, B297:417, 1992.

BIBLIOGRAPHY

- [18] M. Derrick *et al.* Measurement of the diffractive structure function in deep inelastic scattering at HERA. *Z. Phys.*, C68:569, 1995.
- [19] M. Derrick *et al.* Diffractive hard photoproduction at HERA and evidence for the gluon content of the pomeron. *Phys. Lett.*, B356:129, 1995.
- [20] F. Abe *et al.* Observation of diffractive W-boson production at the Fermilab Tevatron. *Phys. Rev. Lett.*, 78:2698, 1997.
- [21] F. Abe *et al.* Measurement of diffractive dijet production at the Fermilab Tevatron. *Phys. Rev. Lett.*, 79:2636, 1997.
- [22] T. Affolder *et al.* Observation of diffractive b-quark production at the Fermilab Tevatron. *Phys. Rev. Lett.*, 84:232, 2000.
- [23] S. Abachi *et al.* Hard single diffractive jet production at D0. *Fermilab-Conf-96/247-E*, 1996.
- [24] L. Alvero, J. C. Collins, J. Terron, and J.J. Whitmore. Diffractive production of jets and weak bosons and tests of hard-scattering factorization. *Phys. Rev.*, D59:074022, 1999.
- [25] R. J. M. Covolan and M. S. Soares. Analysis of the diffractive production of W 's and dijets at the DESY HERA and Fermilab Tevatron colliders. *Phys. Rev.*, D60:054005, 1999.
- [26] R. J. M. Covolan and M. S. Soares. Erratum: Analysis of the diffractive production of W 's and dijets at the DESY HERA and Fermilab Tevatron colliders [Phys. Rev. D 60, 054005 (1999)]. *Phys. Rev.*, D61:019901, 2000.
- [27] A. Donnachie and P. V. Landshoff. Diffractive deep inelastic lepton scattering. *Phys. Lett.*, B191:309, 1987.
- [28] A. Donnachie and P.V. Landshoff. Hard diffraction: production of high p_T jets, W or Z , and Drell-Yan pairs. *Nucl. Phys.*, B303:634, 1988.
- [29] P. Bruni and G. Ingelman. Diffractive hard scattering at ep and $p\bar{p}$ colliders. *DESY-93-187*, in *Proceedings of the International Europhysics Conference on High Energy Physics, Marseille, France*, 1993.
- [30] K. Goulianos. Renormalization of hadronic diffraction and the structure of the pomeron. *Phys. Lett.*, B358:379, 1995.
- [31] K. Goulianos. Factorization and scaling in hadronic diffraction. *hep-ph/9805496*, 1998. Published in *Phys. Rev.*, D59:114017, 1999.
- [32] K. Goulianos. Factorization and scaling in hard Diffraction. *hep-ph/9708217*, 1997.
- [33] J. D. Bjorken. Rapidity gaps and jets as a new-physics signature in very-high-energy hadron-hadron collisions. *Phys. Rev.* D47:101, 1993.
- [34] E. Gotsman, E. Levin, and U. Maor. Energy dependence of the survival probability of large rapidity gaps. *Phys. Lett.* B438:229, 1998.

BIBLIOGRAPHY

- [35] E. Gotsman, E. Levin, and U. Maor. Survival probability of large rapidity gaps in a three channel model. *Phys. Rev.* D60:094011, 1999.
- [36] B. E. Cox, K. Goulianos, L. Lönnblad, and J. J. Whitmore. Outstanding problems in the phenomenology of hard diffractive scattering.
- [37] H. Fritzsche and K.-H. Streng. Diffractive production of heavy flavors and the internal structure of the pomeron. *Phys. Lett.* B164:391, 1985.
- [38] K. Kodama *et al.* Search for diffractive charm production in 800 GeV/c proton-silicon interactions. *Phys. Lett.* B316:188, 1993.
- [39] A. Kernan and G. VanDalen. Charm and beauty production in strong interactions. *Phys. Rep.*, 106:297, 1984.
- [40] W. Lockman *et al.* Evidence for Λ_c^+ in inclusive $pp \rightarrow (\Lambda^0 \pi^+ \pi^+ \pi^-) + X$ and $pp \rightarrow (K^- \pi^+ p) + X$ at $\sqrt{s} = 53$ and 62 GeV. *Phys. Lett.*, B85:443, 1979.
- [41] K. L. Giboni *et al.* Diffractive production of the charmed baryon Λ_c^+ at the CERN ISR. *Phys. Lett.*, B85:437, 1979.
- [42] J. Irion *et al.* Production of charmed particles at the CERN intersecting storage rings in events triggered by an electron. *Phys. Lett.*, B99:495, 1981.
- [43] M. Basile *et al.* Measurement of associated charm production in pp interactions at $\sqrt{s} = 62$ GeV. *Nuovo Cimento*, A63:230, 1981.
- [44] D. Drijard *et al.* Charmed baryon production at the CERN intersecting storage rings. *Phys. Lett.*, B85:452, 1979.
- [45] S. J. Brodsky, P. Hoyer, C. Peterson, and N. Sakai. The intrinsic charm of the proton. *Phys. Lett.*, B93:451, 1980.
- [46] S. J. Brodsky, C. Peterson, and N. Sakai. Intrinsic heavy quark states. *Phys. Rev.*, D23:2745, 1981.
- [47] J. A. Appel. Hadroproduction of charm particles. *Annu. Rev. Nucl. Part. Sci.*, 42:367, 1992.
- [48] P. Nason, S. Dawson and R. K. Ellis. The total cross section for the production of heavy quarks in hadronic collisions. *Nucl. Phys.*, B303:607, 1988.
- [49] P. Nason, S. Dawson and R. K. Ellis. The one particle inclusive differential cross section for heavy quark production in hadronic collisions. *Nucl. Phys.*, B327:49, 1989.
- [50] W. Beenaker, H. Kuijf, and W. L. van Neerven. QCD corrections to heavy-quark production in $p\bar{p}$ collisions. *Phys. Rev.*, D40:54, 1989.
- [51] Shuyu Lee. *Lambda Polarization in Exclusive and Diffractive Inclusive Final States Produced in Proton-Proton diffraction Dissociation at 800 GeV/c*. Ph.D. thesis, University of Massachusetts, Amherst, MA, 1994.

BIBLIOGRAPHY

- [52] Kyriacos Markianos. *Spin Parity Measurement of Centrally Produced ($\pi^+ \pi^-$) in Proton-Proton Collisions at 800 GeV/c*. Ph.D. thesis, University of Massachusetts, Amherst, 1997.
- [53] Benjamin Stern. *A Search for Charmed Particles in 15-28 GeV Neutron-Proton Interactions*. Ph.D. thesis, Columbia University, 1988.
- [54] D. C. Christian *et al.* High rate drift chambers. *Nucl. Inst. & Meth. in Phys. Res.*, A345:62, 1994.
- [55] A. Ito *et al.* Ziptrack Manual. *Fermilab-TM-1200*, 1983.
- [56] E. P. Hartouni *et al.* Precise measurement of the Λ^0 and $\bar{\Lambda}^0$ masses and a test of *CPT* invariance. *Phys. Rev. Lett.* 72:1322, 1994.
- [57] M. H. L. S. Wang *et al.* Precise measurement of the Σ^0 mass. *Phys. Rev.*, D56:2544, 1997.
- [58] Particle Data Group: C. Caso *et al.* Review of Particle Physics. *Eur. Phys. J.* C3:1, 1998.
- [59] E. P. Hartouni *et al.* High speed simultaneous measurement of pulse area and time-of-flight for photomultiplier signals. *Nucl. Inst. & Meth. in Phys. Res.*, A317:161, 1992.
- [60] W. Sippach, G. Benenson, and B. Knapp. Real time processing of detector data. *IEEE Trans. on Nucl. Sci.* NS27:578, 1980.
- [61] W. Sippach. Data driven architecture. Contribution to the *Workshop on Triggering, Data Acquisition and Computing for High energy/High Luminosity Hadron-Hadron Colliders*, Fermilab, Nov. 11-14, 1985.
- [62] L. Borten *et al.* A data driven parallel pipelined hardware reconstruction processor. *Proceedings of the Symposium on Recent Developments in Computing, Processor and Software Research for High Energy Physics, Guanajuato, Mexico, May, 1984*.
- [63] E. P. Hartouni *et al.* A new technique for on-line and off-line high speed computation. *IEEE Trans. on Nucl. Sci.* NS36:1480, 1989.
- [64] B. C. Knapp. High speed data-driven processing. *Nucl. Inst. & Meth. in Phys. Res.*, A289:561, 1990.
- [65] CN/ASD Group. *HBOOK Reference Manual*, Version 4.22. CERN, 1995. CERN Program Library Y250.
- [66] H.-U. Bengtsson and T. Sjöstrand. High-energy-physics event generation with PYTHIA 5.7 and JETSET 7.4. *Computer Physics Communications*, 82:74, 1994.
- [67] B. Andersson *et al.* Parton fragmentation and string dynamics. *Phys. Rep.*, 97:31, 1983.
- [68] Y. S. Tsai. Pair production and bremsstrahlung of charged leptons. *Rev. of Mod. Phys.*, 46:815, 1974.

BIBLIOGRAPHY

- [69] J. H. Hubbel, H. A. Gimm, and I. Øverbø. Pair, triplet, and total atomic cross sections (and mass attenuation coefficients) for 1 MeV-100 GeV Photons in Elements Z=1 to 100. *J. Phys. Chem. Ref. Data*, 9:1023, 1980.
- [70] H. A. Gimm. Cross sections for the photoproduction of electron-positron pairs in the field of atomic electrons. *Phys. Rev.*, A25:823, 1982.
- [71] S. Frixione, M. Mangano, P. Nason, and G. Ridolfi. Heavy-quark production. *hep-ph/9702287 v2*, 1997.
- [72] K. Kodama *et al.* Charm meson production in 800 GeV/c proton-emulsion interactions. *Phys. Lett.* B263:573, 1991.
- [73] R. Ammar *et al.* D-Meson production in 800 GeV/c pp Interactions. *Phys. Rev. Lett.*, 61:2185, 1988.